Summer 2024

Computational Analysis of a NACA 0012 Straight Wing at Various Reynolds Numbers Approaching Stall

John E. Crowe III

COMPUTATIONAL ANALYSIS OF A NACA 0012 STRAIGHT WING AT VARIOUS REYNOLDS NUMBERS APPROACHING STALL

by

JOHN CROWE

Under the Direction of Mosfequr Rahman

ABSTRACT

As the capabilities and power of computational resources improve with each passing year, the implementation of simulation in the field of aerospace engineering also increases due to its increased efficiency, as it allows for reducing both time and resources. In this study, a computational method is created and tested for determining and visualizing the effect of increasing flow velocity on a NACA 0012 3D wing as it approaches and reaches stall. For this study, the flow over a NACA 0012 3D wing is simulated using a Reynolds-averaged Navier Stokes simulation at angles of attack of 6, 8, 10, 12, and 15 degrees. These simulations are run with 4 separate flow speeds with Reynolds numbers of 6.0E+5, 8.0E+5, 1.0E+6, and 1.2E+6. From these simulations, the flow properties and aerodynamic forces are gathered and compared with one another. In this study, it was determined that the wing stalled after exceeding 12° for each air speed simulated, with the wing in Re = 6.0E+5 flow approaching stall faster. For each increment in Re at the same aoa, the lift and drag rose by approximately 1%. While in stall, large circulation occurring from flow separation occurs in the flow over the upper wing surface, resulting in large drops in lift and causes the drag to sharply increase. The lift-to-drag ratio for each airspeed dropped by approximately 63% when going from 12° to 15° for each airspeed.

INDEX WORDS: Aerodynamics, Fluent, Computational Fluid Dynamics, Reynolds Averaged Navier-Stokes, Stall

COMPUTATIONAL ANALYSIS OF A NACA 0012 STRAIGHT WING AT VARIOUS REYNOLDS NUMBERS APPROACHING STALL

by

JOHN CROWE

B.S.A.E, North Carolina State University, 2021

A Thesis Submitted to the Graduate Faculty of Georgia Southern University

in Partial Fulfillment of the Requirements for the Degree

MASTER OF SCIENCE

ALLEN E. PAULSON COLLEGE OF ENGINEERING AND COMPUTING

STATESBORO, GEORGIA

COMPUTATIONAL ANALYSIS OF A NACA 0012 STRAIGHT WING AT VARIOUS REYNOLDS NUMBERS APPROACHING STALL

by

JOHN CROWE

Major Professor:	Mosfequr Rahman
Committee:	Marcel Ilie
	Valentin Soloiu

Electronic Version Approved:
July 2024

DEDICATION

I wish to dedicate this thesis to my parents, John, and Marianne Crowe, as well as my brother Daniel Crowe for their continued love and support throughout the years.

ACKNOWLEDGMENTS

The research in this thesis was supported by the Department of Mechanical Engineering at Georgia Southern University as well as the DoD-NSF assure REU site award: 1950207. I would like to express my sincere gratitude to my research advisor, Dr. Mosfequr Rahman, for the guidance and assistance during my graduate career. I would also like to thank Dr. Marcel Ilie and Dr. Valentin Soliu for their continued support and assistance in my research and graduate career.

I would also like to thank my fellow graduate students, Eric Pernell, Cameron Perry, Charles Fricks, Austin Robbins, Whitney Curwin, and David Obando for their support both in class and in the laboratory.

TABLE OF CONTENTS

Acknowledgements 3

Table of Contents 4

List of Tables 6

List of Figures 7

1. Introduction 13

    1.1 Lift and Drag 13

    1.2 Stall 15

    1.3 Goal and Objectives 16

    1.4 Hypothesis 17

2. Literaturre Review 18

    2.1 Literature Relating to Lift and Drag 18

    2.2 Literature relating to Boundary Layer and Stall 20

    2.3 Computational Models 23

3. Methods 26

    3.1 Conservation Equations 26

    3.2 Steady-State Computational Fluid Dynamics 27

    3.3 Flow Properties and Airfoil 31

    3.4 Non-Dimensional Parameters and Aerodynamic Similarity Criterion 32

    3.5 Model Geometry Characteristics 35

    3.6 Mesh Generation 36

3.7 Boundary Conditions 39

3.8 Computational Models 40

4. Results and Conclusion 45

4.1: Lift and Drag Coefficients 45

4.2: Pressure and Velocity 48

4.3: Turbulence Kinetic energy and Wall Shear 58

5. Conclusion 62

5.1 Future Recommendations 62

References 64

Appendix 70

Appendix A Pressure and Velocity Contours 70

Appendix B Wall Shear Vector and Turbulence Kinetic Energy Plots 84

Appendix C Skin Friction Coefficient Plots 91

Appendix D Streamline Plots 99

LIST OF TABLES

Table 3.3.1: Simulation Fluid Properties and Wing Geometry for NACA 0012 Wing..... 31

Table 3.6.1: Element Size vs Maximum Velocity..... 37

Table 3.6.2: Fluid Domain Mesh Statistics..... 38

Table 4.1.1: Lift and Drag Coefficients vs Angle of attack for Re = 6.0E+5 45

Table 4.1.2: Lift and Drag Coefficients vs Angle of attack for Re = 8.0E+5 46

Table 4.1.3: Lift and Drag Coefficients vs Angle of attack for Re = 1.0E+6 46

Table 4.1.4: Lift and Drag Coefficients vs Angle of attack for Re = 1.2E+6 46

LIST OF FIGURES

Figure 1.1: Lift and Drag components of Cambered Airfoil 15

Figure 1.2.1: Velocity Streamline of an Airfoil Undergoing Stall 16

Figure 2.1.1: Lift Coefficient, C_l (a) and Drag Coefficient, C_d (b) vs Angle of Attack, α for NACA 0012 at Various Reynolds 20

Figure 3.3.1: NACA 0012 Airfoil Plot 32

Figure 3.5.1: Fluid Domain Geometry; 2D Side View (Left), and 3D Isometric View (Right) 35

Figure 3.6.1: Mesh Resolution at Wing Surface 37

Figure 3.6.2: Mesh Resolution Near Wing Surface (α = 10° Shown) 39

Figure 3.6.3: Total Volume Mesh Resolution (α = 10° Shown) 39

Figure 3.7.1: Boundary Conditions for Fluid Domain; Side View (Left) and Front View (Right) 40

Figure 3.9.1: Residuals Plot for Re = 6.0E+5, α = 6° (Top); Re = 1.2E+6, α = 15° (Bottom) 44

Figure 4.1.1: Lift Coefficient (C_L) vs Angle of Attack (α) 47

Figure 4.1.1: Drag Coefficient (C_D) vs Angle of Attack (α) 47

Figure 4.1.1: Lift-to-Drag Ratio vs Angle of Attack (α) 48

Figure 4.2.1: Gauge Pressure Contour at Alpha = 6°; Re = 6.0E+5 (Top) & Re= 1.2E+6 (Bottom) 49

Figure 4.2.2: Velocity Contour at Alpha = 6°; Re = 6.0E+5 (Top) & Re= 1.2E+6 (Bottom) 50

Figure 4.2.3: Gauge Pressure Contour at Alpha = 9°; Re = 6.0E+5 (Top) & Re= 1.2E+6 (Bottom) 51

Figure 4.2.4: Velocity Contour at Alpha = 9°; Re = 6.0E+5 (Top) & Re= 1.2E+6 (Bottom) 52

Figure 4.2.5: Gauge Pressure Contour at Alpha = 12°; Re = 6.0E+5 (Top) & Re= 1.2E+6 (Bottom) 53

Figure 4.2.6: Velocity Contour at alpha = 12°; Re = 6.0E+5 (Top) & Re= 1.2E+6 (Bottom) 54

Figure 4.2.7: Gauge Pressure Contour at Alpha = 15°; Re = 6.0E+5 (Top) & Re= 1.2E+6 (Bottom) 55

Figure 4.2.8: Velocity Contour at Alpha = 15°; Re = 6.0E+5 (Top) & Re= 1.2E+6 (Bottom) 56

Figure 4.2.9: Pressure Coefficient (C_P) vs. Chord Length (m) for Re = 1.0E+6, Alpha = 15° 57

Figure 4.2.10: Flow Streamline plot for Alpha = 15°, Re = 1.0E+6 57

Figure 4.3.1: TKE Contour Plot for Alpha = 15°, Re = 6.0E+5 58

Figure 4.3.2: TKE Contour Plot for Alpha = 15°, Re = 8.0E+5 59

Figure 4.3.3: TKE Contour Plot for Alpha = 15°, Re = 1.0E+6 59

Figure 4.3.4: TKE Contour Plot for Alpha = 15°, Re = 1.2E+6 59

Figure 4.3.3: Wall Shear Vector Plots for Alpha = 6°; Re = 6.0E+5 (Top) & Re= 1.2E+6 (Bottom) 60

Figure 4.3.3: Wall Shear Vector Plots for Alpha = 15°; Re = 6.0E+5 (Top) & Re= 1.2E+6 (Bottom) 61

Figure A.1: Pressure Contour at Re = 6.0E5; α = 6° 70

Figure A.2: Pressure Contour at Re = 6.0E5; α = 9° 70

Figure A.3: Pressure Contour at Re = 6.0E5; α = 12° 71

Figure A.4: Pressure Contour at Re = 6.0E5; α = 15° 71

Figure A.5: Pressure Contour at Re = 8.0E5; α = 6° 72

Figure A.6: Pressure Contour at Re = 8.0E5; α = 9° 72

Figure A.7: Pressure Contour at Re = 8.0E5; α = 12° 72

Figure A.7: Pressure Contour at Re = 8.0E5; α = 15° 73

Figure A.8: Pressure Contour at Re = 1.0E6; α = 6° 73

Figure A.9: Pressure Contour at Re = 1.0E6; α = 9° 74

Figure A.10: Pressure Contour at Re = 1.0E6; α = 12° 74

Figure A.11: Pressure Contour at Re = 1.0E6; α = 15° 74

Figure A.12: Pressure Contour at Re = 1.2E6; α = 6° 75

Figure A.13: Pressure Contour at Re = 1.2E6; α = 9° 75

Figure A.14: Pressure Contour at Re = 1.2E6; α = 12° 75

Figure A.15: Pressure Contour at Re = 1.2E6; α = 15° 76

Figure A.16: Velocity Contour at Re = 6.0E5; α = 6° 77

Figure A.17: Velocity Contour at Re = 6.0E5; α = 9° 77

Figure A.18: Velocity Contour at Re = 6.0E5; α = 12° 78

Figure A.19: Velocity Contour at Re = 6.0E5; α = 15° 78

Figure A.20: Velocity Contour at Re = 8.0E5; α = 6° 79

Figure A.21: Velocity Contour at Re = 8.0E5; α = 9° 79

Figure A.22: Velocity Contour at Re = 8.0E5; α = 12° 79

Figure A.21: Velocity Contour at Re = 8.0E5; α = 15° 80

Figure A.22: Velocity Contour at Re = 1.0E6; α = 6° 80

Figure A.23: Velocity Contour at Re = 1.0E6; α = 9° 81

Figure A.24: Velocity Contour at Re = 1.0E6; α = 12° 81

Figure A.25: Velocity Contour at Re = 1.0E6; α = 15° 81

Figure A.26: Velocity Contour at Re = 1.2E6; α = 6° 82

Figure A.27: Velocity Contour at Re = 1.2E6; α = 9° 82

Figure A.28: Velocity Contour at Re = 1.2E6; α = 12° 83

Figure A.29: Velocity Contour at Re = 1.2E6; α = 15° 83

Figure B.1: Wall Shear Vector Plot for Re = 6.0E5; α = 6° 84

Figure B.2: Wall Shear Vector Plot for Re = 6.0E5; α = 9° 84

Figure B.3: Wall Shear Vector Plot for Re = 6.0E5; α = 12° 85

Figure B.4: Wall Shear Vector Plot for Re = 6.0E5; α = 15° 85

Figure B.5: Wall Shear Vector Plot for Re = 8.0E5; α = 6° 86

Figure B.6: Wall Shear Vector Plot for Re = 8.0E5; α = 9° 86

Figure B.7: Wall Shear Vector Plot for Re = 8.0E5; α = 12° 87

Figure B.8: Wall Shear Vector Plot for Re = 8.0E5; α = 15° 87

Figure B.9: Wall Shear Vector Plot for Re = 1.0E6; α = 6° 87

Figure B.10: Wall Shear Vector Plot for Re = 1.0E6; α = 9° 88

Figure B.11: Wall Shear Vector Plot for Re = 1.0E6; α = 12° 88

Figure B.12: Wall Shear Vector Plot for Re = 1.0E6; α = 15° 88

Figure B.13: Wall Shear Vector Plot for Re = 1.2E6; α = 6° 89

Figure B.14: Wall Shear Vector Plot for Re = 1.2E6; α = 9° 89

Figure B.15: Wall Shear Vector Plot for Re = 1.2E6; α = 12° 90

Figure B.16: Wall Shear Vector Plot for Re = 1.2E6; α = 15° 90

Figure C.1: Skin Friction Coefficient Plot for Re = 6.0E5; α = 6° 91

Figure C.2: Skin Friction Coefficient Plot for Re = 6.0E5; α = 9° 91

Figure C.3: Skin Friction Coefficient Plot for Re = 6.0E5; α = 12° 92

Figure C.4: Skin Friction Coefficient Plot for Re = 6.0E5; α = 15° 92

Figure C.5: Skin Friction Coefficient Plot for Re = 8.0E5; α = 6° 93

Figure C.6: Skin Friction Coefficient Plot for Re = 8.0E5; α = 9° 93

Figure C.7: Skin Friction Coefficient Plot for Re = 8.0E5; α = 12° 94

Figure C.8: Skin Friction Coefficient Plot for Re = 8.0E5; α = 15° 94

Figure C.9: Skin Friction Coefficient Plot for Re = 1.0E6; α = 6° 95

Figure C.10: Skin Friction Coefficient Plot for Re = 1.0E6; α = 9° 95

Figure C.11: Skin Friction Coefficient Plot for Re = 1.0E6; α = 12° 96

Figure C.12: Skin Friction Coefficient Plot for Re = 1.0E6; α = 15° 96

Figure C.13: Skin Friction Coefficient Plot for Re = 1.2E6; α = 6° 97

Figure C.14: Skin Friction Coefficient Plot for Re = 1.2E6; α = 9° 97

Figure C.15: Skin Friction Coefficient Plot for Re = 1.2E6; α = 12° 98

Figure C.16: Skin Friction Coefficient Plot for Re = 1.2E6; α = 15° 98

Figure D.1: Velocity Streamline for Re = 6.0E5; α = 6° 99

Figure D.2: Velocity Streamline for Re = 6.0E5; α = 9° 99

Figure D.3: Velocity Streamline for Re = 6.0E5; α = 12° 100

Figure D.4: Velocity Streamline for Re = 6.0E5; α = 15° 100

Figure D.5: Velocity Streamline for Re = 8.0E5; α = 6° 101

Figure D.6: Velocity Streamline for Re = 8.0E5; α = 9° 101

Figure D.7: Velocity Streamline for Re = 8.0E5; α = 12° 101

Figure D.8: Velocity Streamline for Re = 8.0E5; α = 15° 102

Figure D.9: Velocity Streamline for Re = 1.0E6; α = 6° 102

Figure D.10: Velocity Streamline for Re = 1.0E6; α = 9°..... 102

Figure D.11: Velocity Streamline for Re = 1.0E6; α = 12°..... 103

Figure D.12: Velocity Streamline for Re = 1.0E6; α = 15°..... 103

Figure D.13: Velocity Streamline for Re = 1.2E6; α = 6°..... 104

Figure D.14: Velocity Streamline for Re = 1.2E6; α = 9°..... 104

Figure D.15: Velocity Streamline for Re = 1.2E6; α = 12°..... 105

Figure D.16: Velocity Streamline for Re = 1.2E6; α = 15°..... 105

CHAPTER 1

INTRODUCTION

The wings of an aircraft are undoubtedly the most integral part of an aircraft's ability to fly. Ever since the first flight of an aircraft by the Wright brothers in 1903, wings have gone through immense changes to become what they are today. A tremendous amount of research and development goes into increasing the aerodynamic efficiency of wings every day. The focus of this research is on increasing the accuracy of aerodynamic simulations, allowing for further increases in aerodynamic and structural efficiency.

1.1 Lift and Drag

Aerodynamic efficiency boils down to increasing the lift force and decreasing the drag force of an aircraft. Lift is the upwards force perpendicular to the freestream air flow that is responsible for allowing the wing to fly. Lift is caused by a pressure difference between the top and bottom surfaces of the wing, with the pressure across the upper surface being lower than that of the bottom surface. This can be achieved in various ways, one of which is by increasing the angle of attack of a surface undergoing fluid flow. Angle of attack refers to the angle between the wing and the freestream fluid flow and is represented by the Greek letter α. Increasing angle of attack causes the pressure to increase on the lower side, since the surface area of the bottom surface perpendicular to the flow increases. This pressure difference can also be achieved without having to increase the angle of attack using a cambered airfoil, where an airfoil refers to the two-dimensional cross section of a wing. The shape of this airfoil causes the flow over the upper side

of the wing to take a longer path than the bottom side, this difference in flow speed causes the pressure on the upper surface of the wing to be lower than the pressure across the bottom surface, creating lift.

Drag is the force that is perpendicular to the lift force, opposing the forward movement of a wing. This drag force can be separated into two main types: parasite drag and induced drag. Induced drag is the drag force that is generated from the generated lift on a 3D wing. The pressure difference between the top and bottom of the wing causes vortices to form at the ends of the wing where top and bottom flows meet and the higher-pressure flow on the bottom of the wing flows upward towards the lower pressure flow on the upper surface. The vortices that propagate from this phenomenon cause a backwards force on the wing, resulting in increased drag. Induced drag increases with increased lift since the pressure difference between the top and bottom wing surfaces is increasing, thus increasing the strength of the resulting vortices. (CHENG et al. 2022). Parasite drag is the drag force that propagates from the friction of the fluid on the surface of the wing and the force from the lateral pressure on the wing surface. The drag that forms from friction forces contributes to about half of the overall drag force. (ZHANG et al. 2020; Anderson 2012)

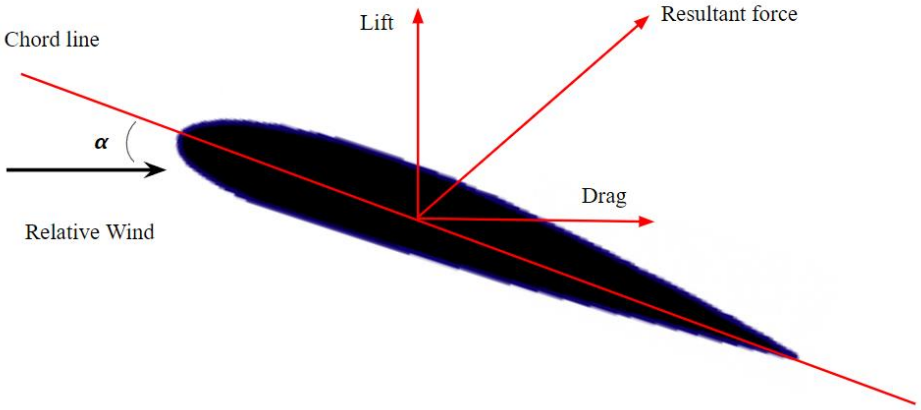

Figure 1.1: Lift and Drag components of Cambered Airfoil

1.2 Stall

Even though lift can be increased by increasing the angle of attack of a wing, there is a certain point where the fluid flow separates from the wing's surface, this separation causes a drastic decline in lift and has the potential to cause an aircraft to crash. This condition is known as stall. It is impeccable to an aircraft's safety to avoid stall at all costs; however, stall can be recovered from if the pilot is experienced enough. (Akbari and Price 2003) There is no way for the possibility of stall to be eliminated for an airfoil, but the angle of attack at which the stall will occur can be delayed through devices such as vortex generators. When a wing or airfoil enters stall, the boundary layer of the fluid flow begins to separate from the upper surface of the wing. If the angle of attack continues to rise, the point at which the flow separates gets closer to the leading edge. When the separation reaches the leading edge, the wing is under full stall, where there is no flow over the upper surface. If an aircraft in flight enters full stall, it is impossible to recover from, regardless of the pilot. When this separation occurs, the flow begins to recirculate into the area of

separation. This recirculation causes the flow to become unstable and drastically increases drag, while drastically reducing lift. (Mccroskey 1981; Tao, Wang, and Sun 2021; Chen et al. 2022)

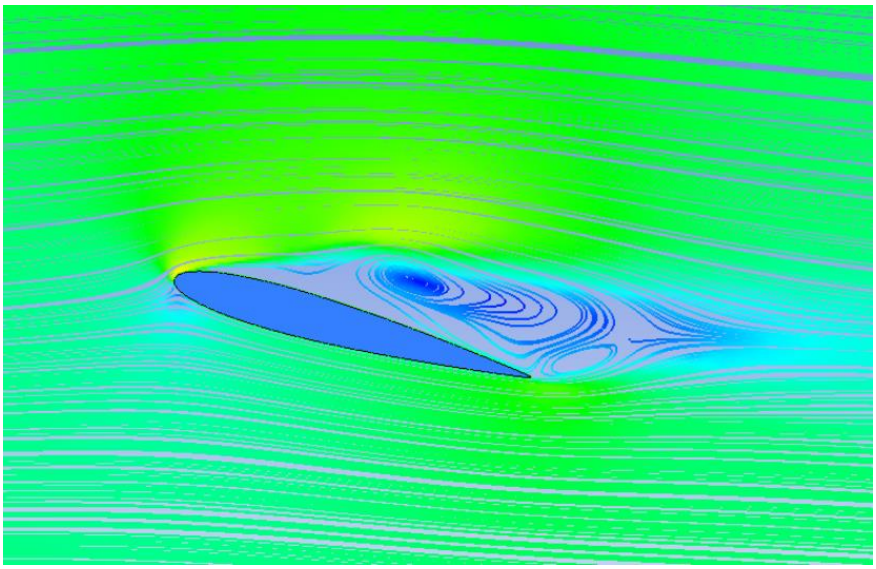

Figure 1.2.1: Velocity Streamline of an Airfoil Undergoing Stall

1.3 Goal and Objectives

The goal of this research is to create and validate a fully coupled fluid dynamics/structural dynamics simulation of a wing at low Reynolds to allow for the analysis of the induced vibrations on a wing in fluid flow. This goal will be achieved by creating a fully coupled aerodynamic and structural simulation that will be compared to both an aerodynamic only simulation and a wind tunnel experimental setup to properly show the effect of adding aeroelastic forces to the simulation. This simulation will show the benefits of using this type of simulation as opposed to an uncoupled, CFD only approach.

The goal of this research is to compare the aerodynamic effect of increasing angle of attack and flow velocity on a 3D NACA 0012 wing near and at stall conditions through computational

means. In order to achieve this, a steady state computational fluid dynamics simulation using a 3D NACA 0012 wing is created for various flow speeds and angle of attack. The various results gained from these simulations are then gathered and compared with each other to exemplify how each variable affects the flow properties and aerodynamic forces.

1.4 Hypothesis

Increasing the flow velocity and angle of attack of a wing increases both the lift and drag generated by the wing up until flow separation occurs, where the lift sharply decreases and the drag sharply increases, therefore a 3D NACA 0012 going from an angle of attack of 12° to 15° will exhibit a drop in the generated lift-to-drag ratio of at least 60%

CHAPTER 2

LITERATURE REVIEW

Research into improving the efficiency of aircraft has been constantly being performed since the dawn of aviation. The primary focuses of this research are improvements to aerodynamic efficiency and structural efficiency, which often become intertwined. Increases of the efficiency of an aircraft can benefit a multitude of factors such as maneuverability, fuel efficiency, and safety. For any aircraft, both commercial and private, safety is the primary concern.

Many different factors contribute to the safety of an aircraft, but one of the most important indicators of the safety of an aircraft is how early it stalls and how easy it is for the aircraft to exit stall. Stall refers to the aerodynamic condition that occurs when the flow over an airfoil or wing becomes separated from the upper surface, drastically reducing lift and increasing drag. (Tao, Wang, and Sun 2021) When an aircraft enters stall, it essentially starts to fall out of the sky. If the stall is not recovered from, it will inevitably result in the aircraft crashing.

2.1 Literature Relating to Lift and Drag

The lift and drag generated by an airfoil are the two key components of the aerodynamic efficiency of a wing. Lift is the upwards force on the airfoil produced by pressure differences between the top and bottom surfaces of an airfoil. (Auteri et al. 2022). Drag is the force that is perpendicular to the lift force, opposing the forward movement of a wing. This drag force can be separated into two main types: parasite drag and induced drag. Induced drag is the drag force that is generated from the generated lift on a 3D wing. The pressure difference between the top and bottom of the wing causes vortices to form at the ends of the wing where top and bottom flows meet and the higher-pressure flow on the bottom of the wing flows upward towards the lower

pressure flow on the upper surface. The vortices that propagate from this phenomenon cause a backwards force on the wing, resulting in increased drag. (CHENG et al. 2022; Kroo 2003) Parasite drag is the drag force that is created by skin friction and the geometry of an object due to increased pressure on an area, such as a bluff body. (ZHANG et al. 2020)

For an aircraft wing, parasite drag from friction is the largest component of drag on the wing, contributing to about half of the overall drag force. Friction drag, as the name suggests, is the drag caused by the friction of a fluid against the surface of an object that is passing through the fluid. The fluid's interaction with the surface causes the velocity directly above the surface to become zero, and slowly speeds up as the distance away from the surface increases until the speed is equivalent to the outside flow. The area where this occurs is known as the boundary layer. The size of the boundary layer is determined primarily by the amount of friction between the fluid and the surface that the fluid is passing over. An increase in the friction coefficient of the surface will increase the area where the fluid is slower than the outside flow. (ZHANG et al. 2020). For aircraft wings and many other aerodynamic surfaces, it is impeccable to ensure that the fluid flow remains attached to the surface. Too much friction or pressure differences, especially with air, can easily cause a flow to become more turbulent, increasing the friction coefficient and increasing the size of the boundary layer until the flow becomes completely separated from the surface, resulting in stall. (Anderson 2012)

Since the need for efficiency is so large in aviation, nearly every aircraft uses a different airfoil based on flight conditions. Due to this variability of airfoils, specific airfoils are typically chosen for research based on flow properties to create replicability. The most common airfoil used in research for low Reynolds flow is the NACA 0012 airfoil (Srinivasa Rao, Mahapatra, and

Chaitanya Mangavelli 2018; Han et al. 2021; Mahato et al. 2023; Chang et al. 2022; Chen et al. 2022). This airfoil is so common because of its simplicity, being a symmetrical airfoil with relatively low thickness, meaning it stalls at a higher angle of attack than a traditional cambered airfoil, and produces no lift at an angle of attack of zero degrees. This simplicity makes this airfoil an ideal baseline when performing aerodynamic research on wings and airfoils. A study done on the influence of turbulence intensity on aerodynamic characteristics of a 2D NACA 0012 airfoil at low Reynolds shows how the lift and drag coefficient changes with relation to angle of attack and Reynolds number. (Tsuchiya et al. 2013)

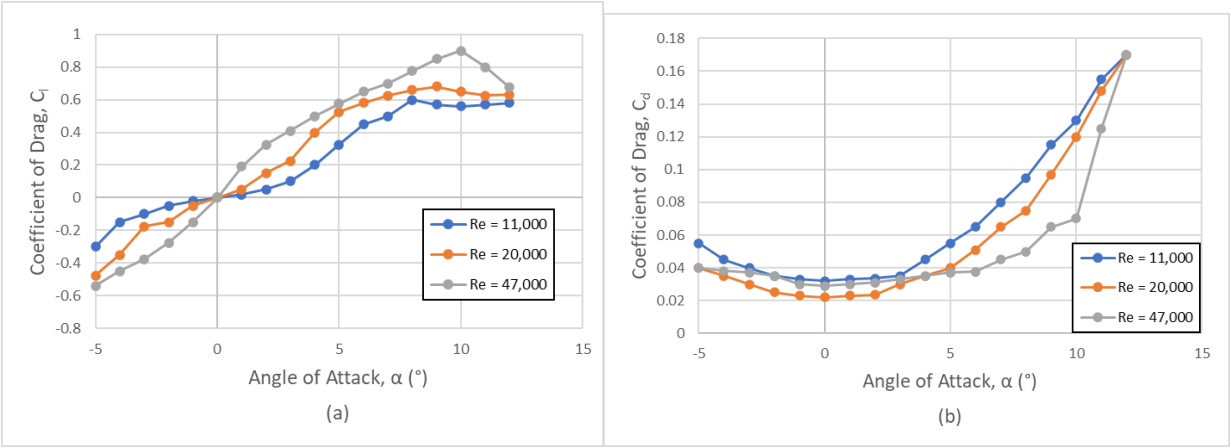

Figure 2.1.1: Lift Coefficient, C_l (a) and Drag Coefficient, C_d (b) vs Angle of Attack, α for NACA 0012 at Various Reynolds (Tsuchiya et al. 2013)

2.2 Literature relating to Boundary Layer and Stall

A key point of interest when examining fluid dynamics is the concept of the boundary layer. The boundary layer refers to the thin layer of fluid in the immediate vicinity of a surface undergoing fluid flow. Studies show that the boundary layer exists due to friction between a fluid and the

surface the fluid is passing over. Due to this friction, the fluid's velocity becomes zero at the surface/wall. This condition is commonly referred to as a no-slip boundary condition. The velocity of the fluid increases above the surface until it reaches the free stream velocity. This thin layer of the fluid whose velocity has not yet reached free stream velocity is what is denoted as the boundary layer. (Rouser 2002; Casey 2004; Anderson 2012).

There are two types of boundary layers, laminar and turbulent. Laminar flow is characterized by fluid particles following smooth, predictable paths in layers. In turbulent flow, the flow paths become unstable and start to "swirl". The fluid velocity in a laminar boundary layer increases steadily until reaching free stream, whereas the fluid velocity in a turbulent boundary layer starts increasing slowly, then increases sharply. For flow across an airfoil, the boundary layer typically begins as a laminar boundary layer at the leading edge of the wing, and transitions to turbulent flow at some point across the airfoil's surface. In the case of minimizing drag, it is important to delay this transition as much as possible, as turbulent flow causes more drag than laminar flow. (Schetz and Bowersox 2011; sciences and 2002 2002)

For a two-dimensional airfoil, increasing the angle of attack can increase the lift, however there is a point at which the pressure difference between the top and bottom surface becomes so great that the flow will separate from the surface on the top side of the airfoil. (Tao, Wang, and Sun 2021). Studies have shown that for a 3D wing with a finite wingspan, this point becomes even smaller due to the presence of induced drag and flow turbulence. Typically, once a wing reaches that point, the lift suddenly increases for a short amount of time before plummeting and the flow separates, this sudden increase in lift can increase the angle attack even more if the stall is not controlled fast enough. This further increase in angle of attack pushes the point of boundary layer separation closer to the leading edge of the wing, causing a larger zone of separation and an

increase in vortex strength on the upper area of the wing. As the strength of these vortices increases, the aeroelastic forces acting on the wing also increase. If the zone of separation reaches the leading edge, the flow becomes completely separated from the top surface of the wing and airfoil enters a state known as deep stall. Once an aircraft enters deep stall, it is near impossible to recover from (Carr, 1988; McCroskey et al., n.d.; Mccroskey, 1981).

When analyzing a fixed airfoil in steady flow, the airfoil will always stall at the same angle of attack if the Reynold's number is unchanged. This point is typically referred to as static stall, as it is a specific point at which flow separation occurs, rather than a range. However, for a maneuvering fixed wing aircraft studies have shown that this is not the case. For a 3D, nonfinite wing, the point at which the wing will enter stall varies within around a degree of the static stall point. Dynamic stall is characterized by a delay in boundary layer separation beyond the static stall angle and there have been numerous studies of this phenomenae (Batther and Lee 2022; Mccroskey 1981; W. J. McCroskey, Carr, and McAlister 2012; W. McCroskey et al., n.d.; Carr 1988). This phenomenon may delay the onset of stall for an aircraft, but once an aircraft undergoes dynamic stall in can be severely more problematic for the aircraft. The delay in stall causes the point of flow separation to be closer to the leading edge, meaning it is much closer to entering deep stall. Dynamic stall also results in greater aerodynamic load than static stall due to the increased area of separation, resulting in large, coupled loads that a CFD only simulation would not be able to detect.(Batther and Lee 2022; Akbari and Price 2003; Carr 1988; Wu, Dai, and Yang 2022)

2.3 Computational Models

The equations governing the properties and behavior of a fluid are known as the Navier-Stokes Equations. (Friedlander 2004; Ferziger and Perić 2002; Anderson 2012; Cavagna, Quaranta, and Mantegazza 2007). CFD solves these equations to simulate the fluid flow. However, these equations require simplification methods to be solved, primarily in relation to the turbulence and pressure-velocity coupling. There are a multitude of different models used in CFD studies to solve the turbulence behavior of a fluid, with each model having different strengths and weaknesses. The simplest of these models is known as the Reynolds Averaged Navier-Stokes (RANS) turbulence model, of which there are a few variations. RANS turbulence models are the most common and widespread approach due to their simplicity and lower computational costs, but the use of RANS turbulence models comes with some limitations due to their modeling assumptions. RANS models use an averaged approach and focus primarily on the larger trend of the fluid's flow. As the flow boundary's complexity and degrees of freedom in the flow increase, RANS models become more inaccurate. Because of this, RANS models are used for simple geometries in low-Reynolds flow. One variation of the RANS turbulence model that helps with this limitation is known as the shear stress transport k-omega RANS model. (F. R. Menter 1993). This model has an increased focus on the inner parts of the boundary layer, making it accurate for low-Re turbulence models where small turbulence near a surface is an important focus. This model does not include any extra damping functions like the large eddy simulation (LES) computational model, which drastically increases computational time. (Rahman 2023; Troldborg, Sørensen, and Zahle 2022; Bellegoni et al. 2023). The name of the k-omega SST model comes from the

implementation of turbulence kinetic energy k, and specific dissipation rate ω, in the governing equations.

The discretized forms of the Navier-Stokes equations used for CFD modeling have linear dependence of velocity and pressure and vice-versa. The inter-equation coupling of these two variables is called velocity-pressure coupling. Like with the turbulence models, there are different methods of coupling the pressure and velocity, with different uses for each one. There are two primary algorithms that are used for the pressure-velocity coupling in CFD. One of these algorithms is known as the semi-implicit method for pressure-linked equations, also called the SIMPLE algorithm. This algorithm works by first using an approximation of the velocity field by solving the momentum equation, then the pressure gradient term is calculated using the approximated velocity field and the pressure distribution from the previous iteration. The pressure equation is then formulated and solved to obtain the new pressure distribution. The velocity field is then corrected, and a new set of face mass fluxes is created. This repeats until the pressure and velocity fields converge. This coupling model is typically used for solvers with numerous iterations and typically at low Reynolds flow. (Patankar and Spalding 1972; Ferziger and Perić 2002; Rahman 2023; 2021; Karki and Patankar 2012)

The other primary velocity-pressure coupling method used in research is the PISO algorithm (Pressure implicit with splitting of operator). This method is an extension of the SIMPLE algorithm for simulations with little to no iterations and with large timesteps. It was originally developed for the computation of unsteady compressible flow but has been adapted recently to work with steady state problems as well as incompressible flows. This algorithm works similar to the SIMPLE algorithm; however, it repeats the correction steps 3 times on its own rather than once per iteration. For its intended purpose, the PISO algorithm provides slightly more stable results

with a lower computational time than the SIMPLE algorithm, however in simulations requiring many iterations, it is much slower than SIMPLE and can provide unstable results. (Pries, Fiolitakis, and Gerlinger 2024; Cavagna, Quaranta, and Mantegazza 2007; Ilie 2019a; Sohail and Ullah 2017)

CHAPTER 3

METHODS

3.1 Conservation Equations

All CFD equations are obtained directly from the ANSYS Fluent Theory Guide (ANSYS Inc. 2011). As the simulation of coupled aeroelastic forces requires the implementation of fluid-structure interaction, the turbulent boundary layer should be accurately modeled. Due to this importance, the boundary layer around the wing should be the primary point of interest when performing such a simulation to accurately solve the pressure and velocity at the wing wall. Of the various methods of CFD methods used, there are two prominent standouts when it comes to accurately modeling turbulence, RANS and LES. RANS simulations require significantly less computational resources than that of LES simulations, however RANS simulations provide less accurate results further away from the boundary layer. The type of turbulence model used for a simulation varies on the simulation's application and model characteristics, as well as the available computational resources. Due to its significantly lower computational resources needed, RANS simulations are typically preferred if this method can provide accurate results for a given model. For more complex geometry and flow properties however, simulations using the LES turbulence model may be needed to provide accurate results (Troldborg, Sørensen, and Zahle 2022; Ilie 2019b). For both LES and RANS, the governing equations for mass, momentum and energy are used (ANSYS Inc. 2011). The equation for conservation of mass can be written as:

$$\frac{\partial \rho}{\partial t} + \nabla * (\rho \vec{v}) = S_m \tag{3.1.1}$$

where the source term S_m is added to the continuity equation. This conservation of mass equation is applicable to both incompressible and compressible flows. The equations for conservation of momentum as well as conservation of energy respectively are defined as follows:

$$\frac{\partial}{\partial t}(\rho\vec{v}) + \nabla \cdot (\rho\vec{v}\vec{v}) = -\nabla p + \rho\vec{g} + \vec{F} \tag{3.1.2}$$

$$\frac{\partial}{\partial t}(\rho E) + \nabla \cdot \left(\vec{v}(\rho E + p)\right) = -\nabla \cdot \left(\sum_j h_j J_j\right) + S_h \tag{3.1.3}$$

where p is the local static pressure and $\rho\ \vec{g}$ and $\vec{F}$ are body forces, and $\bar{\bar{\tau}}$ is the shear stress tensor (ANSYS Inc. 2011).

3.2 Steady-State Computational Fluid Dynamics

There are two primary types of simulations used for CFD application: steady-state and transient. Steady-state simulations represent a time averaged simulation, whereas transient simulations simulate flow properties over user specified time periods. Steady-state simulations are preferred when applicable due to their higher accuracy with respect to computational time. Time averaged, steady-state simulations can also be used to initialize longer simulations such as LES to save computational time.

For the purposes of this study, steady-state simulation is used due to the lower computational time compared to a transient simulation. Since this type of simulation uses a time-averaged solution the results gathered are more reliable and consistent compared to a transient solution. A transient simulation is needed to represent changes in a fluid's flow over time, and and is typically used for any simulation where large turbulence exists in the flow. Highly turbulent flow can have eddies with a wide range of length and time scales. Directly solving these eddies is called Direct Numerical Simulation (DNS) and is not computationally practical as the range of

eddies scales with the cube of the Reynolds number (ANSYS Inc. 2011). This requires a drastic increase in element count as the Reynolds number is increased, limiting the practical implementation of DNS. RANS and LES models solve this impracticality by limiting their eddy calculation focus. The reasoning for this is that smaller eddies are less dependent on flow conditions and are more isotropic. This allows for some approximation when calculating these smaller eddies. The fundamental difference between LES and RANS models is their strictness in filtering out their eddy calculations. LES still calculates the properties of large eddies in a flow and has looser restrictions to what it defines as "large" eddies. RANS models focus primarily on eddies closer to a wall, where eddies in the surrounding flow are filtered out based on their approximated effect on the flow field. The two main variations of the RANS model are the $k-\omega$ and $k-\varepsilon$ models. The $k-\omega$ model places an even greater focus on turbulence calculation within the boundary layer, whereas the $k-\varepsilon$ model places greater emphasis on larger turbulence in the surrounding flow field.

Due to the focus of this study being on the turbulent boundary layer around the wing surface the $k-\omega$ model is desirable for this study. The standard $k-\omega$ model is an empirical model based on the model transport equations for turbulence kinetic energy (k) and specific dissipation rate (ω) (Wilcox 2001). The turbulence kinetic energy, k, and the specific dissipation rate, ω, are obtained form the following transport equations (ANSYS Inc. 2011):

$$\frac{\partial}{\partial t}(pk)+\frac{\partial}{\partial x_i}(pku_i)=\frac{\partial}{\partial x_j}\left(\Gamma_k\frac{\partial k}{\partial x_j}\right)+G_k-Y_k+S_k \tag{3.2.1}$$

and

$$\frac{\partial}{\partial t}(p\omega)+\frac{\partial}{\partial x_i}(p\omega u_i)=\frac{\partial}{\partial x_j}\left(\Gamma_\omega\frac{\partial \omega}{\partial x_j}\right)+G_\omega-Y_\omega+S_\omega \tag{3.2.2}$$

In these equations, G_k represents the generation of turbulence kinetic energy due to mean velocity gradients, and G_ω represents the generation of ω. Γ_k and Γ_ω represent the effective diffusivity of k and ω respectively. Y_k and Y_ω represent the dissipation of k and ω due to turbulence. S_k and S_ω are user-defined source terms. All the above terms are calculated using the following equations:

$$\Gamma_k = \mu + \frac{\mu_t}{\sigma_k} \tag{3.2.3}$$

$$\Gamma_\omega = \mu + \frac{\mu_t}{\sigma_\omega} \tag{3.2.4}$$

where σ_k and σ_ω are the turbulent Prandtl numbers for k and ω. The turbulent viscosity, μ_t is computed as follows:

$$\mu_t = \alpha^* \frac{\rho k}{\omega} \tag{3.2.5}$$

The coefficient α^* damps the turbulent viscosity, causing a low-Reynolds-number correction to be needed. This coefficient is defined as:

$$\alpha^* = \alpha^*_\infty \left(\frac{\alpha^*_0 + Re_t/R_k}{1 + Re_t/R_k}\right) \tag{3.2.6}$$

For calculating the production of k, the term G_k represents the production of turbulence kinetic energy. This term is defined as:

$$G_k = -\rho \overline{u_i' u_j'} \frac{\partial u_j}{\partial x_i} \tag{3.2.7}$$

The production of ω is given by:

$$G_\omega = \alpha \frac{\omega}{k} G_k \tag{3.2.8}$$

where the coefficient α is given by:

$$\alpha = \frac{\alpha_\infty}{\alpha^*} \left(\frac{\alpha_0 + Re_t/R_\omega}{1 + Re_t/R_\omega}\right) \tag{3.2.9}$$

where R_ω = 2.95. The dissipation of k is given by:

$$Y_k = \rho \beta^* f_{\beta^*} k\omega$$

Where:

$$f_{\beta^*} = \begin{cases} 1 & x_k \leq 0 \\ \frac{1+680x_k^2}{1+400x_k^2} & x_k > 0 \end{cases} \quad (3.2.10)$$

$$x_k \equiv \frac{1}{\omega^3}\frac{\partial k}{\partial x_j}\frac{\partial \omega}{\partial x_j} \quad (3.2.11)$$

$$\beta^* = \beta_i^*[1 + \zeta^* F(M_t)] \quad (3.2.12)$$

$$\beta_i^* = \beta_\infty^* \left(\frac{4/15+(Re_t/R_\beta)^4}{1+(Re_t/R_\beta)^4}\right) \quad (3.2.13)$$

The dissipation of ω is given by:

$$Y_\omega = \rho\beta f_\beta \omega^2 \quad (3.2.14)$$

where

$$f_\beta = \frac{1+70x_\omega}{1+80x_\omega} \quad (3.2.15)$$

$$x_\omega = \left|\frac{\Omega_{ij}\Omega_{jk}S_{ki}}{(\beta_\infty^*\omega)^3}\right| \quad (3.2.16)$$

$$\Omega_{ij} = \frac{1}{2}\left(\frac{\partial u_i}{\partial x_j} - \frac{\partial u_j}{\partial x_i}\right) \quad (3.2.17)$$

and

$$\beta = \beta_i\left[1 - \frac{\beta_i^*}{\beta_i}\zeta^* F(M_t)\right] \quad (3.2.18)$$

where the compressibility function, $F(M_t)$ is given by:

$$F(M_t) = \begin{cases} 0 & M_t \leq M_{t0} \\ M_t^2 - M_{t0}^2 & M_t > M_{t0} \end{cases} \quad (3.2.19)$$

3.3 Flow Properties and Airfoil

A key aspect of this research is to keep the simulation conditions used simple to create replicability. Because of this, analysis was done at a low Reynolds number to avoid compressibility effects. This also allows for easy wind tunnel testing to validate the simulation results. An added benefit to performing this simulation for low-Reynolds flow is a drastic reduction in computational time, which is one driving aspect of this research. Fluid flow at standard sea level (SSL) conditions at are used for this research to convey the aeroelastic effects of a wing under viscous dominant flow. The velocities chose are for the Reynolds number of each flow to equal 6.0E+5, 8.0E+5, 1.0E+6, and 1.2E+6. The fluid properties and wing dimensions used to achieve this Reynolds number are shown in **Table 3.3.1** below.

Table 3.3.1: Simulation Fluid Properties and Wing Geometry for NACA 0012 Wing

Density:	1.225	kg/m^3
Chord:	0.4	m
Dynamic Viscosity:	1.81E-5	Pa*s
Span	1.2	m
Velocities	22.04; 29.39; 36.73; 44.08	m/s
Aspect Ratio	3	

The airfoil chosen for aeroelastic analysis in this research was the NACA 0012 airfoil. This is due to the simplistic nature of this airfoil. The NACA 0012 airfoil is symmetrical, meaning it has no camber and produces no lift at an angle of attack of 0°. This airfoil is also relatively thin,

with lower curvature than cambered airfoils, meaning it takes lower computational power to simulate than traditional cambered airfoils. Due to its simplistic nature, results gained using this airfoil are comparable to other traditional airfoils and wing shapes, albeit generally. Due to its replicability and simplicity, it is the most common airfoil that is tested in the field of aerospace research. (Mahato et al. 2023; Srinivasa Rao, Mahapatra, and Chaitanya Mangavelli 2018; Chen et al. 2022; Chang et al. 2022; Akbari and Price 2003; Han et al. 2021).

The coordinates on the X and Y plane for a NACA 0012 airfoil were gathered from the UIUC Airfoil Coordinates Database (UIUC Applied Aerodynamics Group 2023). These coordinates are determined by using the following definition to generate a 2D curve with a chord length of 1 m.

$$y = 0.6(0.2969\sqrt{x} - 0.1260x - 0.3516x^2 + 0.2843x^3 - 0.1015x^4) \quad (3.3.1)$$

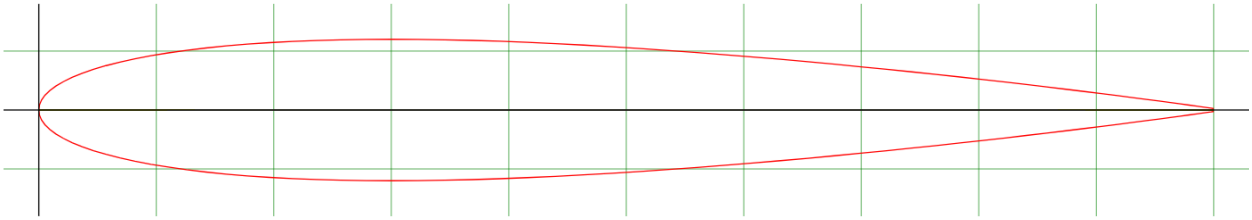

Figure 3.3.1: NACA 0012 Airfoil Plot

3.4 Non-Dimensional Parameters and Aerodynamic Similarity Criterion

In the field of aerospace, many relevant values such as pressure, lift, and drag are non-dimensionalized to allow for easy comparison between models. These values are referred to as coefficients. The value that makes this easy comparison possible is a value known as Reynolds Number. Reynolds number (Re) is a non-dimensional value that characterizes the viscous properties of a fluid flow, which is calculated using equation 1 below: (Anderson 2012)

$$Re = \frac{\rho v l}{\mu} \tag{3.4.1}$$

Where:

- v = the velocity of the fluid in m/s
- ρ = the density of the fluid in kg/m^3
- l = the characteristic length, the chord length of an airfoil
- μ = the fluid dynamic viscosity in kg/(m*s)

Even if an airfoil is scaled up to ten times its original size, if the Reynolds number of the flow is the same, the aerodynamic characteristics will also be identical. This means the coefficients of lift, drag, pressure, etc. will also be identical between the two models if the fluid is still incompressible.

As the speed of a fluid increases and becomes incompressible, the viscous effects of the fluid start to matter less to the aerodynamic performance as the behavior of the air molecules start to change. Once the fluid starts to become compressible, the speed of fluid relative to the speed of sound becomes the driving factor for the aerodynamic properties. The value that corresponds to the characteristics of the fluid at these speeds is known as the Mach number (M), which is a ratio of the local flow velocity over the speed of sound through that fluid. The Mach number, like the Reynolds number, is also non-dimensionalized. The Mach number at which a fluid is compressible is typically considered to be 0.8. (Anderson 2012)

$$Ma = \frac{u}{c_s} \tag{3.4.2}$$

An additional non-dimensional value that is used in computational fluid dynamics specifically is the y^+ value. y^+ is the distance based on the local cell fluid velocity and is associated

with the resolution and convergence of a mesh grid. It is a dimensionless distance from the surface wall of a fluid boundary to the first node in the mesh. This value is calculated using the following equation:

$$y^+ = \frac{u_* y}{\nu} \tag{3.4.3}$$

Where u_* is the friction velocity at the wall and y is the perpendicular distance from the wall to the nearest node. (Ferziger and Perić 2002). The lift and drag forces as well as pressure acting on a wing or airfoil are also commonly non-dimensionalized (Anderson 2012). The non-dimensionalized versions for lift and drag force are defined using the following equations:

$$C_L = \frac{L}{\frac{1}{2}\rho V^2 A} \tag{3.4.4}$$

$$C_D = \frac{D}{\frac{1}{2}\rho V^2 A} \tag{3.4.5}$$

where A is the cross-sectional area that the force is applied on, L is the force in the Y direction (lift), and D is the force in the X direction (drag). The capitol L and D in these equations denote that the lift and drag coefficients are for a 3D, finite wing. For a 2D airfoil, the L and D are lowercase, and the chord length is used as the reference length as opposed to A for a finite wing. Another commonly used coefficient is the pressure coefficient, C_p. This coefficient is given by:

$$C_p = \frac{p - p_\infty}{\frac{1}{2}\rho V^2} \tag{3.4.6}$$

where p_∞ is the total freestream pressure. Due to its commonality between equations, the term $\frac{1}{2}\rho V^2$ is typically referred to only as dynamic pressure, q. (Anderson 2012)

3.5 Model Geometry Characteristics

To generate the geometry model of the 3D wing, this curve is imported into ANSYS Design Modeler and extruded by 3m to create a solid wing, which is then scaled down by 0.4 to have a chord of 0.4 m and a wingspan of 1.2 m. For different angles of attack, the wing is rotated about the leading edge of the wing. This wing geometry is used for the CSD simulation, however the CFD simulation requires a fluid boundary as well. To create this fluid boundary, a 3 m x 4 m box is created around the wing, with the leading edge at the leftmost center of the box. A half-circle with a radius of 2 m is created at the leftmost edge of the box. This resulting shape is then extruded by 2 m. The wing geometry is then subtracted from the extruded box to complete the fluid boundary geometry.

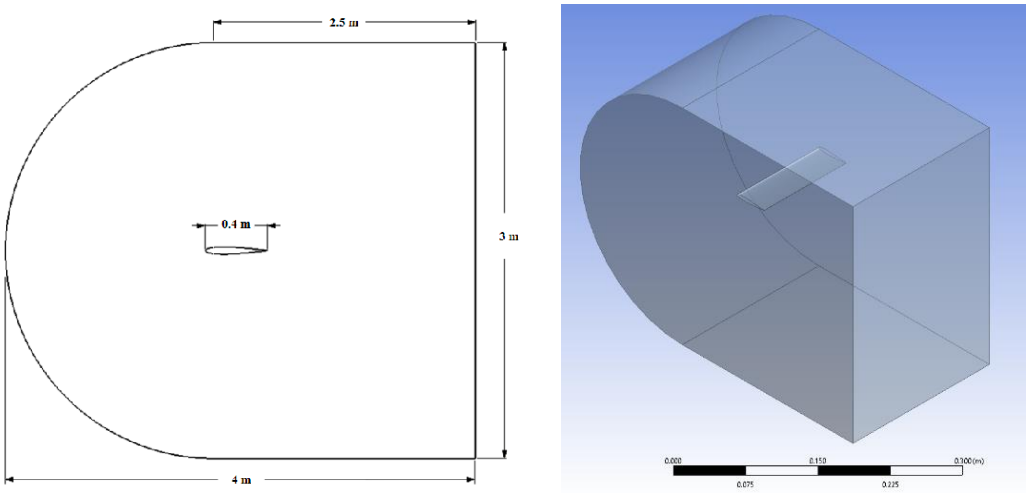

Figure 3.5.1: Fluid Domain Geometry; 2D Side View (Left), and 3D Isometric View (Right)

3.6 Mesh Generation

This geometry is imported into ANSYS Fluent Meshing for the meshing process. The mesh at the wing surface is meshed first to achieve the desired y+ value. For highly viscous dominant flow, a y+ value less than 1 is ideal, however a y+ value between 1 and 30 is considered appropriate. (ANSYS Inc. 2011). Due to the large computational time of the CFD/CSD simulation and the purpose of this research, a y+ value of 1 is used for this application to keep computational time to an achievable amount. To achieve a y+ value of 1, the following equations were used to determine an approximation of the needed mesh sizing at the wall based on flat plate boundary layer theory. (White 2002)

$$C_f = \frac{0.026}{Re^{1/7}} \tag{3.6.1}$$

$$\tau_{wall} = \frac{C_f \rho U_{inf}{}^2}{2} \tag{3.6.2}$$

$$u^* = \sqrt{\frac{\tau_{wall}}{\rho}} \tag{3.6.3}$$

$$\Delta s = \frac{y^+ \mu}{u^* \rho} \tag{3.6.4}$$

Where C_f is the coefficient of friction, τ_{wall} is the shear at the wall, and Δs is the wall spacing. Using these equations, the desired wall spacing to achieve a y+ value of 10 is 1.5E-05m. 6 Inflation layers with a first layer thickness of 1.5E-05 m were added at the wing surface to produce a smooth transition from boundary layer to surrounding volume. To show that this mesh is converged, a

series of simulations were run at Re = 1.2E+06 and α = 6° starting with a surface element size of 0.007 m, and the maximum velocity around the wing was taken. This was repeated until the maximum velocity converged, resulting in the following values:

Table 3.6.1: Element Size vs Maximum Velocity

Element Size at Wing Surface (m)	Maximum Velocity (m/s)
0.007	5.20E+1
0.0025	5.36E+1
0.003	5.79E+1
0.005	5.83E+1
0.007	5.83E+1

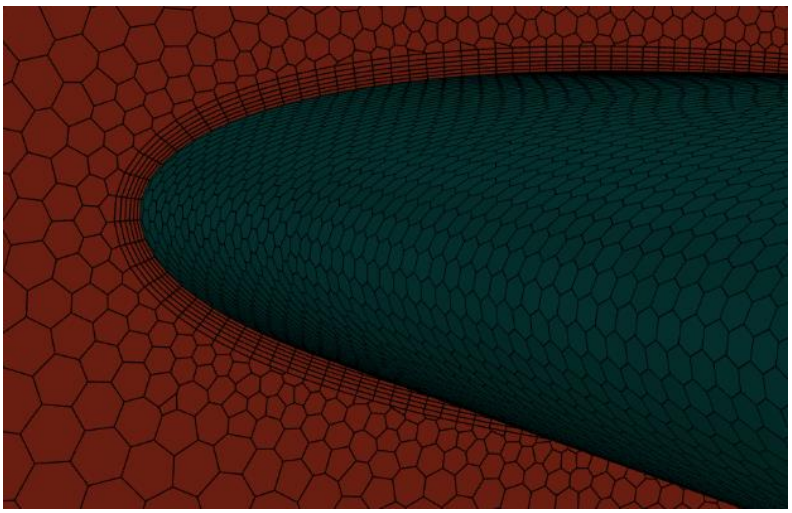

Figure 3.6.1: Mesh Resolution at Wing Surface

For the remainder of the volume mesh, a growth rate of 1.1 per layer was applied with a maximum mesh size of 0.7m. For the element order, linear is chosen due to the drastic increase in computational time that quadratic elements because. This element type in ANSYS ADPL is labeled as FLUID 142, which is a linear 3D element for fluid dynamics calculations. (ANSYS Inc. 2012). Due to this limitation, polyhedral elements are used as opposed to hexagonal due to the increased accuracy that polyhedral elements provide over hexagonal.

Mesh quality can be assessed through both skewness and orthogonality. Skewness refers to how close a cell is to its ideal shape. For example, in the case of 3D hexahedral elements, a cube or rectangular prism will have higher skewness when compared to a rhombus element shape. Orthogonality is related to the angle between the vector connecting two ajacent cell centers and the normal vector of the face shared by these two cells. Two rectangular prisms adjacent to each other will have a low orthogonality compared to two extruded rhombuses. When creating a mesh where a domain exhibits any amount of curvature, it is nearly impossible for every element in the mesh to have an ideal skewness. For a 3D mesh, a maximum skewness of less than 0.9 with an average skewness less than 0.4 are ideal. The ideal average orthogonal quality is 1. (ANSYS Inc. 2011)

Table 3.6.2: Fluid Domain Mesh Statistics

Size at wing surface	1.5E-05 m
y+	0.5 (Average), 0.9 (maximum)
Growth rate	1.1
Element number	3092485
Element type	Polyhedra (Fluid142)
Element order	Linear

Max. skewness	0.751
Average skewness	0.01932
Average orthogonal quality	0.97565
Inflation layer #	6
Inf. layer growth rate	1.1

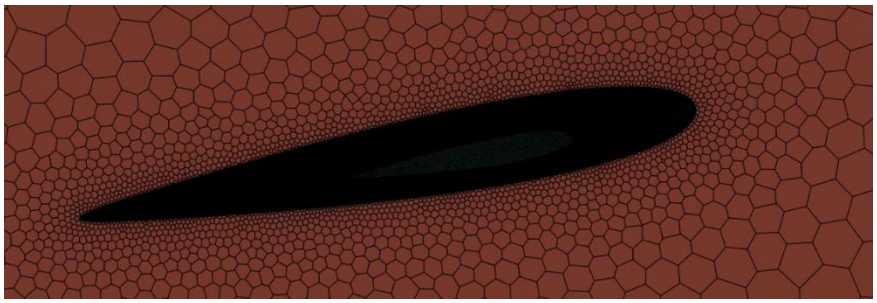

Figure 3.6.2: Mesh Resolution Near Wing Surface (α = 10° Shown)

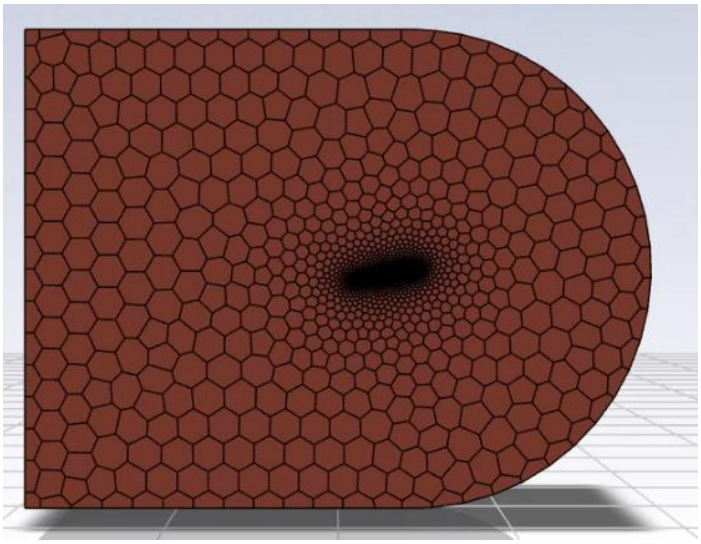

Figure 3.6.3: Total Volume Mesh Resolution (α = 10° Shown)

3.7 Boundary Conditions

For the boundary conditions of the fluid domain, the front face of the domain is made an inlet with an X velocity of 18.5 m/s, and the back face is made a pressure outlet with a gauge pressure of 0 Pa. The top and bottom faces of the boundary, as well as the wing surface, are walls with the no-slip boundary condition. The remaining walls are selected as symmetrical boundaries to avoid wall interference at the wing base and tip. A fluid-structure interaction boundary condition is also added to the wing surface and dynamic remeshing is applied to the wing surface. To save on computational time, the dynamic meshing is set to only re-mesh the portions of the mesh that exhibit deformation, as opposed to the entire mesh.

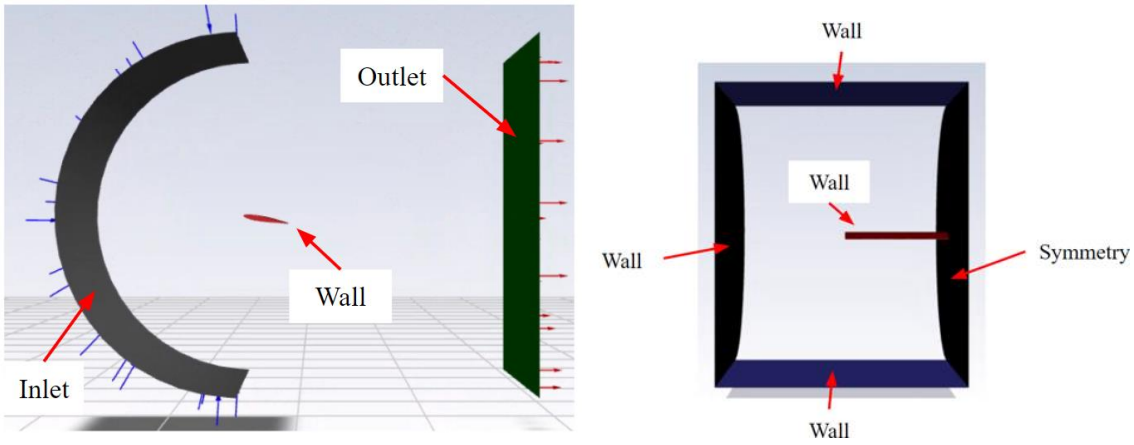

Figure 3.7.1: Boundary Conditions for Fluid Domain; Side View (Left) and Front View (Right)

3.8 Computational Models

The CFD computational model used for solving the turbulence model is RANS k-omega SST. This model was chosen since the fluid flow is at a low Reynolds number and viscous dominant with low amounts of turbulence, and the fluid properties and turbulence close to the wing wall are the focus. The simple wing shape used for the simulations also contributes to higher

accuracy of the RANS turbulence model (Rahman 2023; Bellegoni et al. 2023). This model also provides lower computational cost than that of the LES turbulence model. For more complex geometry than the model tested in this thesis, an LES model may be needed to provide more accurate results. For this research, however, it is deemed that the use of the RANS turbulence model is appropriate (Ilie 2019b).

The basic, discretized forms of the equations used for the RANS k-ω SST model are: (F. R. Menter 1994; 1993; ANSYS Inc. 2011)

$$\nu_T = \frac{a_1 k}{max\left(a_1\omega, SF_2\right)} \tag{3.8.1}$$

$$\frac{\partial k}{\partial t} + U_j\frac{\partial k}{\partial x_j} = P_k - \beta^* k\omega + \frac{\partial}{\partial x_j}\left[\left(\nu + \sigma_k\nu_T\right)\frac{\partial k}{\partial x_j}\right] \tag{3.8.2}$$

$$\frac{\partial \omega}{\partial t} + U_j\frac{\partial \omega}{\partial x_j} = \alpha S^2 - \beta\omega^2 + \frac{\partial}{\partial x_j}\left[\left(\nu + \sigma_\omega\nu_T\right)\frac{\partial \omega}{\partial x_j}\right] + 2\left(1 - F_1\right)\sigma_{\omega 2}\frac{1}{\omega}\frac{\partial k}{\partial x_i}\frac{\partial \omega}{\partial x_i} \tag{3.8.3}$$

Where:

$$F_2 = \tanh\left[\left[max\left(\frac{2\sqrt{k}}{\beta^*\omega y'}, \frac{500\nu}{y^2\omega}\right)\right]^2\right] \tag{3.8.4}$$

$$P_k = min\left(\tau_{ij}\frac{\partial U_i}{\partial x_j}, 10\beta^* k\omega\right) \tag{3.8.5}$$

$$F_1 = \tanh\left\{\left\{min\left[max\left(\frac{\sqrt{k}}{\beta^*\omega y'}, \frac{500\nu}{y^2\omega}\right), \frac{4\sigma_{\omega 2}k}{CD_{k\omega}y^2}\right]\right\}^4\right\} \tag{3.8.6}$$

$$CD_{k\omega} = max\left(2\rho\sigma_{\omega 2}\frac{1}{\omega}\frac{\partial k}{\partial x_i}\frac{\partial \omega}{\partial x_i}, 10^{-10}\right) \tag{3.8.7}$$

$$\phi = \phi_1 F_1 + \phi_2\left(1 - F_1\right) \tag{3.8.8}$$

$$\alpha_1 = \frac{5}{9}, \alpha_2 = 0.44 \tag{3.8.9}$$

$$\beta_1 = \frac{3}{40}, \beta_2 = 0.0828 \tag{3.8.10}$$

$$\beta^* = \frac{9}{100} \tag{3.8.11}$$

$$\sigma_{k1} = 0.85, \sigma_{k2} = 1 \tag{3.8.12}$$

$$\sigma_{\omega 1} = 0.5, \sigma_{\omega 2} = 0.856 \tag{3.8.13}$$

The velocity and pressure of the system are coupled using the second-order PISO algorithm. This model is slower per iteration than the SIMPLE algorithm but is typically faster overall for steady-state simulations than the SIMPLE algorithm if there is no temperature change in the flow. The PISO algorithm consists of three major steps: the predictor step, the first corrector step, and the third corrector step. In the predictor step, the pressure field p^* is first guessed based on the previous time step's flow conditions to calculate the velocity field components u^* and v^* using a discretized momentum equation. The initial guess for the pressure field may or may not be correct, and the velocity components may not satisfy the continuity equation. If this is the case, correction factors for pressure and velocity are defined to solve the conservation of momentum equation: p', u', and v' respectively.

$$p' = p^{**} - p^* \tag{3.8.14}$$

$$u' = u^{**} - v^{*} \tag{3.8.15}$$

$$v' = v^{**} - v^{*} \tag{3.8.16}$$

Where p^{**}, u^{**}, and v^{**}, are the corrected pressure and velocity fields corresponding to the momentum equation. For the second corrector step this correction method is repeated using the corrected pressure and velocity fields respectively using additional correction factors p'', u'', and v''. The corrected pressure and velocity fields gained from this are denoted as p^{**}, u^{**}, and v^{**} in the following equations:

$$p^{***} = p^{**} - p''; \; p'' = p^{*} - p' \tag{3.8.17}$$

$$u^{***} = u^{**} - u''; \; u'' = u^{*} - u' \tag{3.8.18}$$

$$v^{***} = v^{**} - v''; \; v'' = v^{*} - v' \tag{3.8.19}$$

These two correction steps are repeated until a converged solution is found, or the desired iteration number is reached. Once this converged solution is reached, the boundary conditions of the model are updated. (ANSYS Inc. 2011; Ferziger and Perić 2002; Sohail and Ullah 2017; Komen et al. 2021).

3.9 Simulation Setup

A separate simulation is performed for each angle of attack for each Reynolds number. The simulation is performed for 2,000 iterations. The residual plots for continuity, x-velocity, y-

velocity, z-velocity, k, and omega are gathered for each simulation to confirm flow convergence. An example of these residuals plot is shown below for the lowest and highest Re and α.

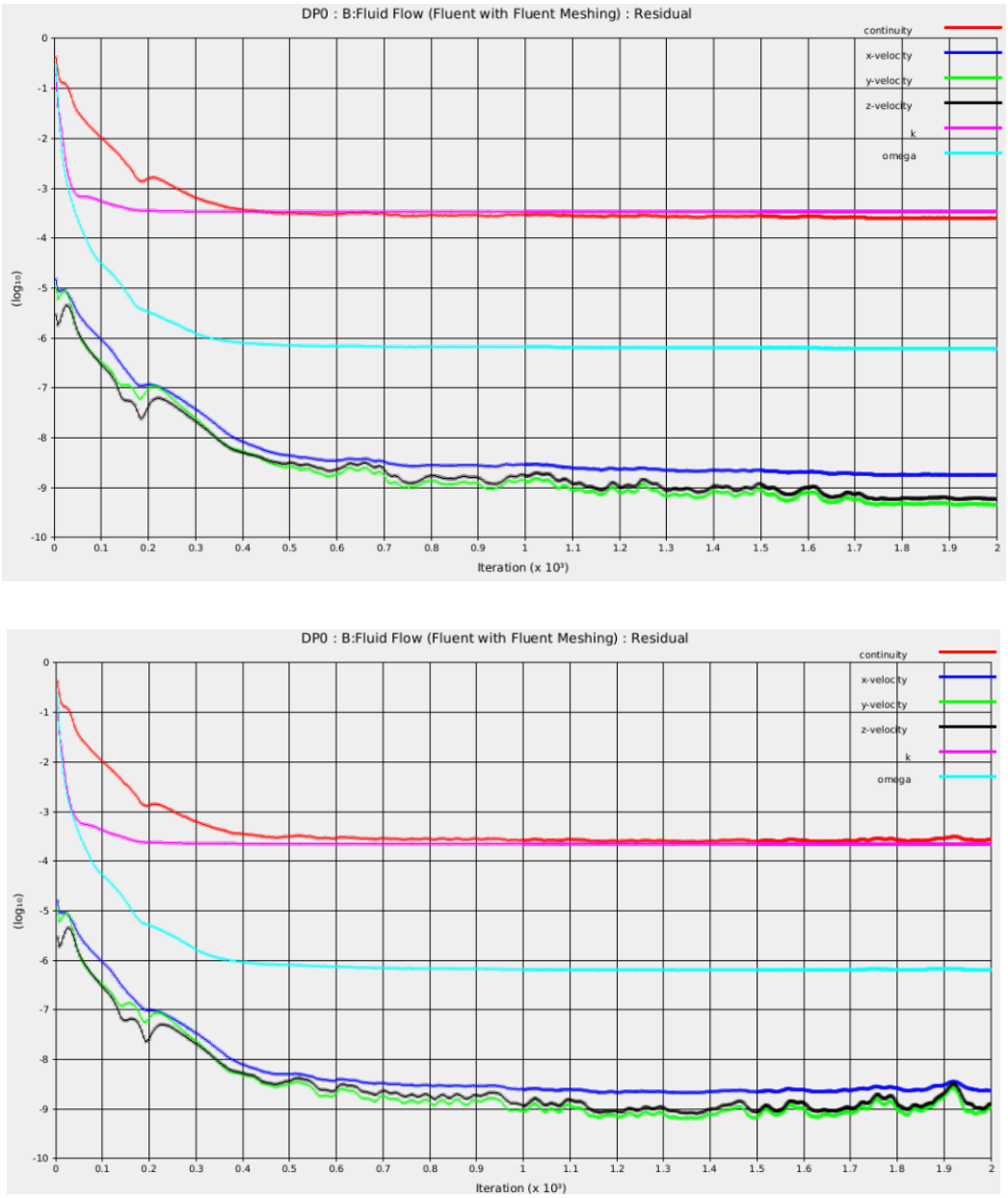

Figure 3.9.1: Residuals Plot for Re = 6.0E+5, α = 6° (Top); Re = 1.2E+6, α = 15° (Bottom)

CHAPTER 4

RESULTS AND DISCUSSION

The purpose of this study is to exemplify and show the differences in flow properties from increasing the flow velocity and angle of attack for a NACA 0012 airfoil. First an investigation into the aerodynamic forces, lift and drag, is performed. Then, the point at which the flow separates from the airfoil is then analyzed and compared at each angle of attack and flow velocity. Once these results are properly established, the corresponding pressure and velocity fields for each aoa and flow speed are compared, followed by the turbulence kinetic energy contour and wall shear vectors for each simulation.

4.1: Lift and Drag Coefficients

Using the equations for lift and drag found in chapter 3, the coefficients of lift and drag are calculated for each angle of attack and corresponding Reynolds number. These values are taken at half of the wingspan (0.6 m). These results are then plotted vs angle of attack for each simulation.

Table 4.1.1: Lift and Drag Coefficients vs Angle of attack for Re = 6.0E+5

α (°)	**C_L**	**C_D**	**C_L/C_D Ratio**
6	0.451	0.0168	26.85
9	0.668	0.0352	18.98
12	0.791	0.0580	13.64
15	0.698	0.175	3.99

Table 4.1.2: Lift and Drag Coefficients vs Angle of attack for Re = 8.0E+5

α (°)	C_L	C_D	L/D Ratio
6	0.452	0.0165	27.32
9	0.673	0.0339	19.83
12	0.834	0.0637	13.09
15	0.722	0.1599	4.51

Table 4.1.3: Lift and Drag Coefficients vs Angle of attack for Re = 1.0E+6

α (°)	C_L	C_D	L/D Ratio
6	0.457	0.0165	27.63
9	0.680	0.033	20.46
12	0.837	0.0581	14.41
15	0.753	0.1459	5.16

Table 4.1.4: Lift and Drag Coefficients vs Angle of attack for Re = 1.2E+6

α (°)	C_L	C_D	L/D Ratio
6	0.793	0.0165	27.85
9	0.458	0.0334	20.15
12	0.849	0.0584	14.55
15	0.789	0.1521	5.19

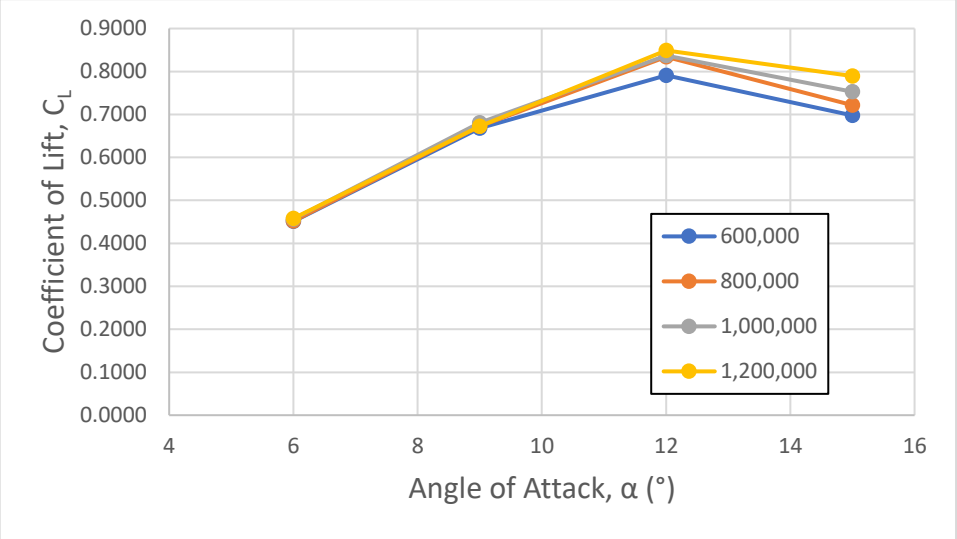

Figure 4.1.1: Lift Coefficient (C_L) vs Angle of Attack (α)

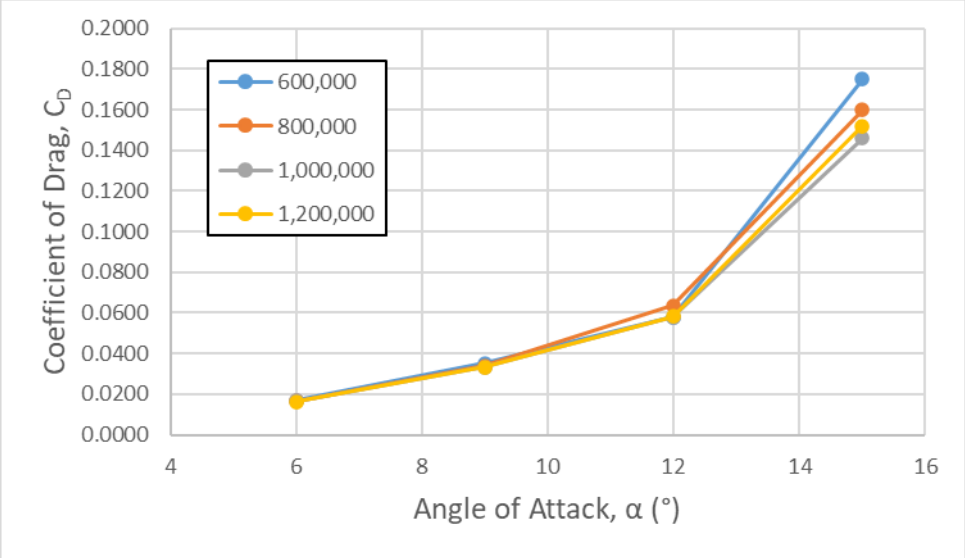

Figure 4.1.1: Drag Coefficient (C_D) vs Angle of Attack (α)

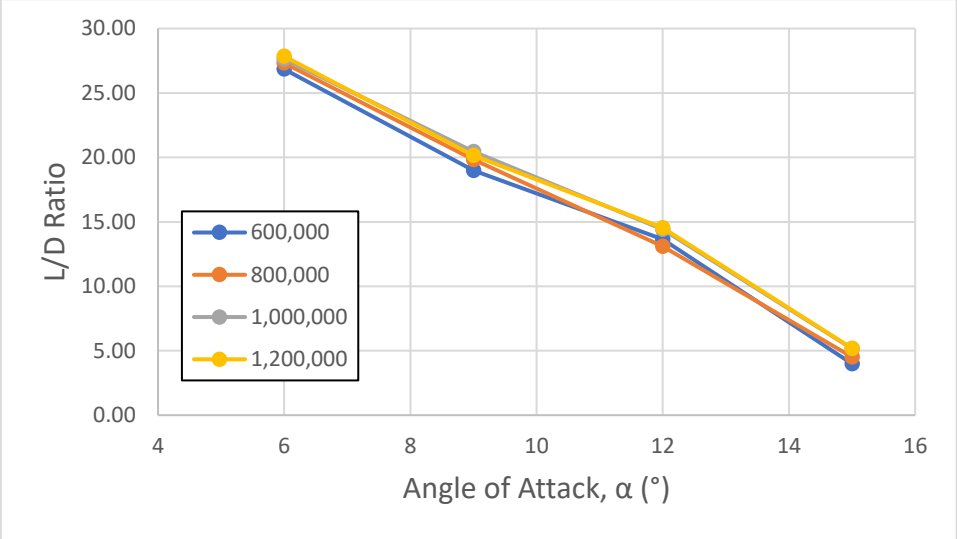

Figure 4.1.1: Lift-to-Drag Ratio vs Angle of Attack (α)

From these results, a sharp decline in lift can be seen once the angle of attack exceeds 12°, meaning that for each simulated flow velocity, the NACA 0012 stalls at between 12° and 15° with the lift for Re = 6.0E+5 falling slightly sooner than the other flow speeds. This aligns with expected results.

4.2: Pressure and Velocity

To properly compare the pressure and velocity fields at each aoa and velocity, Contours are created at the middle of the wingspan parallel to the X-Y plane for the velocity magnitude in m/s and the gauge pressure in Pa. For clarity, only the contours at a Reynolds number of 6.0E+5 and 1.2E+6 are shown in this section, as the differences are clearer. The contours for the other flow velocities not shown here will be shown in Appendix A.

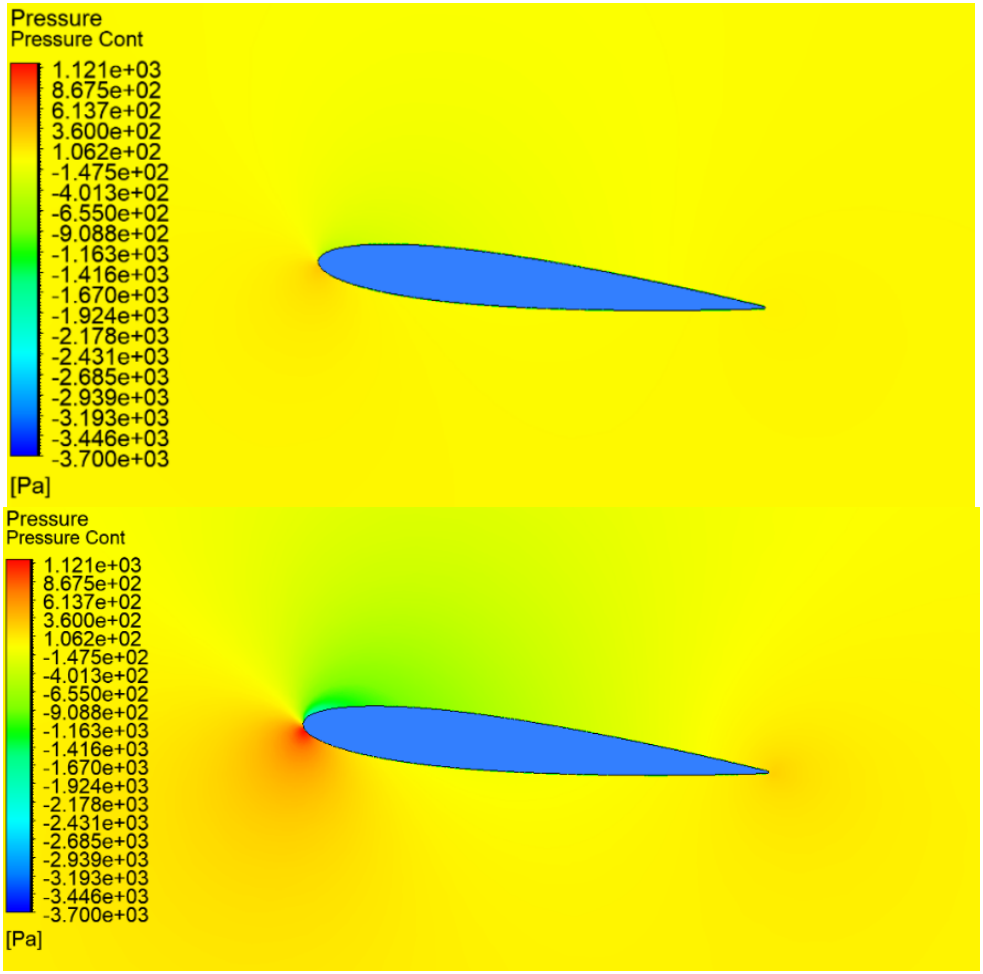

Figure 4.2.1: Gauge Pressure Contour at Alpha = 6°; Re = 6.0E+5 (Top) & Re= 1.2E+6 (Bottom)

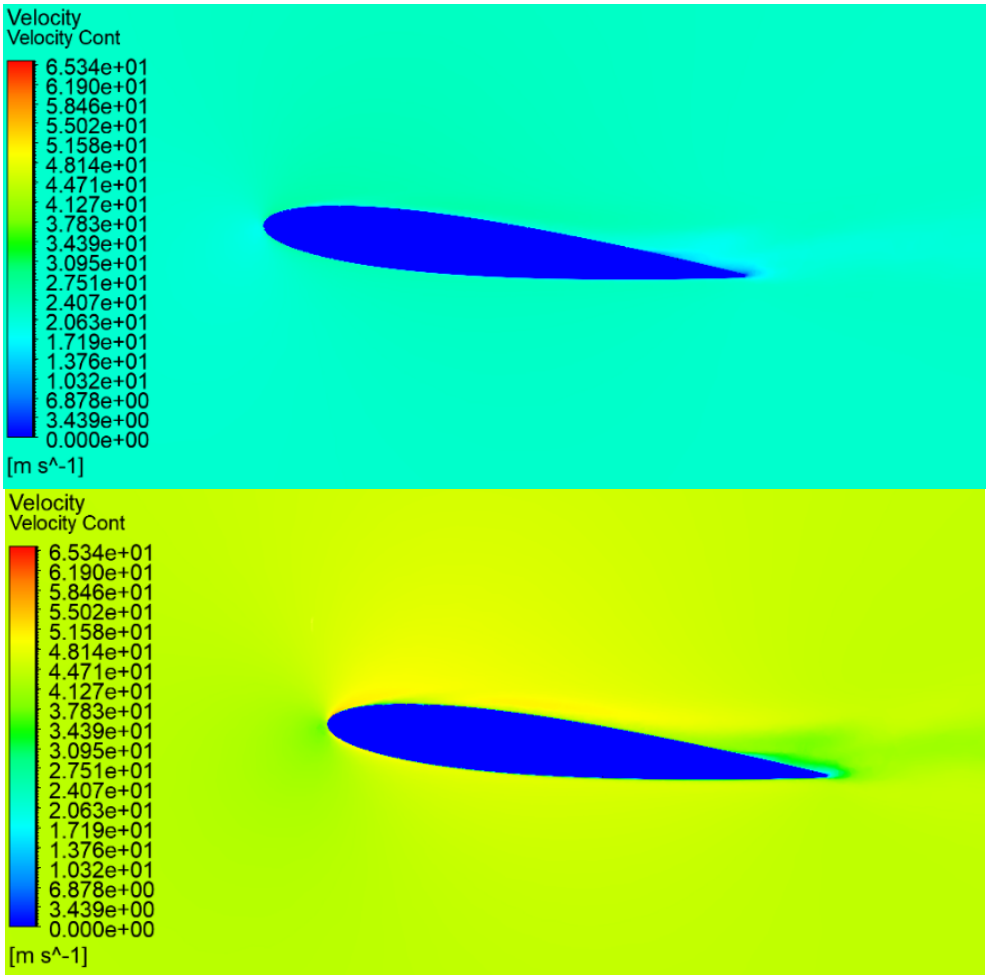

Figure 4.2.2: Velocity Contour at Alpha = 6°; Re = 6.0E+5 (Top) & Re= 1.2E+6 (Bottom)

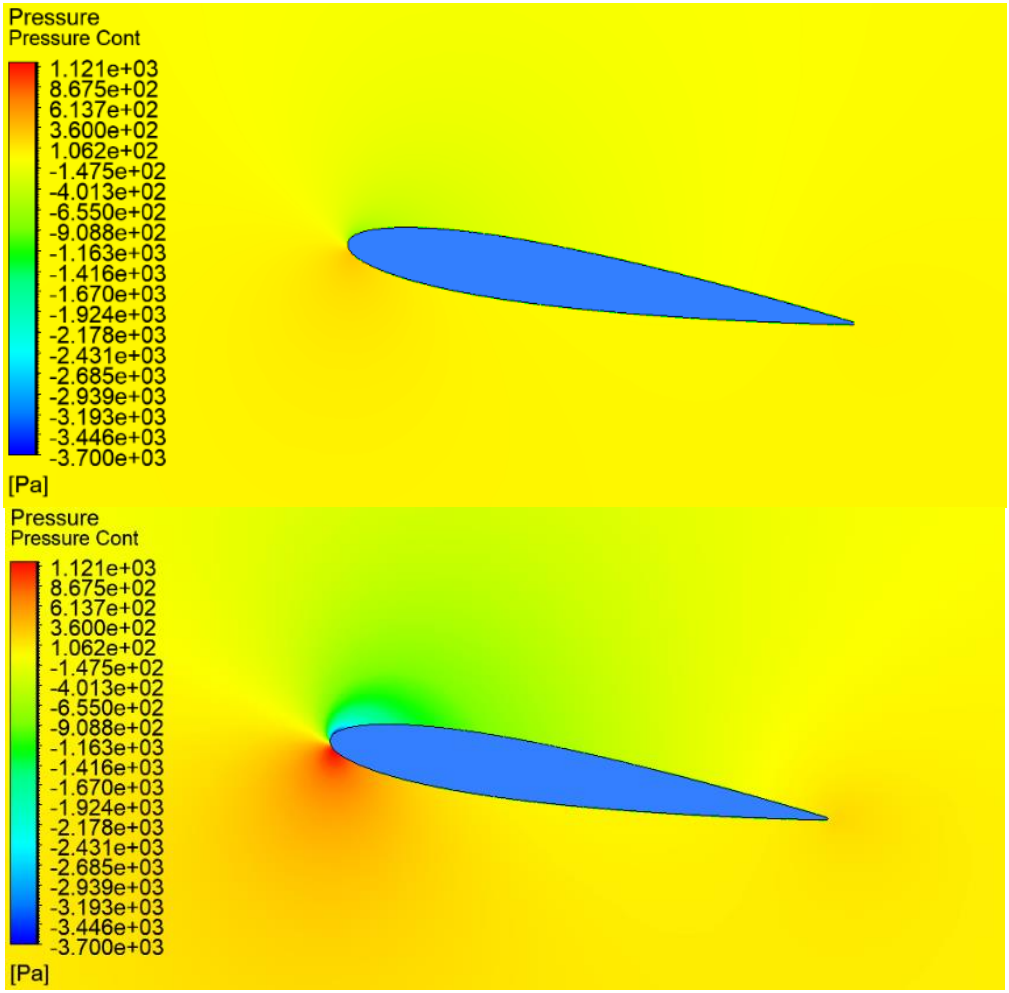

Figure 4.2.3: Gauge Pressure Contour at Alpha = 9°; Re = 6.0E+5 (Top) & Re= 1.2E+6 (Bottom)

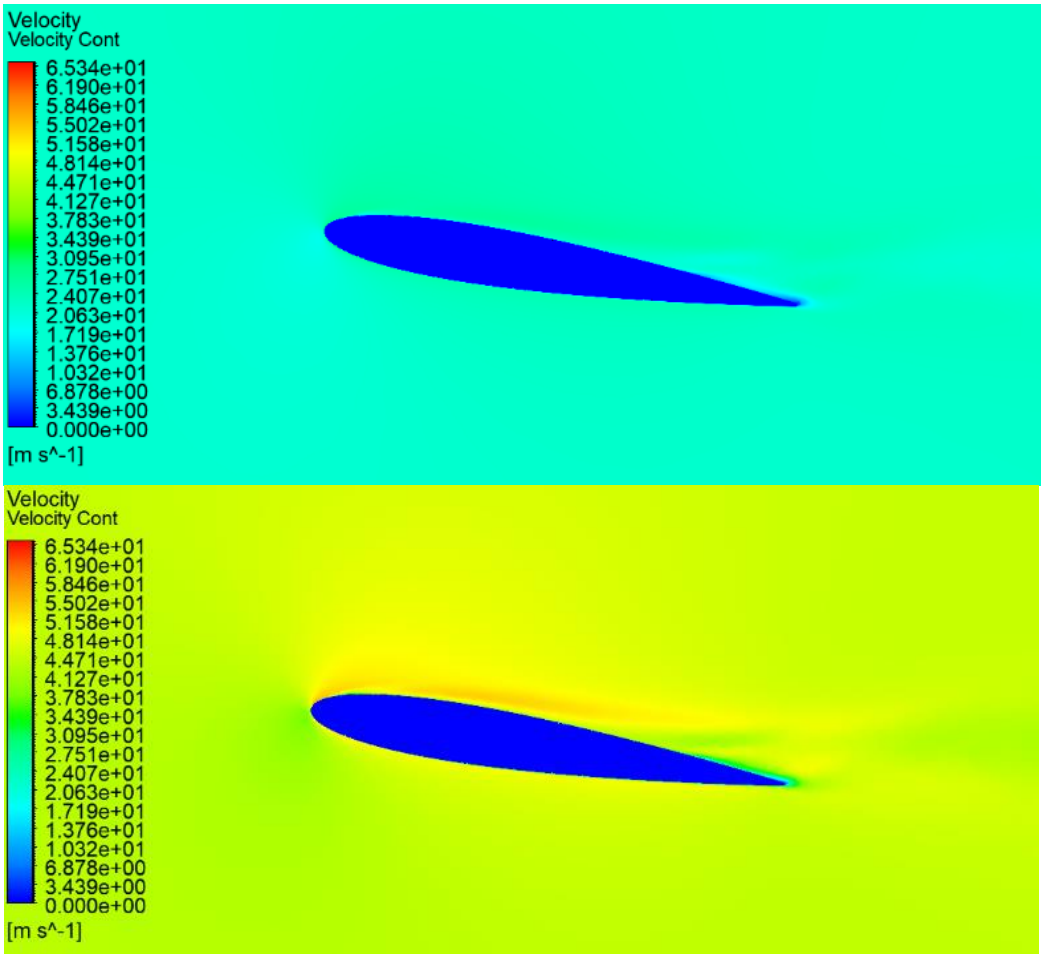

Figure 4.2.4: Velocity Contour at Alpha = 9°; Re = 6.0E+5 (Top) & Re= 1.2E+6 (Bottom)

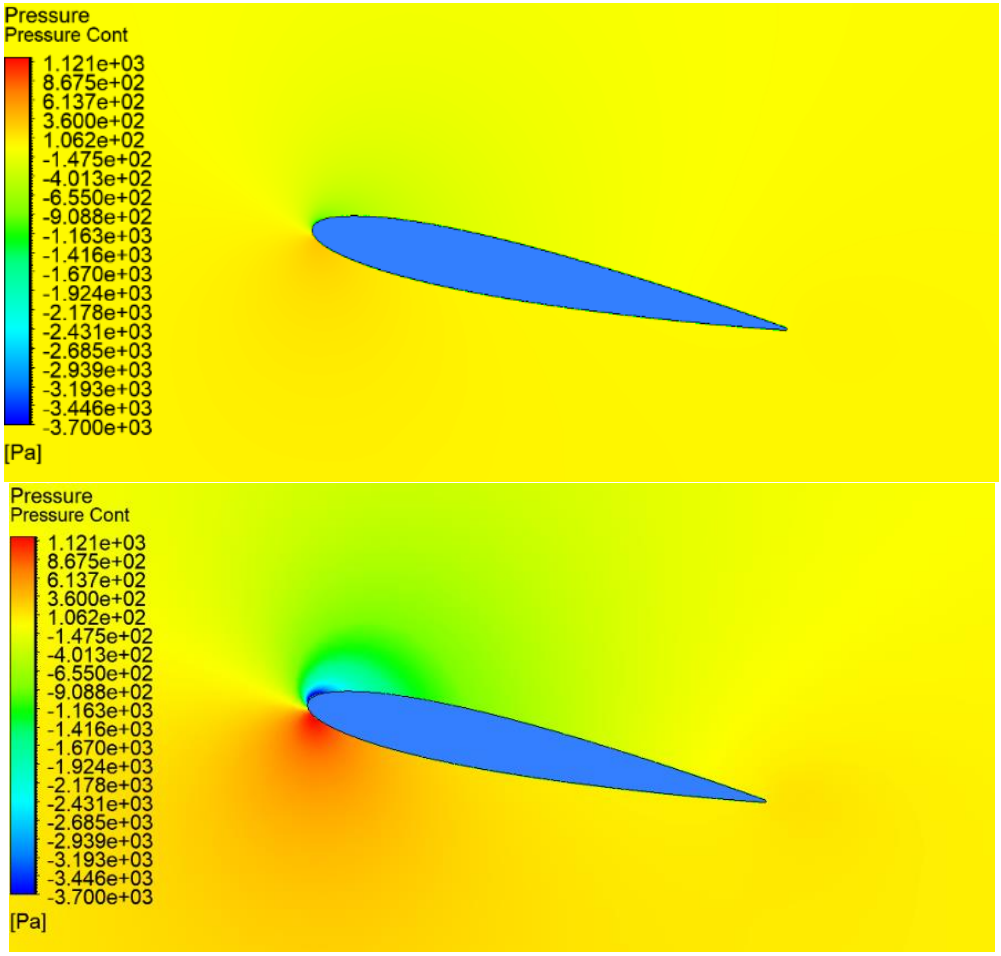

Figure 4.2.5: Gauge Pressure Contour at Alpha = 12°; Re = 6.0E+5 (Top) & Re= 1.2E+6 (Bottom)

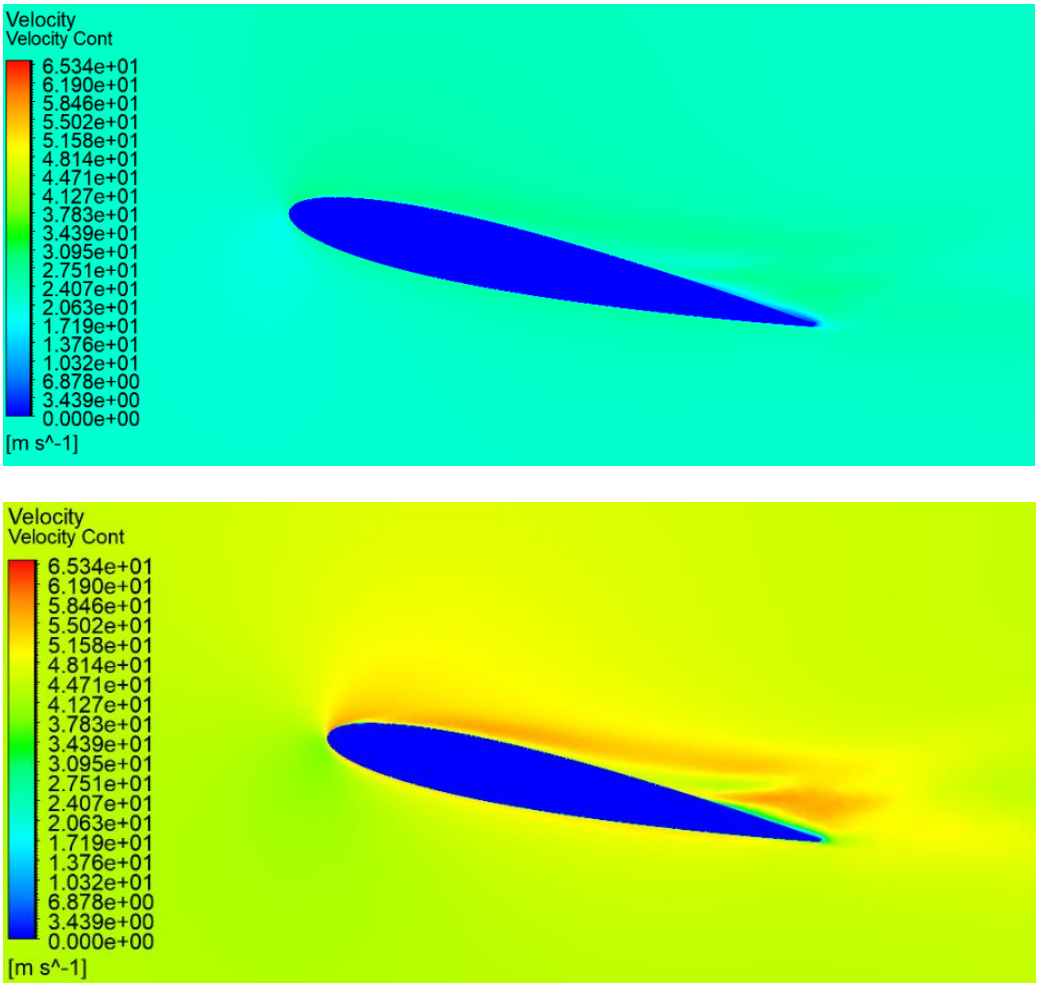

Figure 4.2.6: Velocity Contour at alpha = 12°; Re = 6.0E+5 (Top) & Re= 1.2E+6 (Bottom)

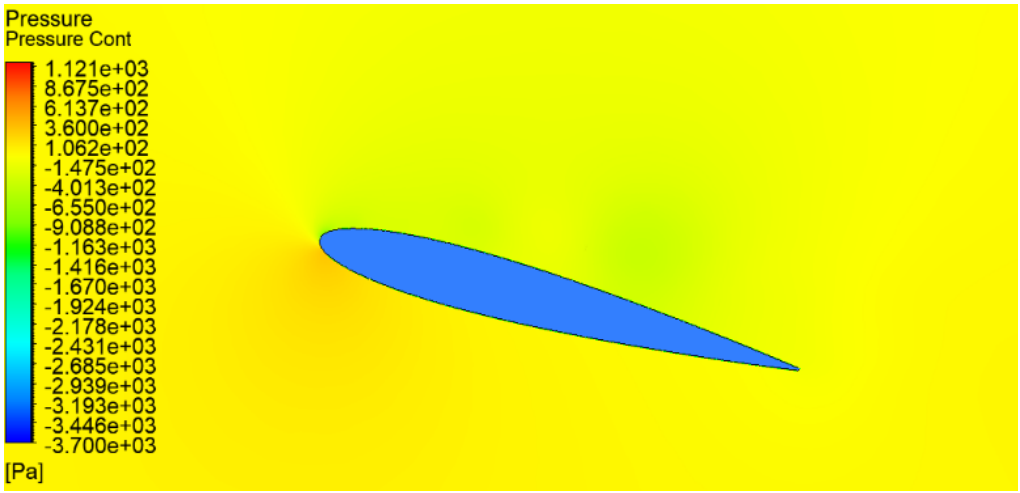

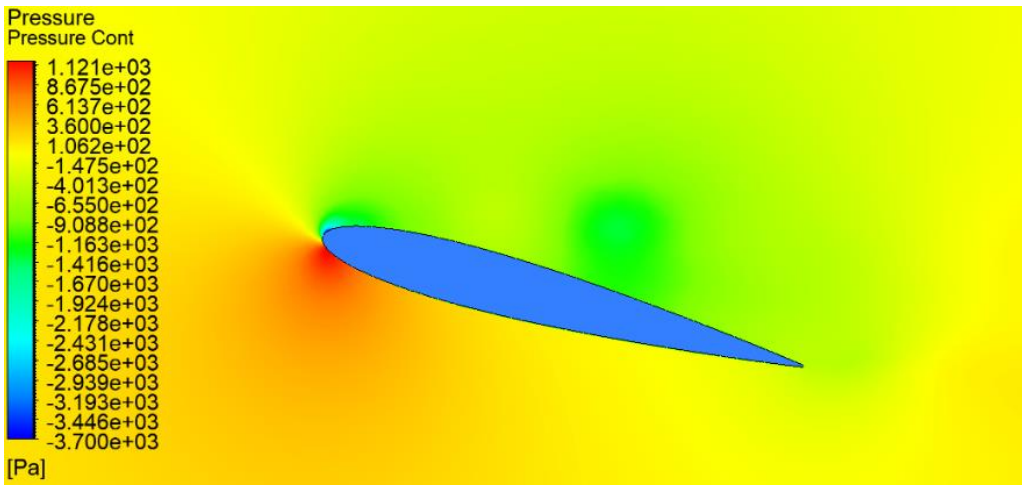

Figure 4.2.7: Gauge Pressure Contour at Alpha = 15°; Re = 6.0E+5 (Top) & Re= 1.2E+6 (Bottom)

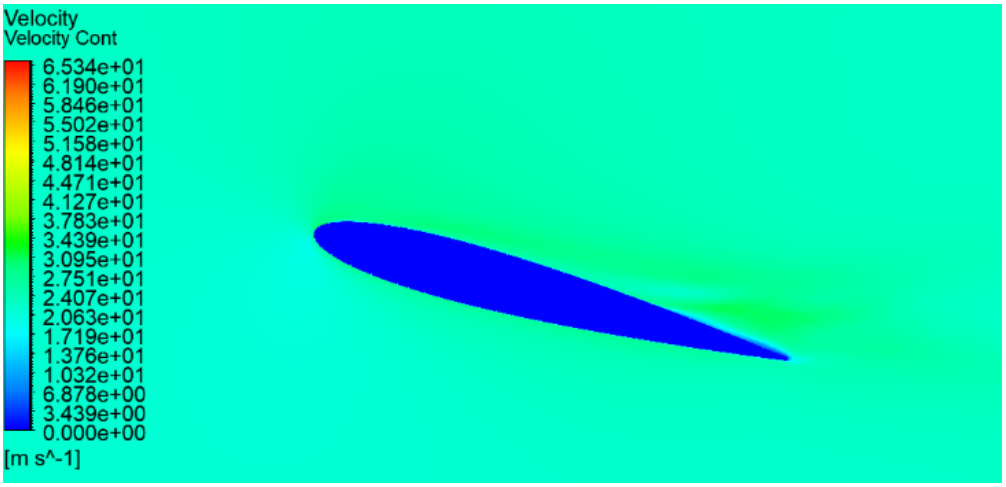

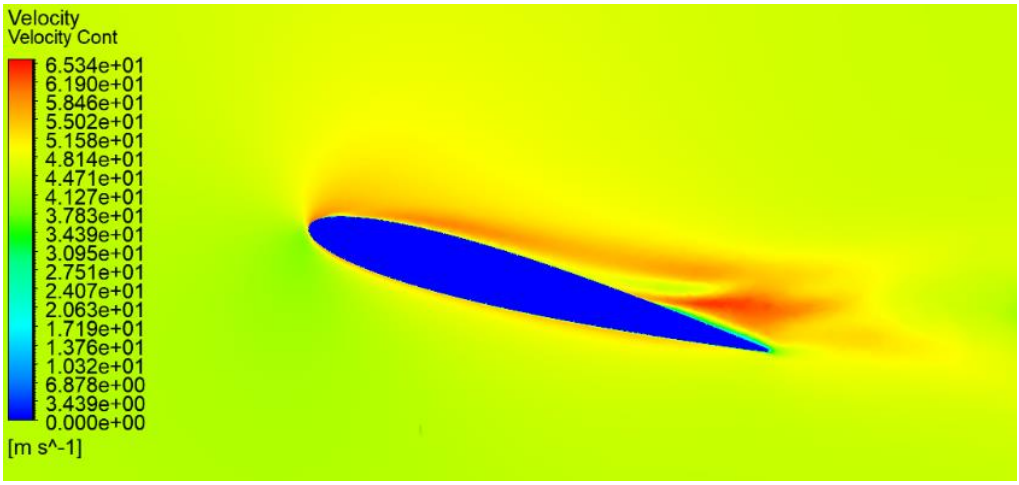

Figure 4.2.8: Velocity Contour at Alpha = 15°; Re = 6.0E+5 (Top) & Re= 1.2E+6 (Bottom)

As expected, the pressure and velocity fields differ greatly between the lower and higher Reynolds flows, as the flow speed is significantly higher for Re = 1.2E+6. For both flow speeds, flow separation can be seen once the angle of attack reaches and exceeds 9° as the wing approaches stall, with the separation being the clearest at alpha = 15°. In **Figure 4.2.5** a low pressure bubble can be seen for the Re = 1.2 million plot, signifying that the wing is approaching stall, which reflects the lift and drag coefficient results.

To visualize the point at which the flow separates from the wing and enters stall, the skin friction coefficient was plotted against the chord length for each simulation. The point at which the coefficient becomes negative shows the point at which the flow separates from the wing surface. An example plot is shown below:

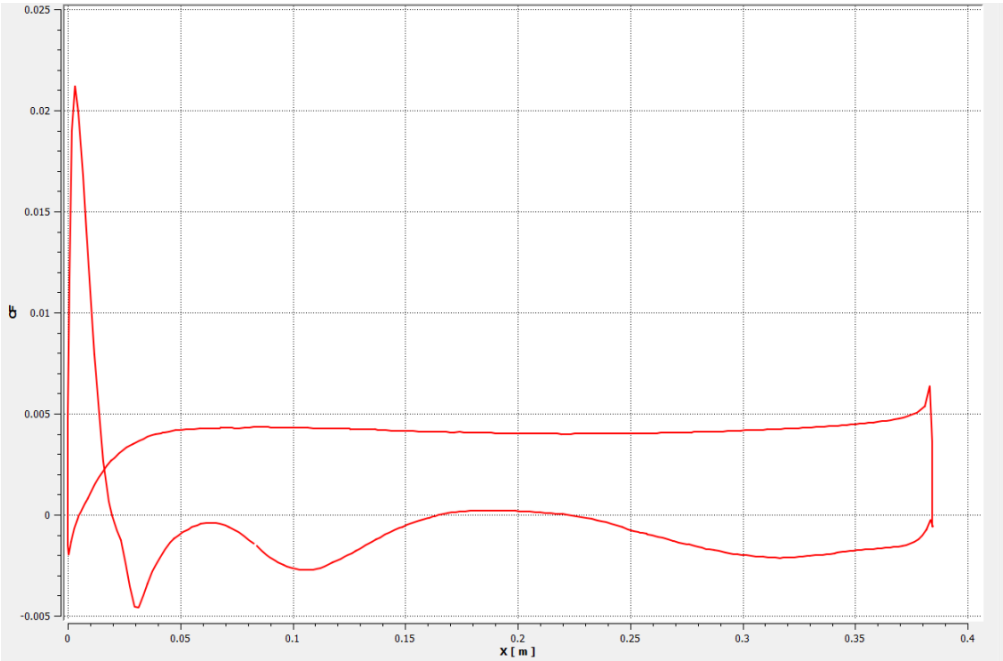

Figure 4.2.9: Pressure Coefficient (C_P) vs. Chord Length (m) for Re = 1.0E+6, Alpha = 15°

Based on this plot, flow separation begins at approximately x = 0.012 m away from the leading edge. The other pressure coefficient plots not shown here can be found in Appendix B. This point was recorded for each simulation and is shown in the table below. The streamline plot at this angle of attack and flow velocity clearly shows the flow separation and formation of vortices.

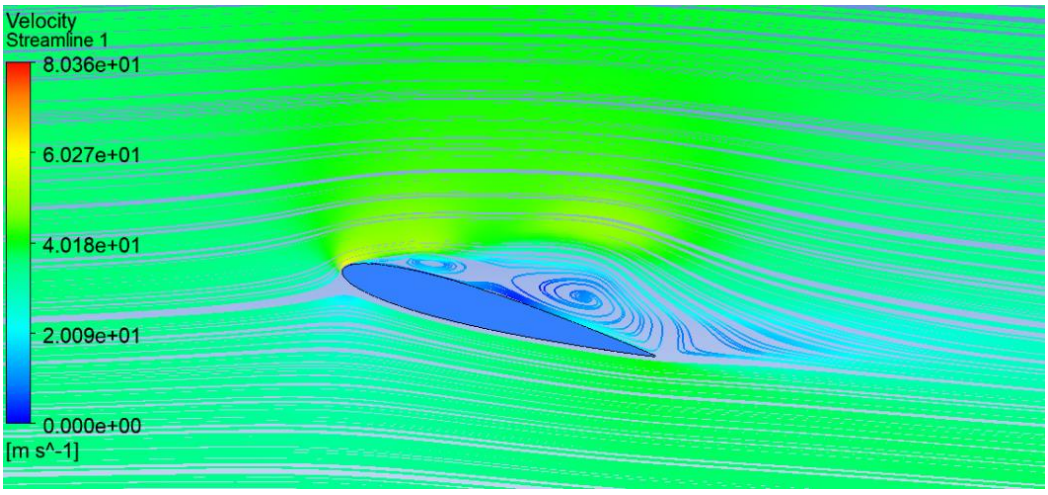

Figure 4.2.10: Flow Streamline plot for Alpha = 15°, Re = 1.0E+6

Each simulated wing shows flow separation once the angle of attack reached 15°. This aligns with the lift and drag coefficient results, as a sharp drop in lift and increase in drag can be observed as the angle of attack goes from 12° to 15°.

4.3: Turbulence Kinetic energy and Wall Shear

To further show the effects of increasing the angle of attack and airspeed, contour plots of the turbulence kinetic energy (TKE) and wall shear vector plots were created for each simulation. For the turbulence contour plots, only plots at $\alpha = 15°$ are shown, as there is very little turbulence around the wing before stall.

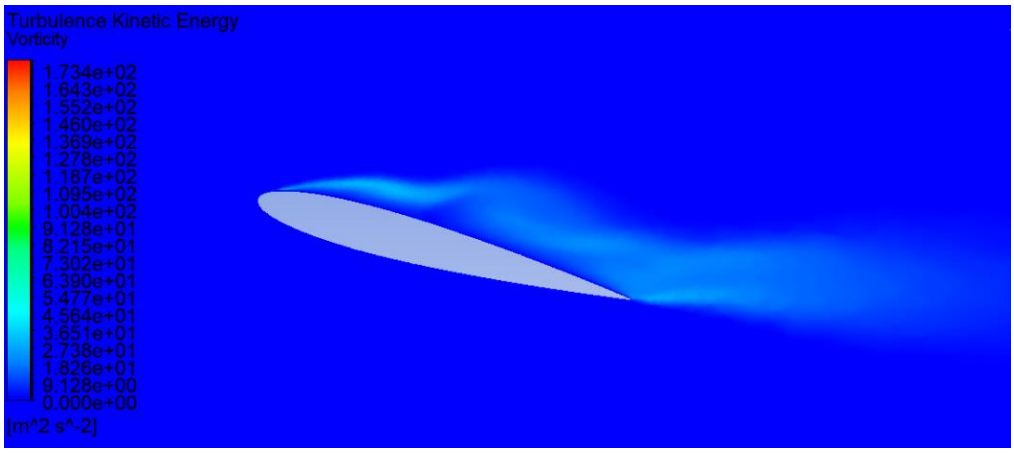

Figure 4.3.1: TKE Contour Plot for Alpha = 15°, Re = 6.0E+5

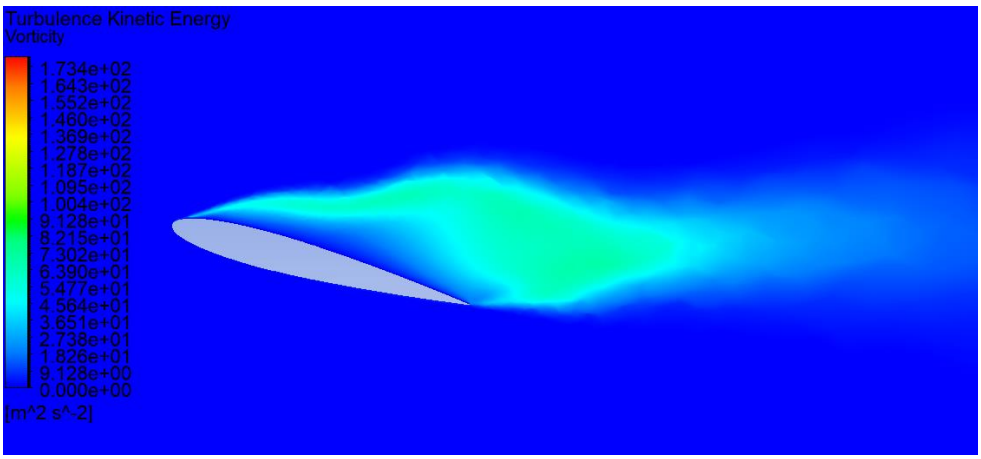

Figure 4.3.2: TKE Contour Plot for Alpha = 15°, Re = 8.0E+5

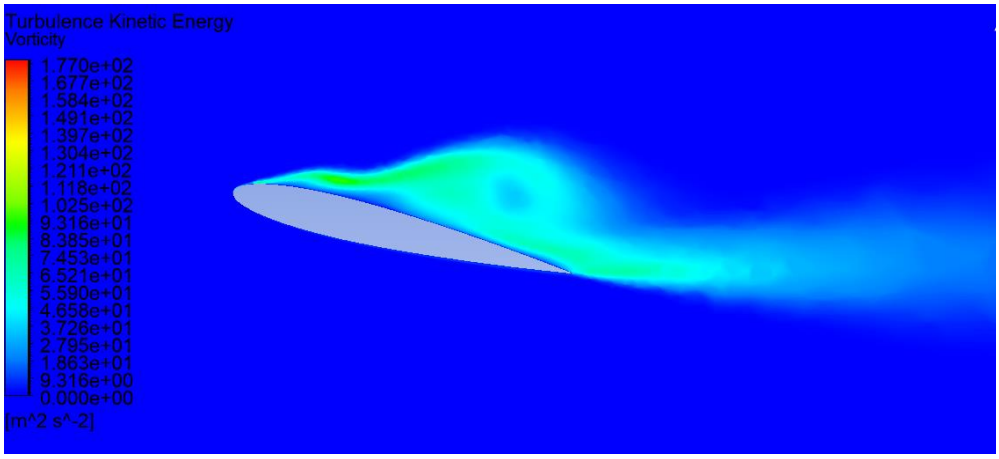

Figure 4.3.3: TKE Contour Plot for Alpha = 15°, Re = 1.0E+6

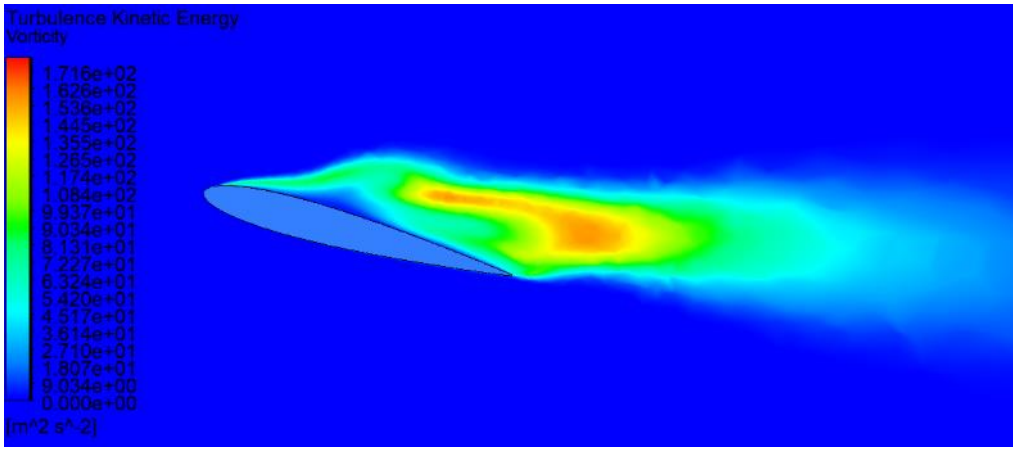

Figure 4.3.4: TKE Contour Plot for Alpha = 15°, Re = 1.2E+6

As expected, the turbulence kinetic energy around the wing is significantly higher for the higher Reynolds flow once the wing enters stall. Higher velocity and higher flow separation causes more turbulence to form around the wing. Flow separation can be observed in each TKE contour plot**,** where the vortices created by the flow separation causes turbulence away from the wing before the trailing edge. Wall shear vector plots are also taken for each simulation, which are shown below. For brevity, only the wall shear vector plots for alpha = 6° and 5° for Re = 6.0E+5 and 1.2E+6 are shown here. The remaining plots can be found in Appendix .

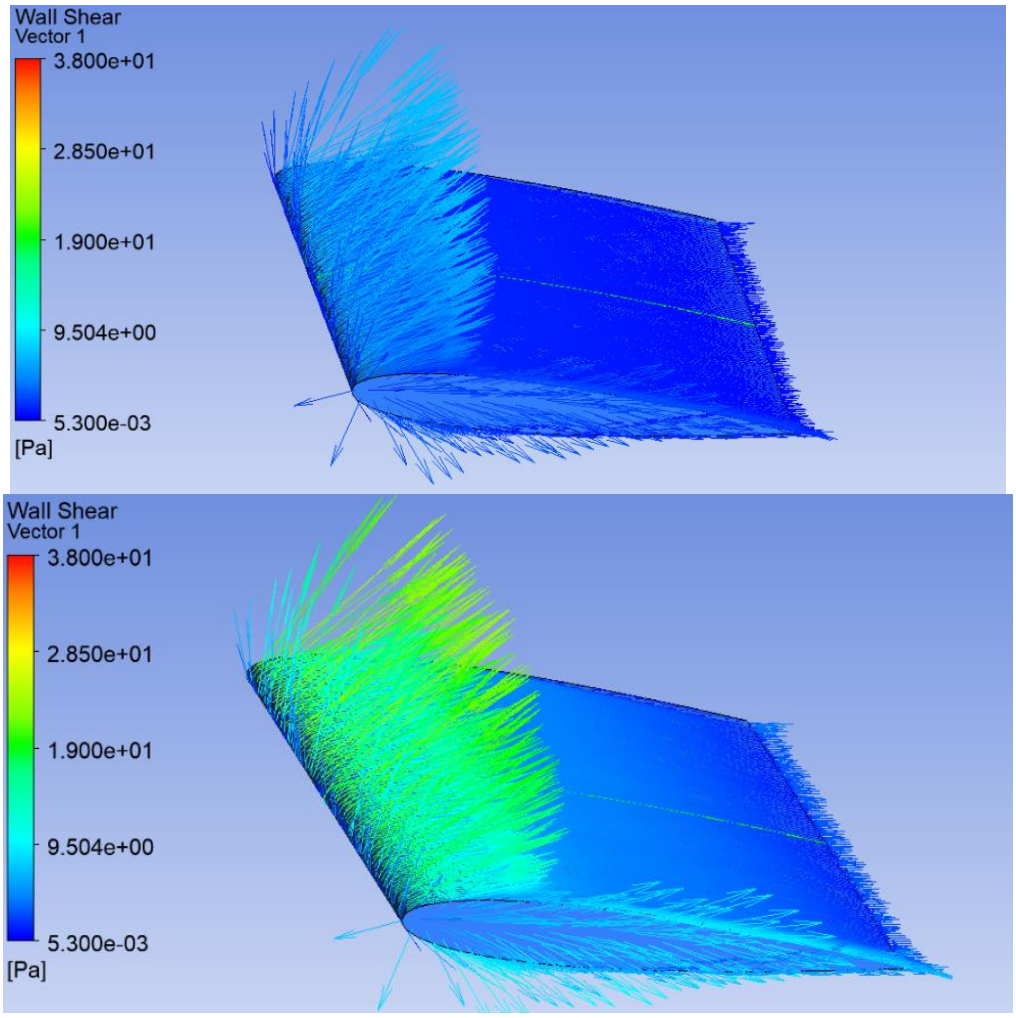

Figure 4.3.3: Wall Shear Vector Plots for Alpha = 6°; Re = 6.0E+5 (Top) & Re= 1.2E+6 (Bottom)

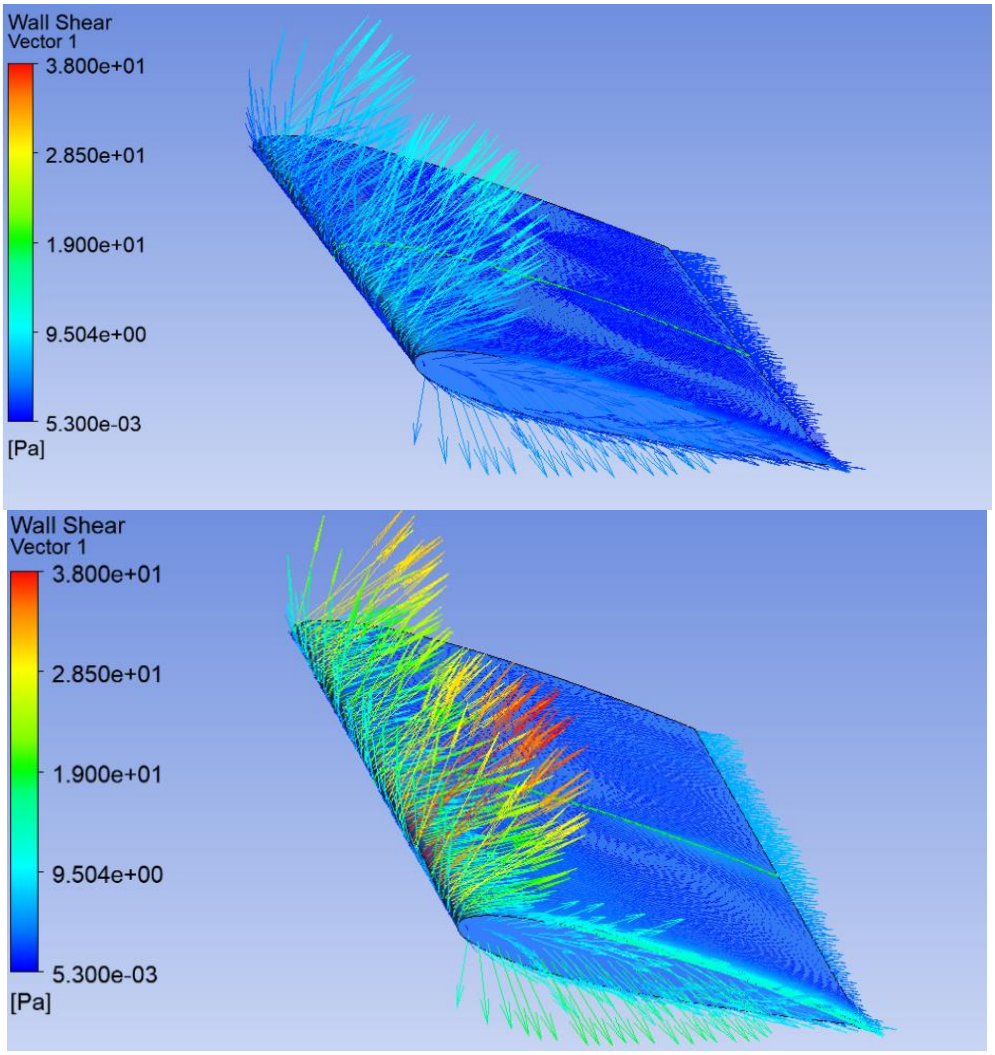

Figure 4.3.3: Wall Shear Vector Plots for Alpha = 15°; Re = 6.0E+5 (Top) & Re= 1.2E+6 (Bottom)

Similarly to the TKE contour plots, the wall shear increases as the angle of attack and flow speed increases, with most of the wall shear occurring at the leading edge, where pressure is highest. These vector plots also show the formation of vortices at the wing edge due to pressure differences between the upper and lower surfaces of the wing. These vortices occur due to the wing being of finite length, rather than a 2D airfoil. The higher and lower pressure regions mix at the wing edge, creating these vortices.

CHAPTER 5

CONCLUSION

An investigation into the effects of differing Reynolds number flow on a NACA 0012 wing near stall was conducted successfully. For each simulated flow speed, the wing exhibited behavior that it was approaching stall at an angle of attack of 12° was fully stalled at 15°. At this angle of attack, the lift coefficient drops, and the drag coefficient rises due to flow separation from the wing surface. As was expected, the pressure and velocity fields were highest for the wing at a Reynolds number of 1.2 million at an angle of attack of 15°, with the turbulence kinetic anergy and wall shear following a similar pattern. The highest amount of lift generated by the wing ($C_L = 0.849$) occurs at $\alpha = 12°$ and Re = 1.2E+6 before the wing has entered stall, while the highest amount of drag ($C_D = 0.1521$) occurs at $\alpha = 15°$ at the same flow speed. The lift-to-drag ratio decreases with an increasing angle of attack, meaning the wing is less efficient at higher angles of attack.

Since the wing that is simulated in this study is a 3D wing, the lift generated by the wing is slightly lower than what a 2D airfoil would generate due to the presence of induced vortices at the wing tip. These vortices reduce lift and increase drag; however, they are an innate symptom of a finite wing, and cannot be completely eliminated for a wing. Devices such as winglets aim to reduce the size of these vortices and move the bulk of the vortices away from the primary wing surface, but these were not tested in this study.

5.1 Future Recommendations

For future studies, it is recommended that an experimental study performed replicating the flow conditions are used to properly validate the results gathered. Since this study was done using RANS, the large amount of turbulence in the simulated flow at $\alpha = 15°$ could cause some

inaccuracies, as RANS approximates the larger eddies further away from the wing. These vortices could have an impact on the aerodynamic forces produced on the wing.

REFERENCES

Akbari, M. H., and S. J. Price. 2003. "Simulation of Dynamic Stall for a NACA 0012 Airfoil Using a Vortex Method." *Journal of Fluids and Structures* 17 (6): 855–74. https://doi.org/10.1016/S0889-9746(03)00018-5.

Anderson, J. D. 2012. "Fundamentals of Aerodynamics — Fifth Edition, J. D. Anderson, McGraw-Hill, Shoppenhangers Road, Maidenhead, Berkshire, SL6 2QL, UK. 2011. 1098pp. Illustrated. £47.99. ISBN 978-007-128908-5." *The Aeronautical Journal* 116 (1176): 222–23. https://doi.org/10.1017/S000192400000676X.

ANSYS Inc. 2011. "ANSYS FLUENT Theory Guide." 2011. https://www.afs.enea.it/project/neptunius/docs/fluent/html/th/main_pre.htm.

———. 2012. "ANSYS Mechanical APDL Element Reference." *Southpointe*. Canonsburg: ANSYS Inc.

Batther, Jagdeep, and Seongkyu Lee. 2022. "Numerical Investigation of a Pitching Airfoil Undergoing Dynamic Stall Using Delayed Detached Eddy Simulations." *Computers & Fluids* 249 (December):105691. https://doi.org/10.1016/J.COMPFLUID.2022.105691.

Bellegoni, Marco, Léo Cotteleer, Sampath Kumar Raghunathan Srikumar, Gabriele Mosca, Alessandro Gambale, Leonardo Tognotti, Chiara Galletti, and Alessandro Parente. 2023. "An Extended SST K−ω Framework for the RANS Simulation of the Neutral Atmospheric Boundary Layer." *Environmental Modelling & Software* 160 (February):105583. https://doi.org/10.1016/J.ENVSOFT.2022.105583.

Carr, Lawrence W. 1988. "Progress in Analysis and Prediction of Dynamic Stall." *Journal of Aircraft* 25 (1): 6–17. https://doi.org/10.2514/3.45534.

Casey, John P. 2004. “Effect of Dimple Pattern on the Suppression of Boundary Layer Separation on a Low Pressure Turbine Blade.” https://scholar.afit.edu/etd/3923/.

Cavagna, Luca, Giuseppe Quaranta, and Paolo Mantegazza. 2007. “Application of Navier–Stokes Simulations for Aeroelastic Stability Assessment in Transonic Regime.” *Computers & Structures* 85 (11–14): 818–32. https://doi.org/10.1016/J.COMPSTRUC.2007.01.005.

Chang, Jianlong, Qingui Zhang, Liujing He, and Yi Zhou. 2022. “Shedding Vortex Characteristics Analysis of NACA 0012 Airfoil at Low Reynolds Numbers.” *Energy Reports* 8 (July):156–74. https://doi.org/10.1016/J.EGYR.2022.01.149.

Chen, Zhen, Zhiwei Shi, Sinuo Chen, and Zhangyi Yao. 2022. “Stall Flutter Suppression of NACA 0012 Airfoil Based on Steady Blowing.” *Journal of Fluids and Structures* 109 (February):103472. https://doi.org/10.1016/J.JFLUIDSTRUCTS.2021.103472.

CHENG, Zepeng, Shiyan ZHANG, Yang XIANG, Chun SHAO, Miao ZHANG, Hong LIU, and Yingchun CHEN. 2022. “Effect of Vortex Dynamics and Instability Characteristics on the Induced Drag of Trailing Vortices.” *Chinese Journal of Aeronautics* 35 (9): 160–73. https://doi.org/10.1016/J.CJA.2021.12.012.

F. R. Menter. 1993. “Zonal Two Equation K-w Turbulence Models For Aerodynamic Flows.” *American Institute of Aeronautics and Astronautics*, 93–2906.

———. 1994. “Two-Equation Eddy-Viscosity Turbulence Models for Engineering Applications.” *AIAA* 32 (8): 1598–1605.

Ferziger, Joel H., and Milovan Perić. 2002. “Computational Methods for Fluid Dynamics.” *Computational Methods for Fluid Dynamics*. https://doi.org/10.1007/978-3-642-56026-2.

Friedlander, S. 2004. “Stability of Flows.” *Encyclopedia of Mathematical Physics: Five-Volume Set*, January, 1–7. https://doi.org/10.1016/B0-12-512666-2/00252-2.

Han, Le, Dasheng Wei, Yanrong Wang, and Xiaojie Zhang. 2021. "Vortex-Induced Vibration Mechanism of the NACA 0012 Airfoil Based on a Method of Separating Disturbances." *Journal of Sound and Vibration* 501 (June):116044. https://doi.org/10.1016/J.JSV.2021.116044.

Ilie, Marcel. 2019a. "A Fully-Coupled CFD/CSD Computational Approach for Aeroelastic Studies of Helicopter Blade-Vortex Interaction." *Applied Mathematics and Computation* 347 (April):122–42. https://doi.org/10.1016/J.AMC.2018.10.069.

———. 2019b. "Fluid-Structure Interaction in Turbulent Flows; a CFD Based Aeroelastic Algorithm Using LES." *Applied Mathematics and Computation* 342 (February):309–21. https://doi.org/10.1016/J.AMC.2017.10.059.

Karki, K. C., and S. V. Patankar. 2012. "Pressure Based Calculation Procedure for Viscous Flows at All Speedsin Arbitrary Configurations." *Https://Doi.Org/10.2514/3.10242* 27 (9): 1167–74. https://doi.org/10.2514/3.10242.

Komen, E. M.J., J. A. Hopman, E. M.A. Frederix, F. X. Trias, and R. W.C.P. Verstappen. 2021. "A Symmetry-Preserving Second-Order Time-Accurate PISO-Based Method." *Computers & Fluids* 225 (July):104979. https://doi.org/10.1016/J.COMPFLUID.2021.104979.

Mahato, Arunabha, Ravi Kant Singh, Rahul Barnwal, and Subhas Chandra Rana. 2023. "Aerodynamic Characteristics of NACA 0012 vs. NACA 4418 Airfoil for Wind Turbine Applications through CFD Simulation." *Materials Today: Proceedings*, May. https://doi.org/10.1016/J.MATPR.2023.05.439.

Mccroskey, W J. 1981. "The Phenomenon of Dynamic Stall." https://ntrs.nasa.gov/api/citations/19810011501/downloads/19810011501.pdf.

McCroskey, W. J., L. W. Carr, and K. W. McAlister. 2012. “Dynamic Stall Experiments on Oscillating Airfoils.” *Https://Doi.Org/10.2514/3.61332* 14 (1): 57–63. https://doi.org/10.2514/3.61332.

McCroskey, WJ, KW McAlister, … LW Carr - Journal of the, and undefined 1981. n.d. “Dynamic Stall on Advanced Airfoil Sections.” *Ingentaconnect.Com*. Accessed October 7, 2022. https://www.ingentaconnect.com/content/ahs/jahs/1981/00000026/00000003/art00006.

Patankar, S. V., and D. B. Spalding. 1972. “A Calculation Procedure for Heat, Mass and Momentum Transfer in Three-Dimensional Parabolic Flows.” *International Journal of Heat and Mass Transfer* 15 (10): 1787–1806. https://doi.org/10.1016/0017-9310(72)90054-3.

Pries, Michael, Andreas Fiolitakis, and Peter Gerlinger. 2024. “An Implicit Splitting Scheme with Characteristic Boundary Conditions for Compressible Reactive Flows on Unstructured Grids.” *Journal of Computational and Applied Mathematics* 437 (February):115446. https://doi.org/10.1016/J.CAM.2023.115446.

Rahman, M. M. 2021. “Compromising with Corrector Step of SIMPLE Algorithm.” *Mathematics and Computers in Simulation* 188 (October):135–63. https://doi.org/10.1016/J.MATCOM.2021.03.043.

———. 2023. “Predicting Transition with Wall-Distance-Free SST k-ω Model.” *Computers & Fluids* 250 (January):105704. https://doi.org/10.1016/J.COMPFLUID.2022.105704.

Rouser, Kurt P. 2002. “Use of Dimples to Suppress Boundary Layer Separation on a Low Pressure Turbine Blade.” https://scholar.afit.edu/etd/4139/.

Schetz, Joseph A., and Rodney D. W. Bowersox. 2011. “Boundary Layer Analysis, Second Edition.” *Boundary Layer Analysis, Second Edition*, August. https://doi.org/10.2514/4.868245.

sciences, JC Lin - Progress in aerospace, and undefined 2002. 2002. “Review of Research on Low-Profile Vortex Generators to Control Boundary-Layer Separation.” *Elsevier* 38:389–420. https://www.sciencedirect.com/science/article/pii/S0376042102000106.

Sohail, Muhammad Amjad, and Rizwan Ullah. 2017. “CFD of Oscillating Airfoil Pitch Cycle by Using PISO Algorithm Keywords-Angle of Attack, Centre of Pressure, Subsonic Flow, Pitching Moment Coefficient, Turbulence Mode.” https://www.researchgate.net/publication/319650482.

Srinivasa Rao, Talluri, Trilochan Mahapatra, and Sai Chaitanya Mangavelli. 2018. “Enhancement of Lift-Drag Characteristics of NACA 0012.” *Materials Today: Proceedings* 5 (2): 5328–37. https://doi.org/10.1016/J.MATPR.2017.12.117.

Tao, Jun, Xinyu Wang, and Gang Sun. 2021. “Stall Characteristics Analyses and Stall Lift Robustness Inverse Design for High-Lift Devices of a Wide-Body Commercial Aircraft.” *Aerospace Science and Technology* 111 (April):106570. https://doi.org/10.1016/J.AST.2021.106570.

Troldborg, Niels, Niels N. Sørensen, and Frederik Zahle. 2022. “Immersed Boundary Method for the Incompressible Reynolds Averaged Navier–Stokes Equations.” *Computers & Fluids* 237 (April):105340. https://doi.org/10.1016/J.COMPFLUID.2022.105340.

Tsuchiya, Takaaki, Daiju Numata, Tetsuya Suwa, and Keisuke Asai. 2013. “Influence of Turbulence Intensity on Aerodynamic Characteristics of an NACA 0012 at Low Reynolds Numbers.” *51st AIAA Aerospace Sciences Meeting Including the New Horizons Forum and Aerospace Exposition 2013*. https://doi.org/10.2514/6.2013-65.

UIUC Applied Aerodynamics Group. 2023. “UIUC Airfoil Coordinates Database.” 2023. https://m-selig.ae.illinois.edu/ads/coord_database.html.

White, Frank M. 2002. *Fluid Mechanics*. 5th ed. McGraw Hill.

Wilcox, David C. 2001. “Turbulence Modeling: An Overview.” *39th Aerospace Sciences Meeting and Exhibit*. https://doi.org/10.2514/6.2001-724.

Wu, You, Yuting Dai, and Chao Yang. 2022. “Time-Delayed Active Control of Stall Flutter for an Airfoil via Camber Morphing.” *AIAA Journal* 60 (10): 5723–34. https://doi.org/10.2514/1.J061947.

ZHANG, Yufei, Chongyang YAN, Haixin CHEN, and Yuhui YIN. 2020. “Study of Riblet Drag Reduction for an Infinite Span Wing with Different Sweep Angles.” *Chinese Journal of Aeronautics* 33 (12): 3125–37. https://doi.org/10.1016/J.CJA.2020.05.015.

APPENDIX

Appendix A Pressure and Velocity Contours

Below are the pressure contour plots gathered for Re = 600k for α = 6°, 9°, 12°, and 15° respectively

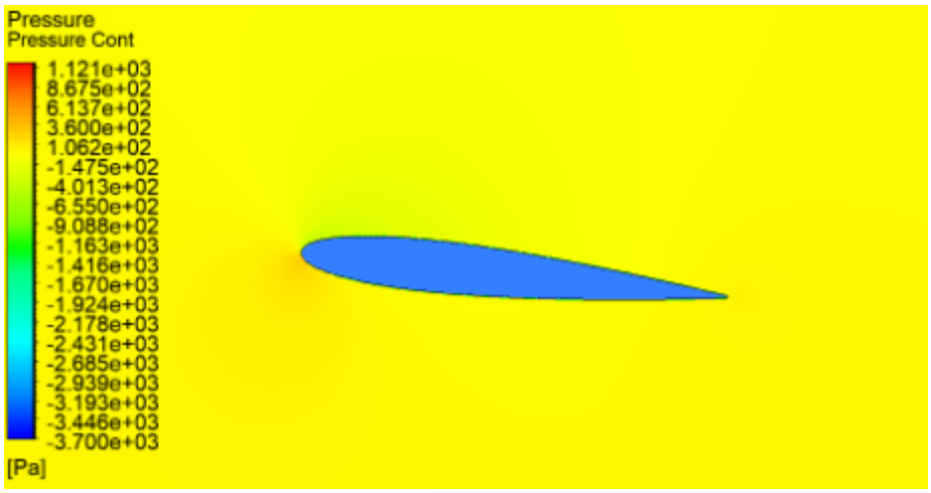

Figure A.1: Pressure Contour at Re = 6.0E5; α = 6°

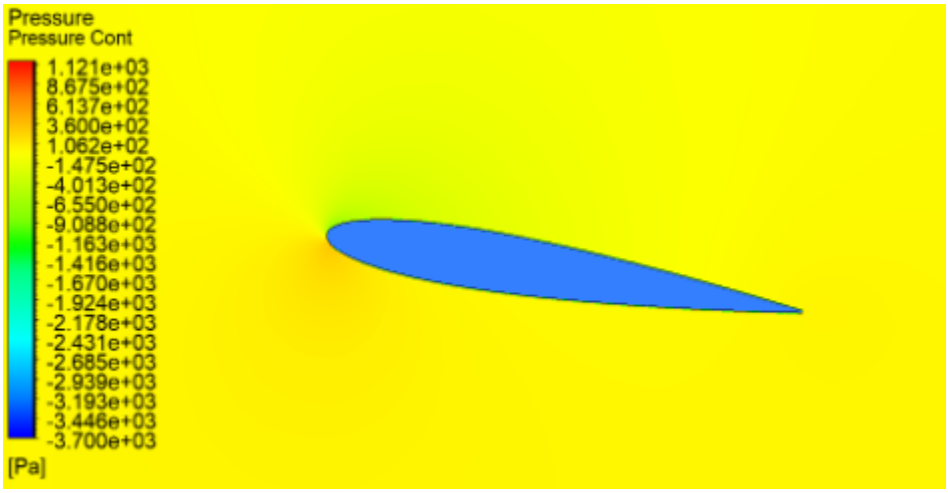

Figure A.2: Pressure Contour at Re = 6.0E5; α = 9°

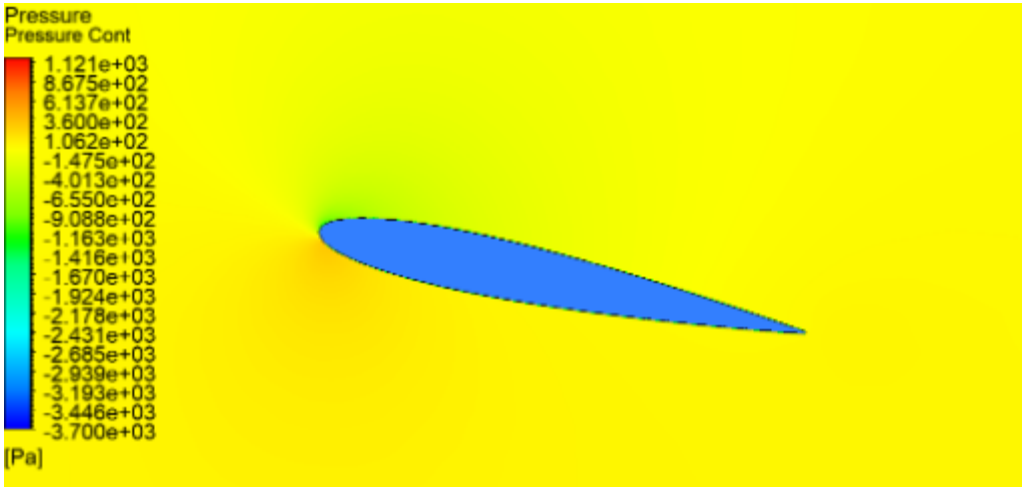

Figure A.3: Pressure Contour at Re = 6.0E5; α = 12°

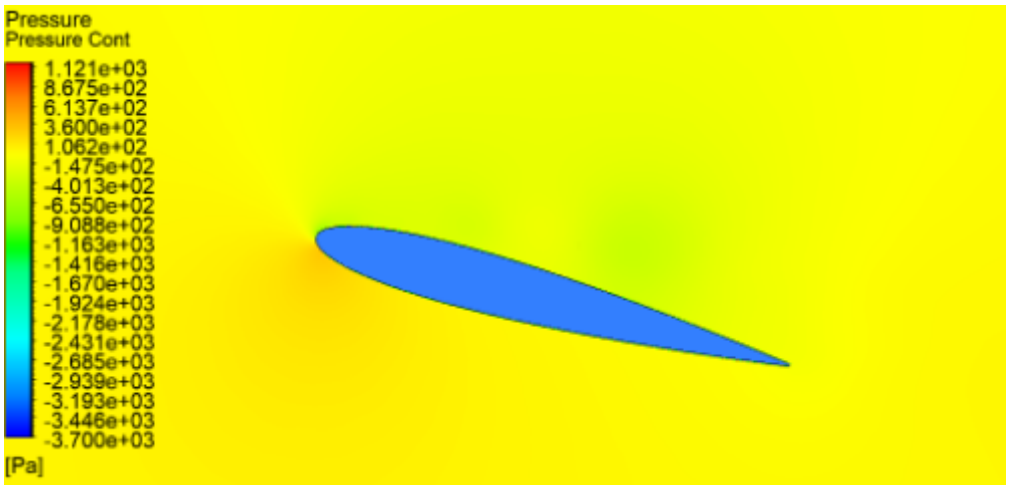

Figure A.4: Pressure Contour at Re = 6.0E5; α = 15°

Below are the pressure contour plots gathered for Re = 800k for α = 6°, 9°, 12°, and 15° respectively

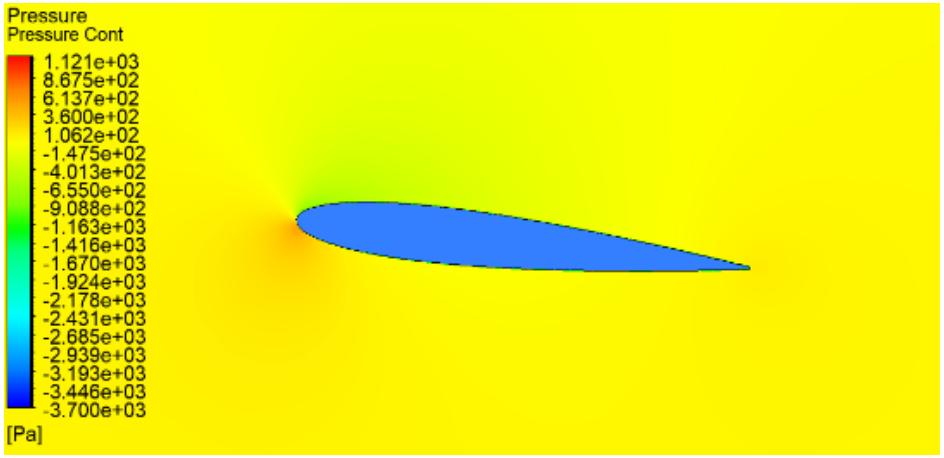

Figure A.5: Pressure Contour at Re = 8.0E5; α = 6°

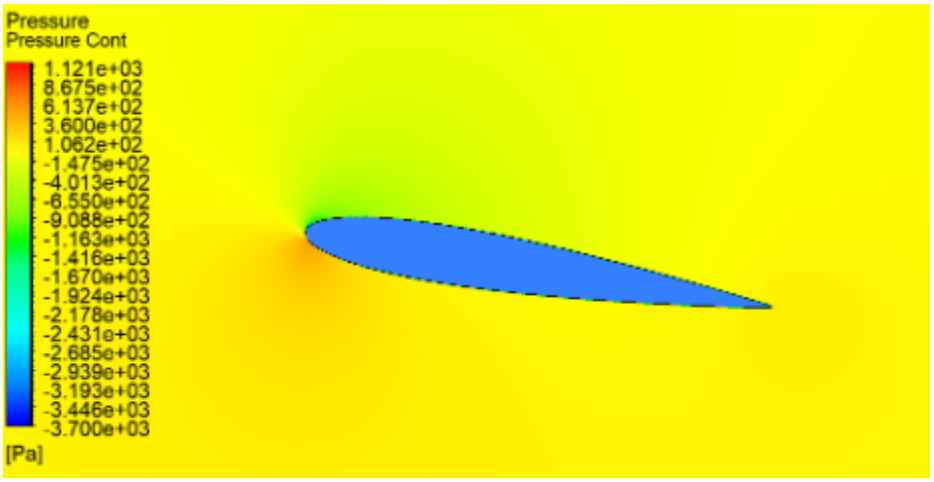

Figure A.6: Pressure Contour at Re = 8.0E5; α = 9°

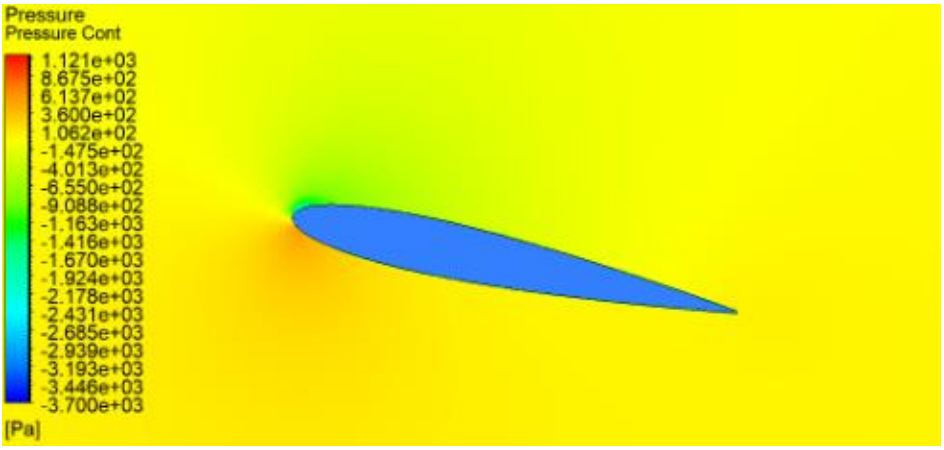

Figure A.7: Pressure Contour at Re = 8.0E5; α = 12°

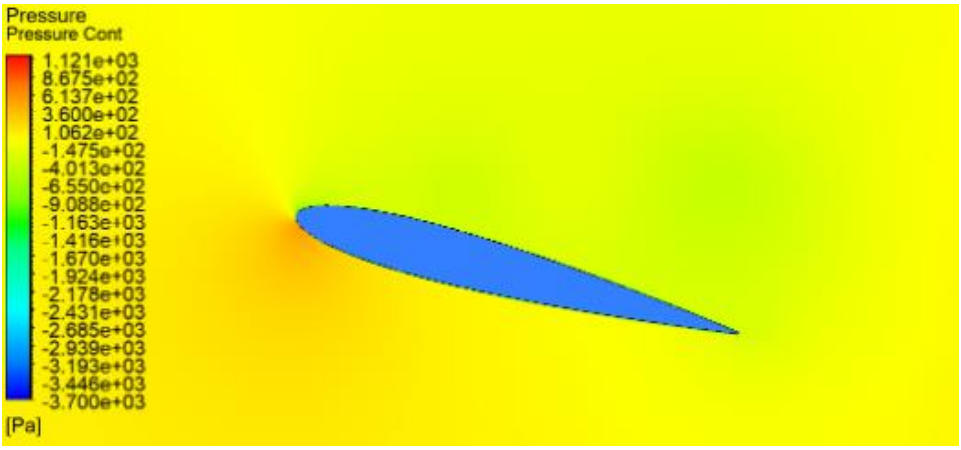

Figure A.7: Pressure Contour at Re = 8.0E5; α = 15°

Below are the pressure contour plots gathered for Re = 1 mil for α = 6°, 9°, 12°, and 15° respectively

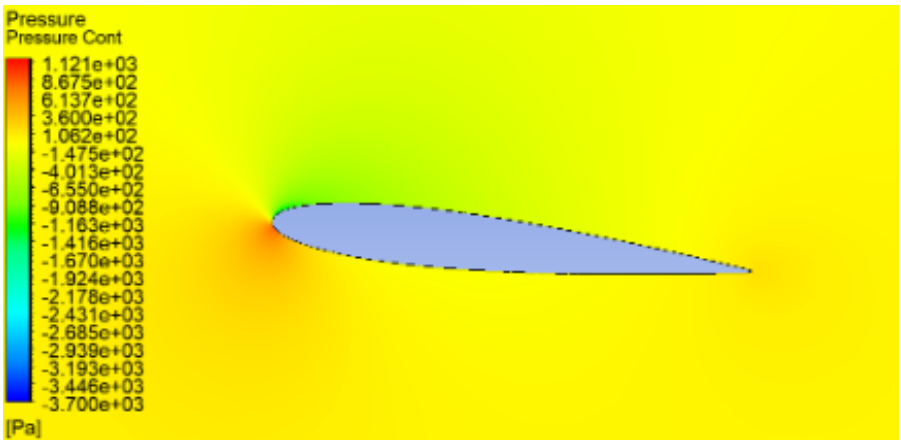

Figure A.8: Pressure Contour at Re = 1.0E6; α = 6°

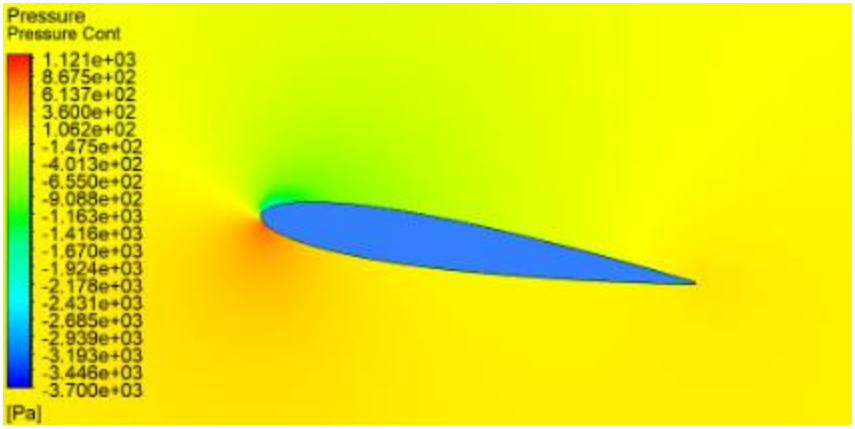

Figure A.9: Pressure Contour at Re = 1.0E6; α = 9°

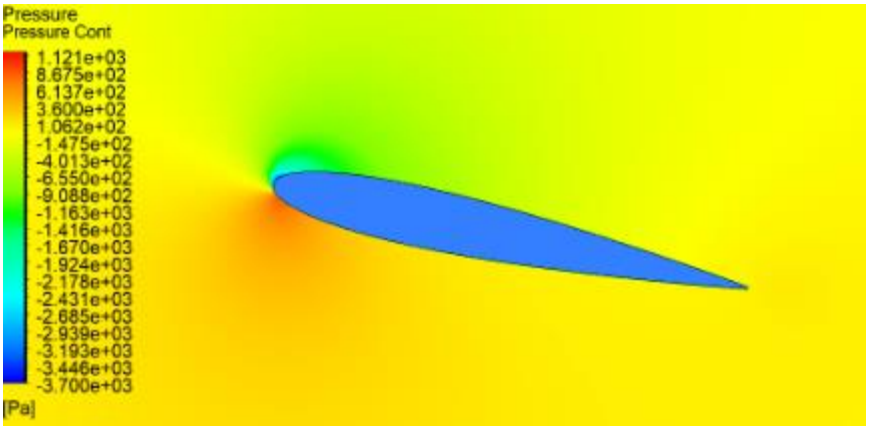

Figure A.10: Pressure Contour at Re = 1.0E6; α = 12°

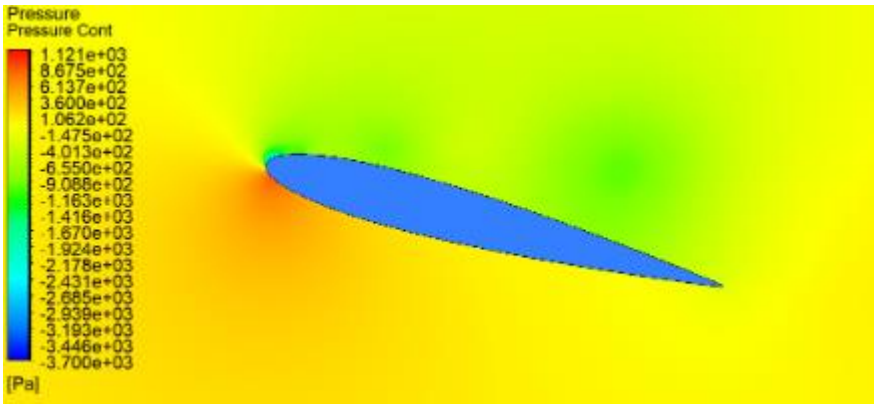

Figure A.11: Pressure Contour at Re = 1.0E6; α = 15°

Below are the pressure contour plots gathered for Re = 1.2 mil for α = 6°, 9°, 12°, and 15° respectively

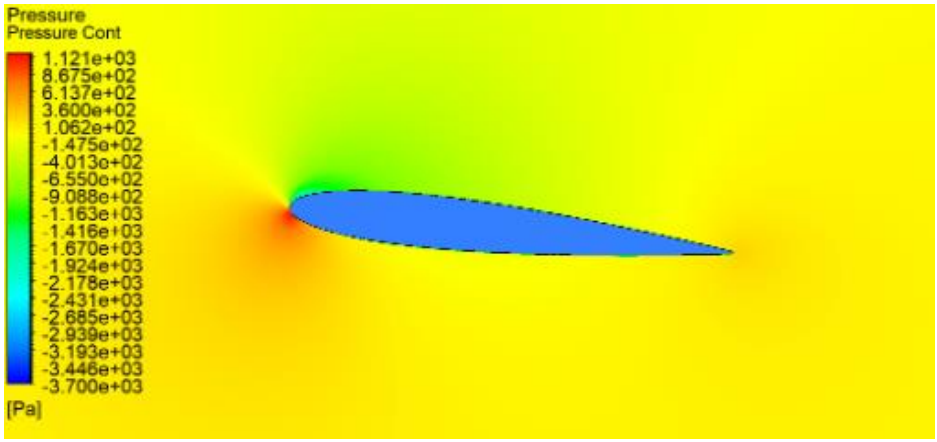

Figure A.12: Pressure Contour at Re = 1.2E6; α = 6°

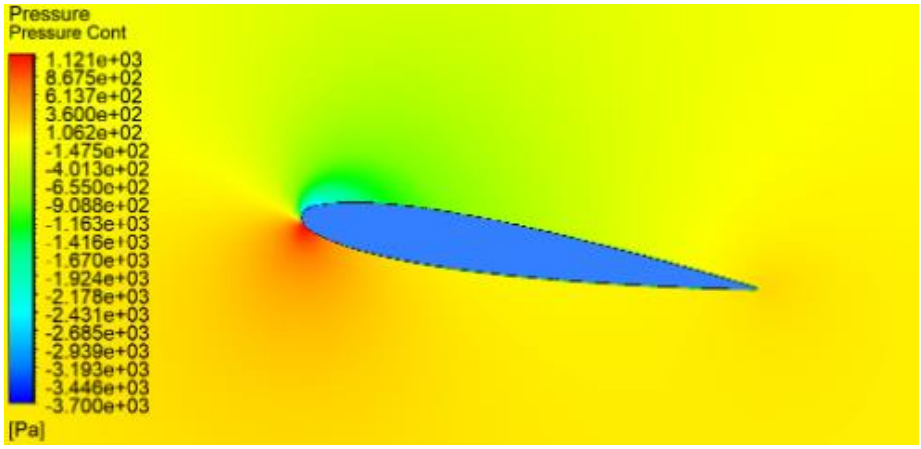

Figure A.13: Pressure Contour at Re = 1.2E6; α = 9°

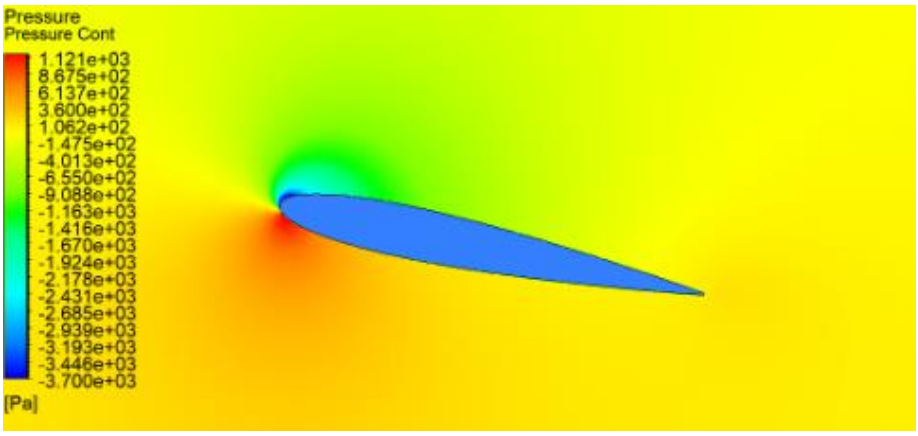

Figure A.14: Pressure Contour at Re = 1.2E6; α = 12°

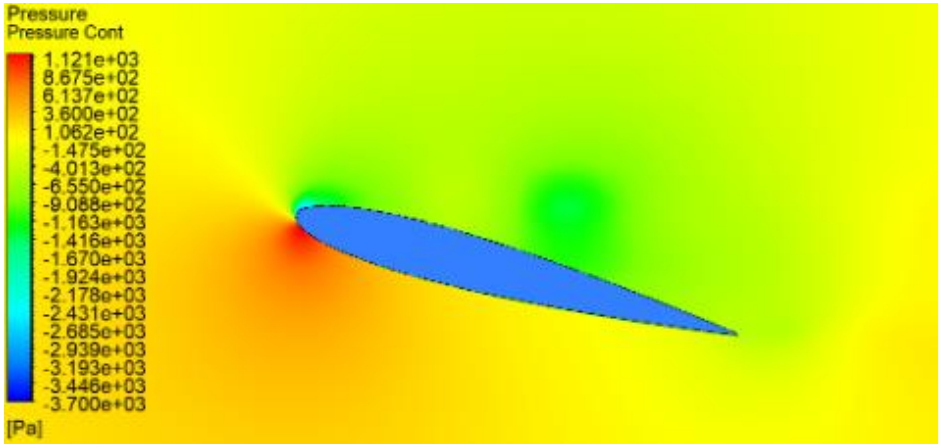

Figure A.15: Pressure Contour at Re = 1.2E6; α = 15°

Below are the velocity contour plots gathered for Re = 600k for α = 6°, 9°, 12°, and 15° respectively

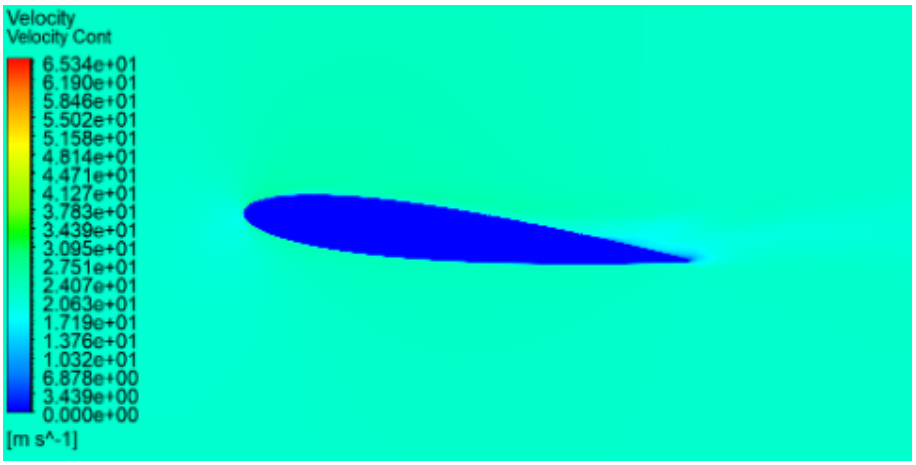

Figure A.16: Velocity Contour at Re = 6.0E5; α = 6°

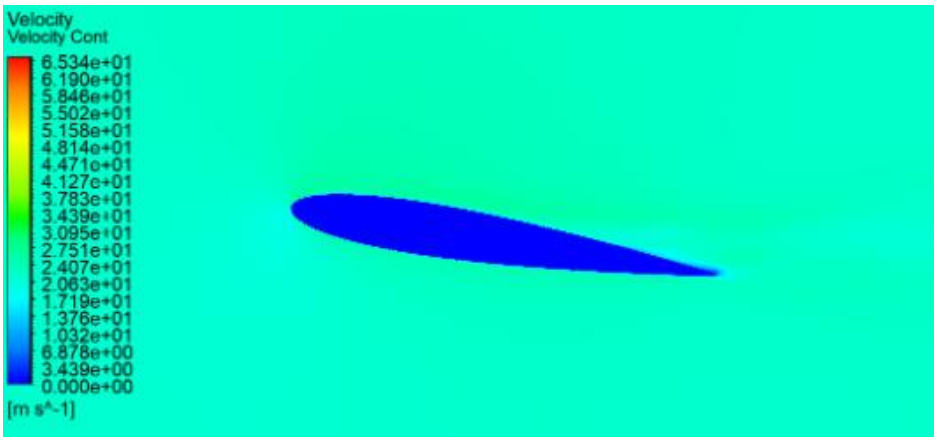

Figure A.17: Velocity Contour at Re = 6.0E5; α = 9°

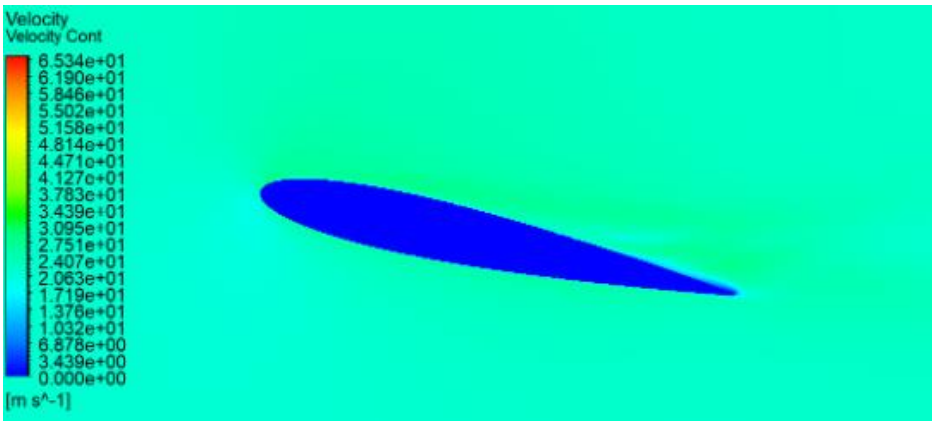

Figure A.18: Velocity Contour at Re = 6.0E5; α = 12°

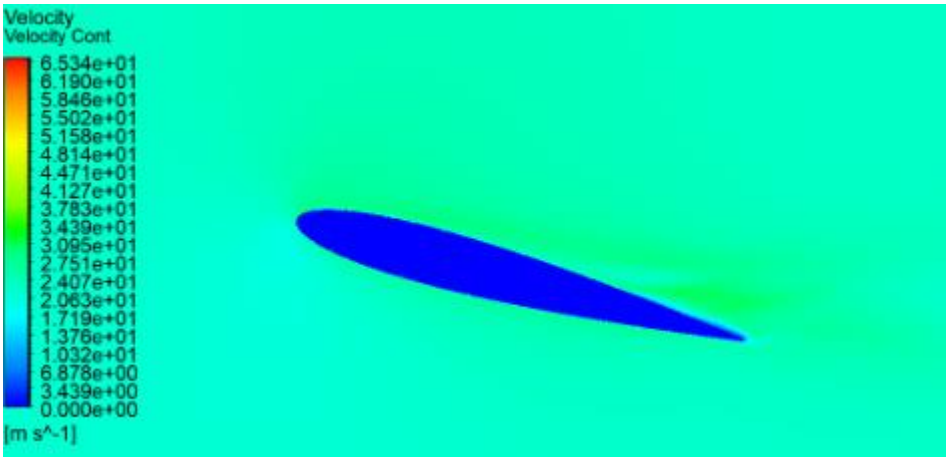

Figure A.19: Velocity Contour at Re = 6.0E5; α = 15°

Below are the velocity contour plots gathered for Re = 800k for α = 6°, 9°, 12°, and 15° respectively

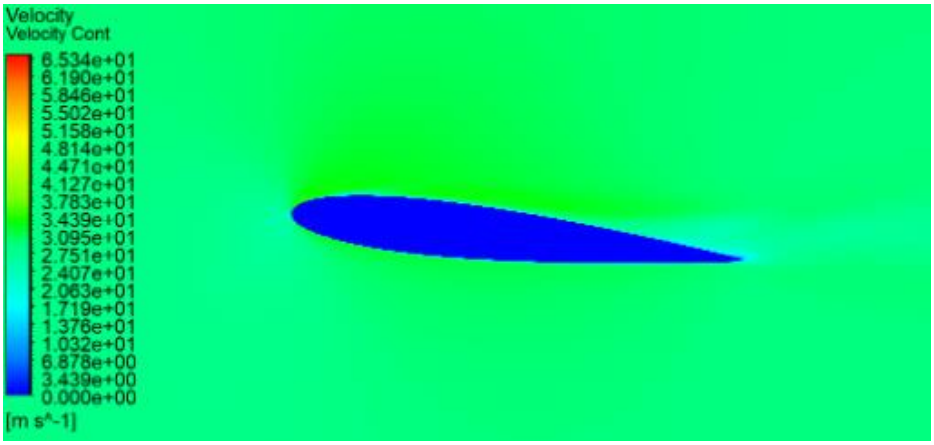

Figure A.20: Velocity Contour at Re = 8.0E5; α = 6°

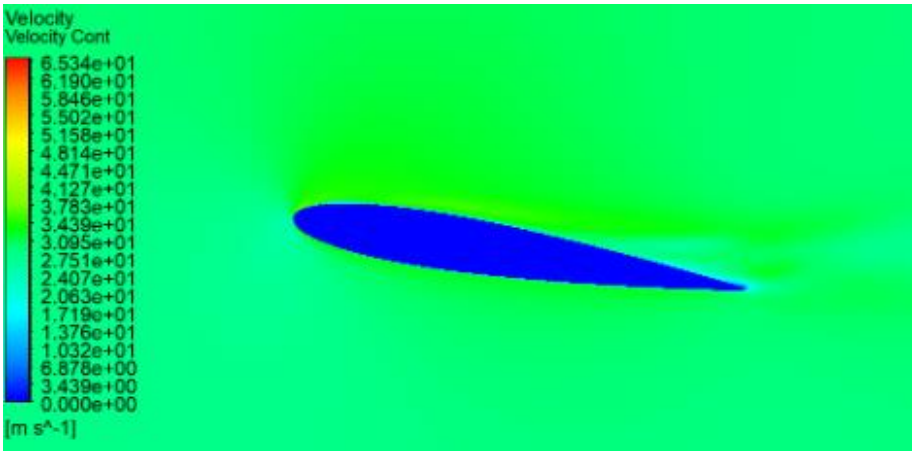

Figure A.21: Velocity Contour at Re = 8.0E5; α = 9°

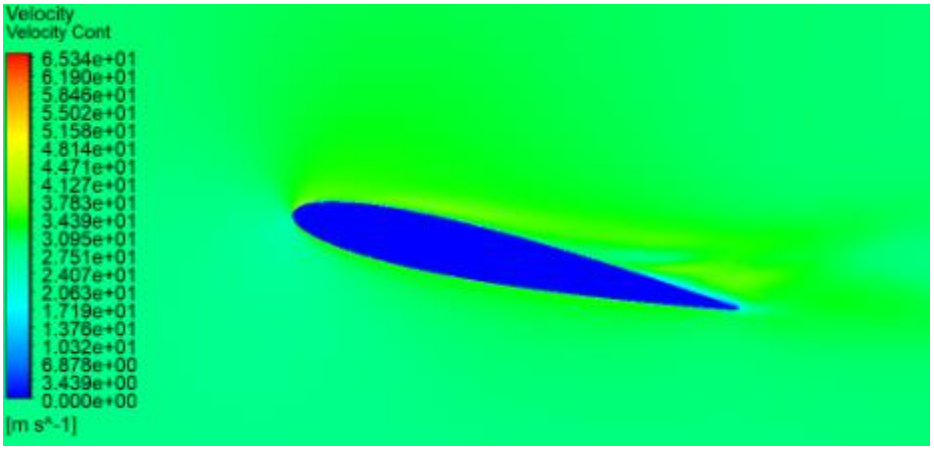

Figure A.22: Velocity Contour at Re = 8.0E5; α = 12°

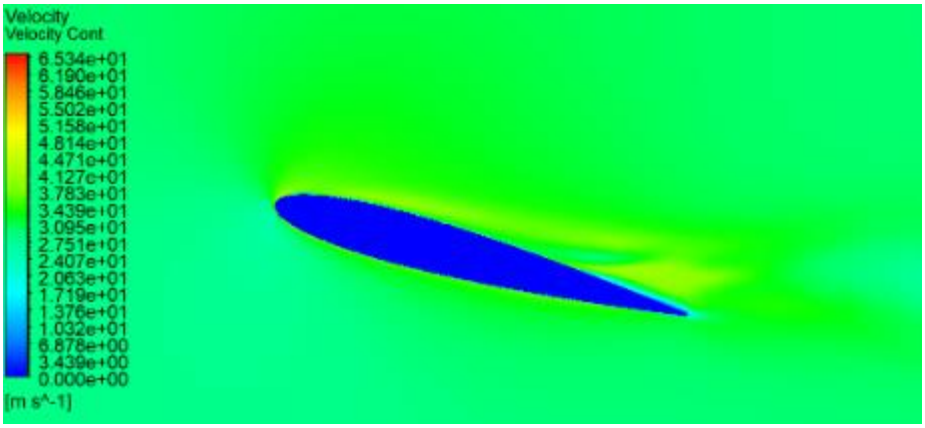

Figure A.21: Velocity Contour at Re = 8.0E5; α = 15°

Below are the velocity contour plots gathered for Re = 1 mil for α = 6°, 9°, 12°, and 15° respectively

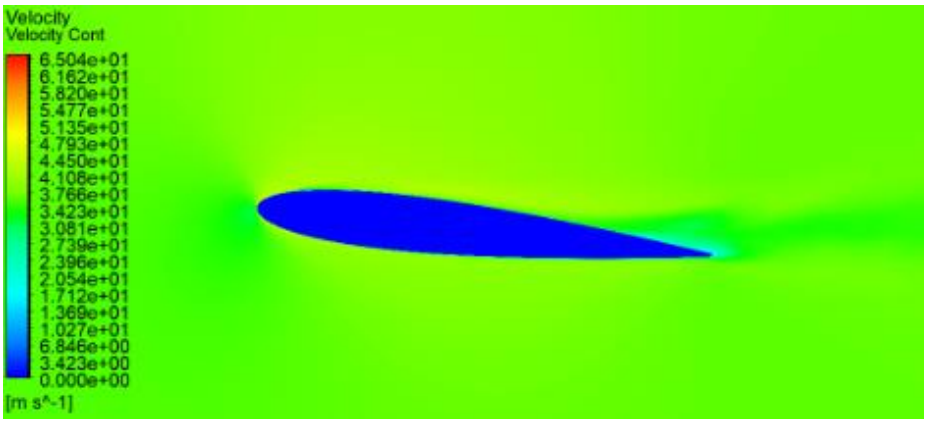

Figure A.22: Velocity Contour at Re = 1.0E6; α = 6°

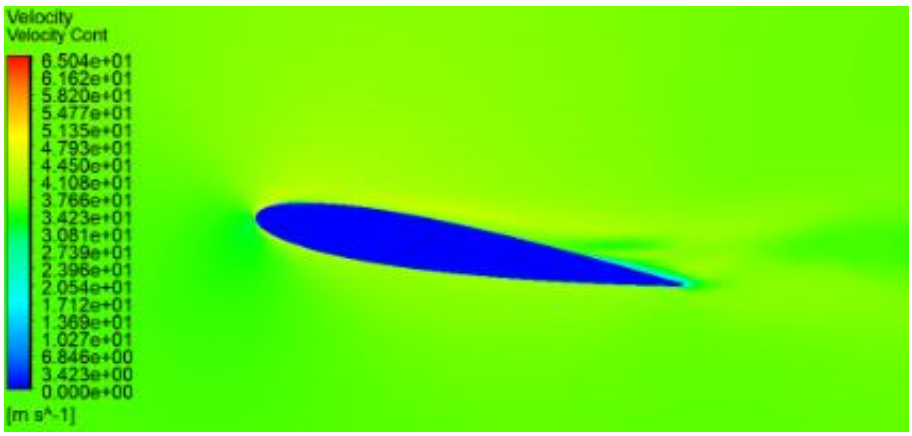

Figure A.23: Velocity Contour at Re = 1.0E6; α = 9°

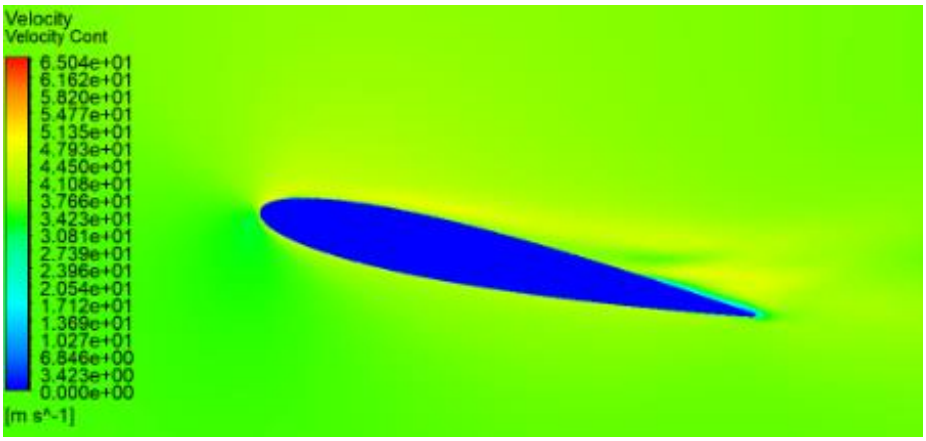

Figure A.24: Velocity Contour at Re = 1.0E6; α = 12°

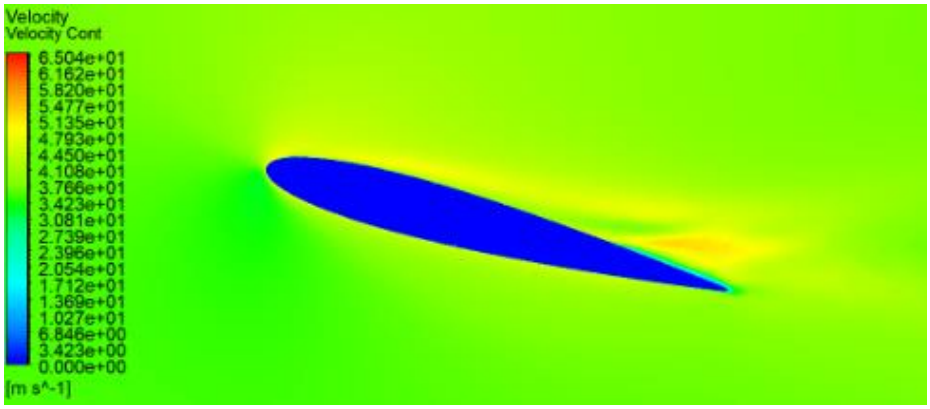

Figure A.25: Velocity Contour at Re = 1.0E6; α = 15°

Below are the velocity contour plots gathered for Re = 1.2 mil for α = 6°, 9°, 12°, and 15° respectively

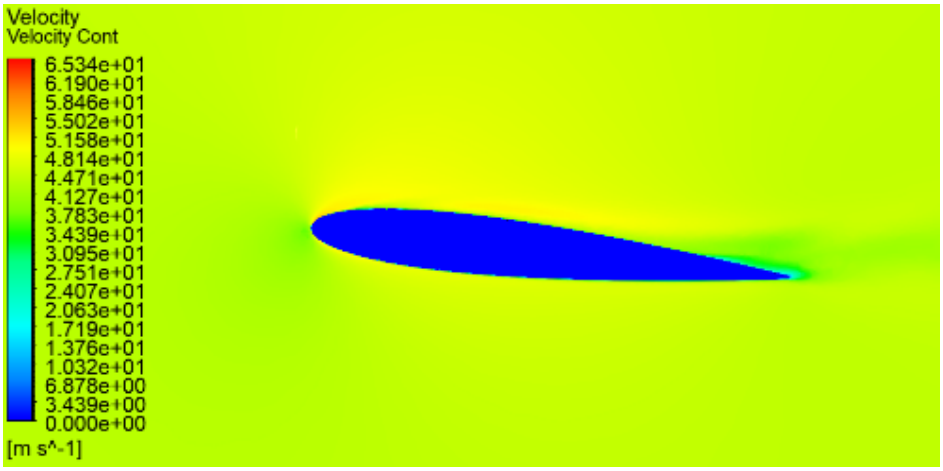

Figure A.26: Velocity Contour at Re = 1.2E6; α = 6°

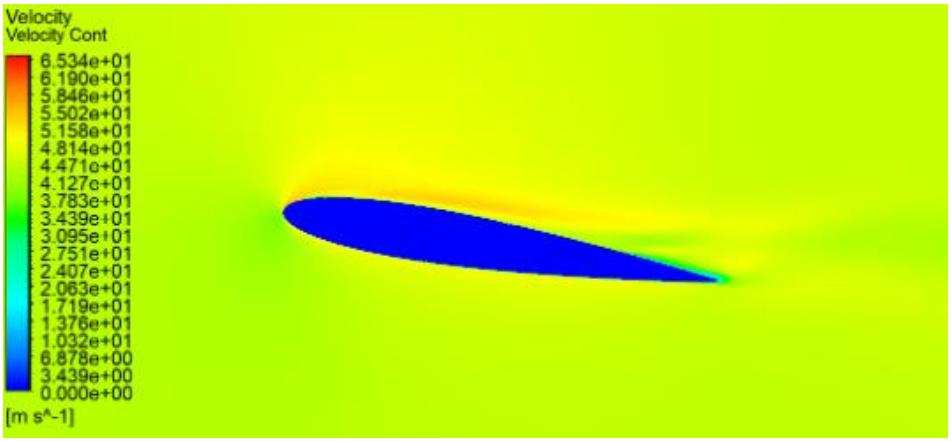

Figure A.27: Velocity Contour at Re = 1.2E6; α = 9°

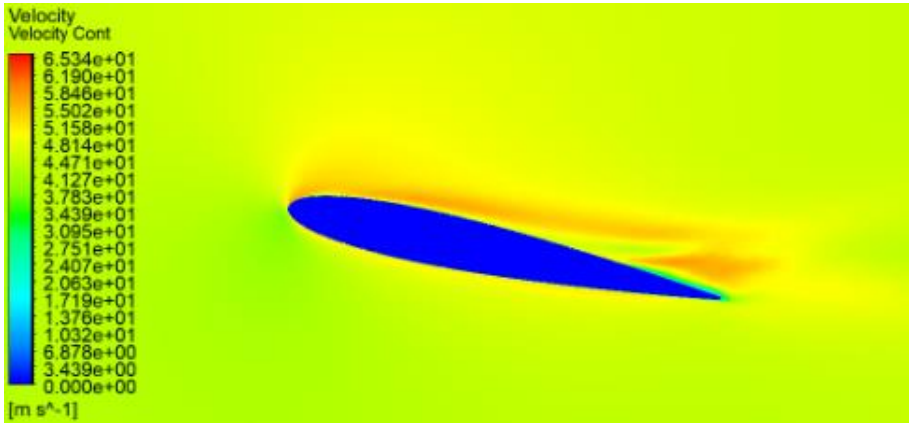

Figure A.28: Velocity Contour at Re = 1.2E6; α = 12°

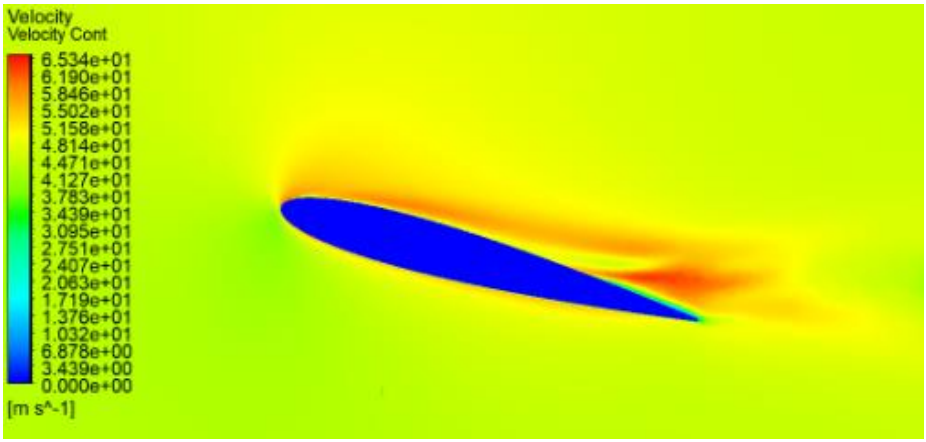

Figure A.29: Velocity Contour at Re = 1.2E6; α = 15°

Appendix B Wall Shear Vector and Turbulence Kinetic Energy Plots

Below are the wall shear vector plots gathered for Re = 600k for α = 6°, 9°, 12°, and 15° respectively

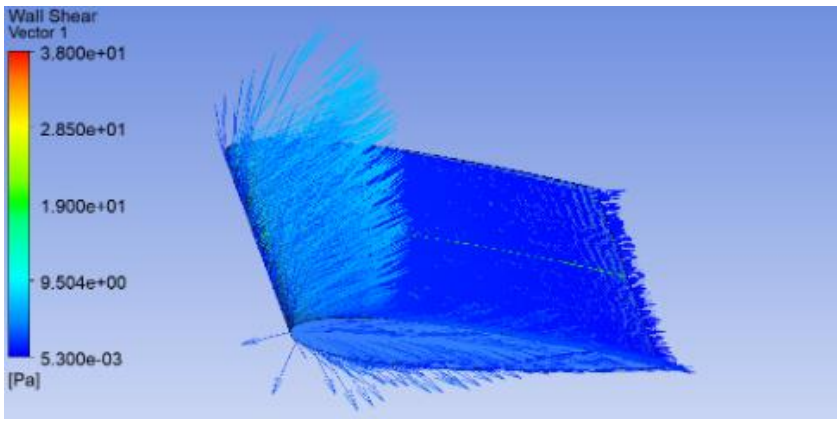

Figure B.1: Wall Shear Vector Plot for Re = 6.0E5; α = 6°

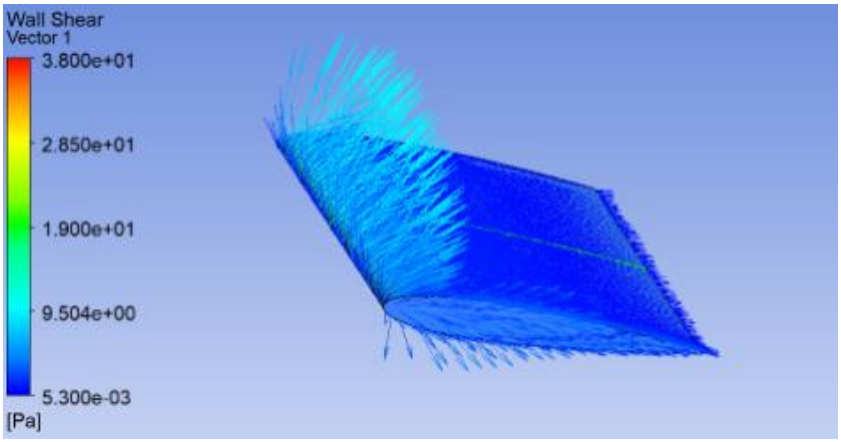

Figure B.2: Wall Shear Vector Plot for Re = 6.0E5; α = 9°

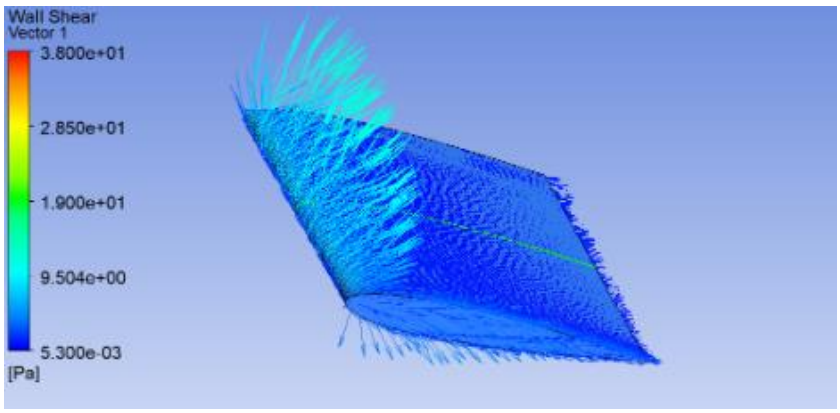

Figure B.3: Wall Shear Vector Plot for Re = 6.0E5; α = 12°

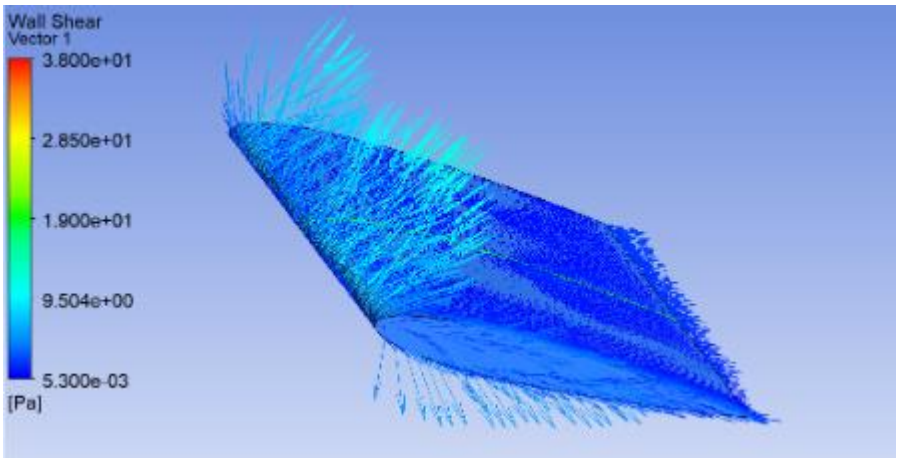

Figure B.4: Wall Shear Vector Plot for Re = 6.0E5; α = 15°

Below are the wall shear vector plots gathered for Re = 800k for α = 6°, 9°, 12°, and 15° respectively

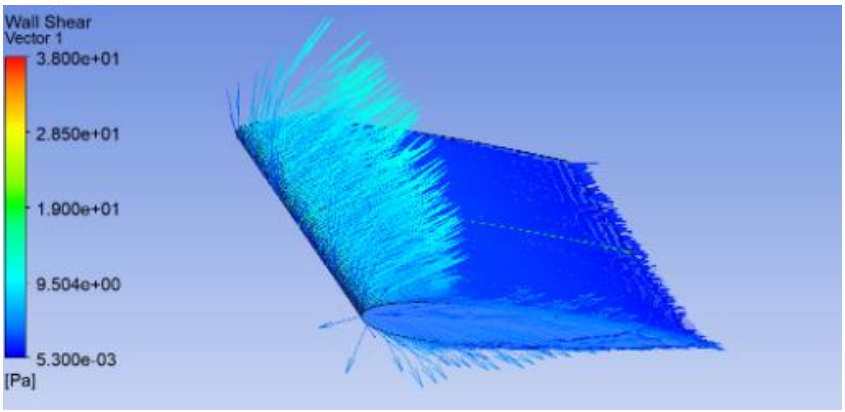

Figure B.5: Wall Shear Vector Plot for Re = 8.0E5; α = 6°

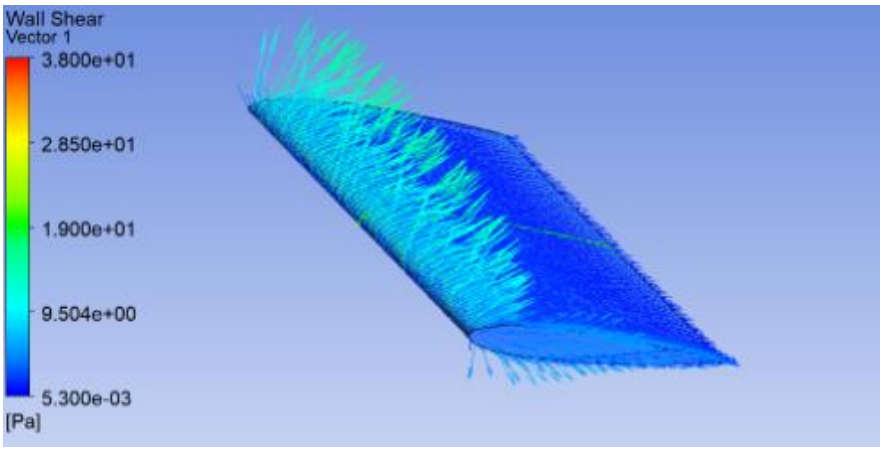

Figure B.6: Wall Shear Vector Plot for Re = 8.0E5; α = 9°

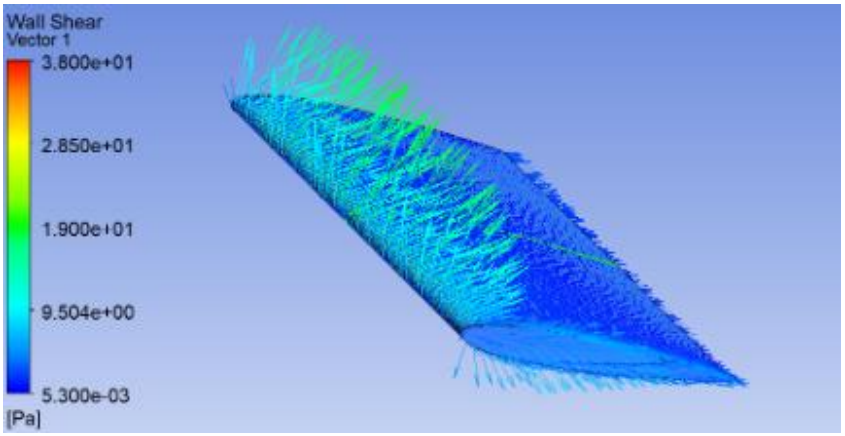

Figure B.7: Wall Shear Vector Plot for Re = 8.0E5; α = 12°

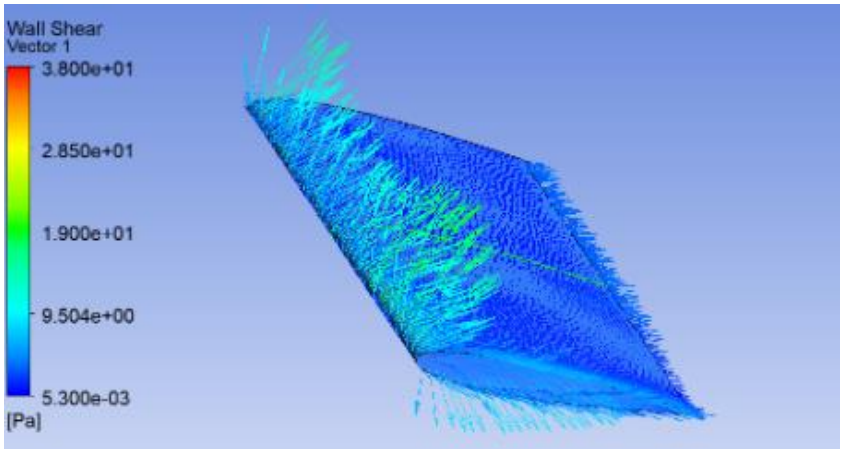

Figure B.8: Wall Shear Vector Plot for Re = 8.0E5; α = 15°

Below are the wall shear vector plots gathered for Re = 1 mil for α = 6°, 9°, 12°, and 15° respectively

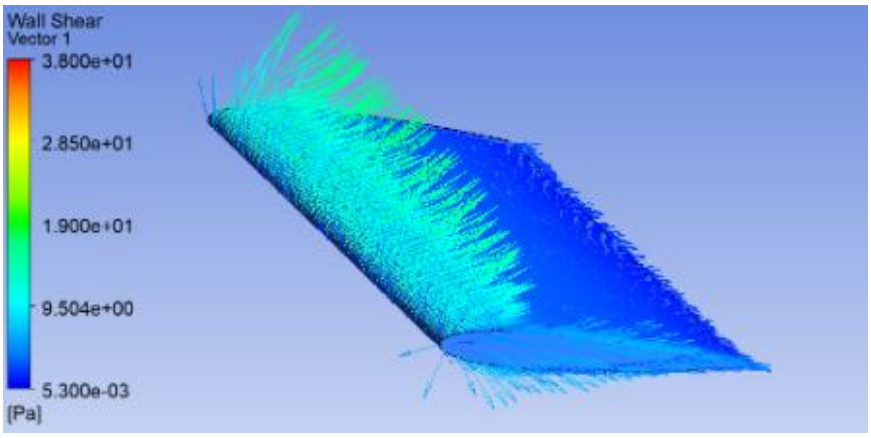

Figure B.9: Wall Shear Vector Plot for Re = 1.0E6; α = 6°

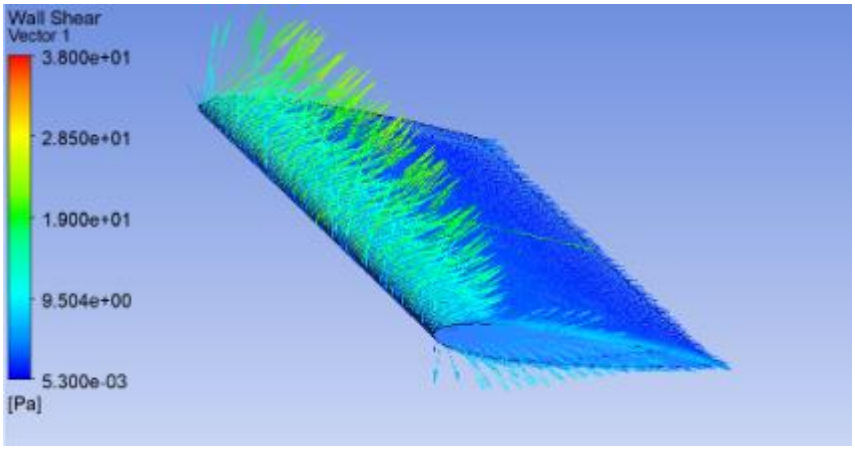

Figure B.10: Wall Shear Vector Plot for Re = 1.0E6; α = 9°

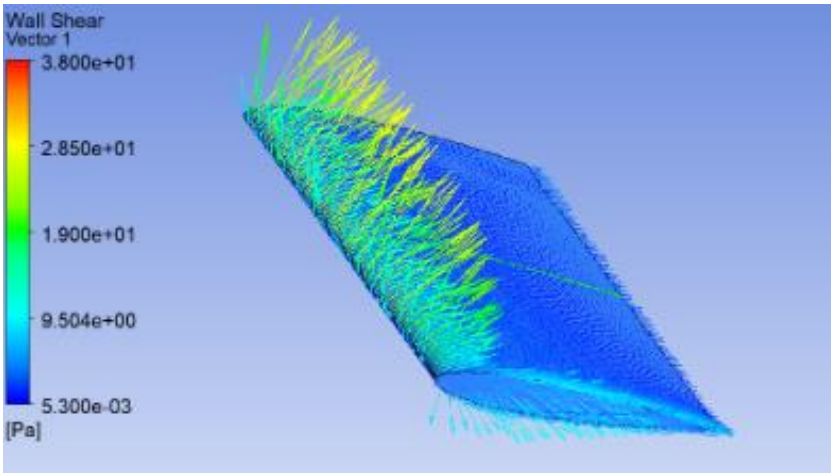

Figure B.11: Wall Shear Vector Plot for Re = 1.0E6; α = 12°

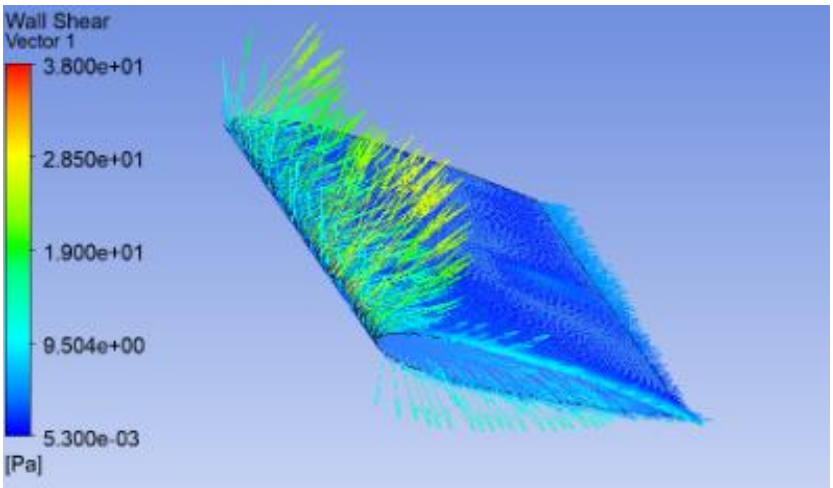

Figure B.12: Wall Shear Vector Plot for Re = 1.0E6; α = 15°

Below are the wall shear vector plots gathered for Re = 1.2 mil for α = 6°, 9°, 12°, and 15° respectively

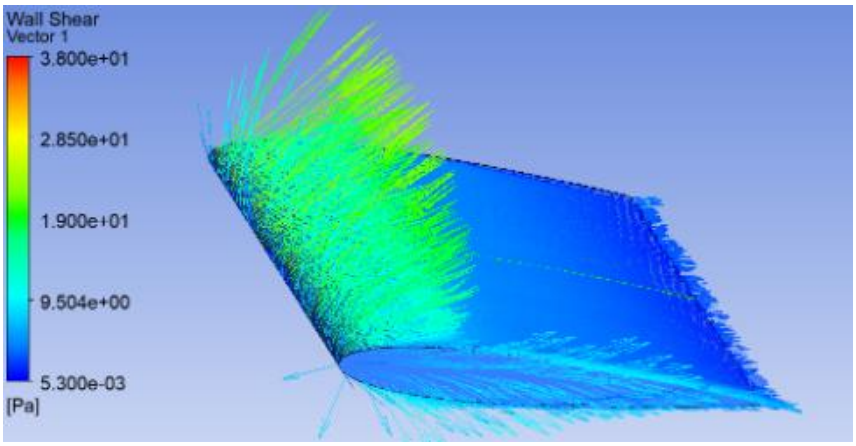

Figure B.13: Wall Shear Vector Plot for Re = 1.2E6; α = 6°

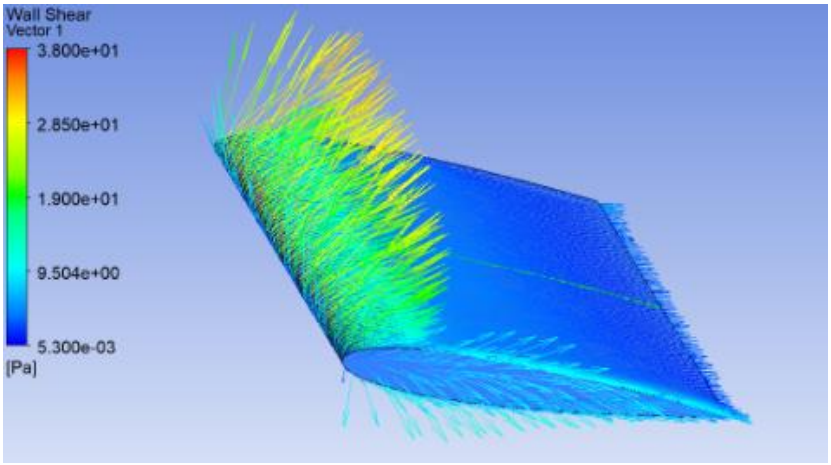

Figure B.14: Wall Shear Vector Plot for Re = 1.2E6; α = 9°

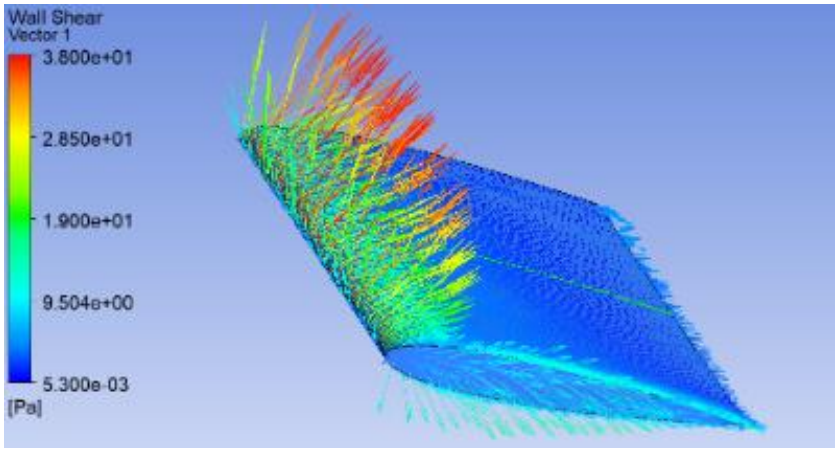

Figure B.15: Wall Shear Vector Plot for Re = 1.2E6; α = 12°

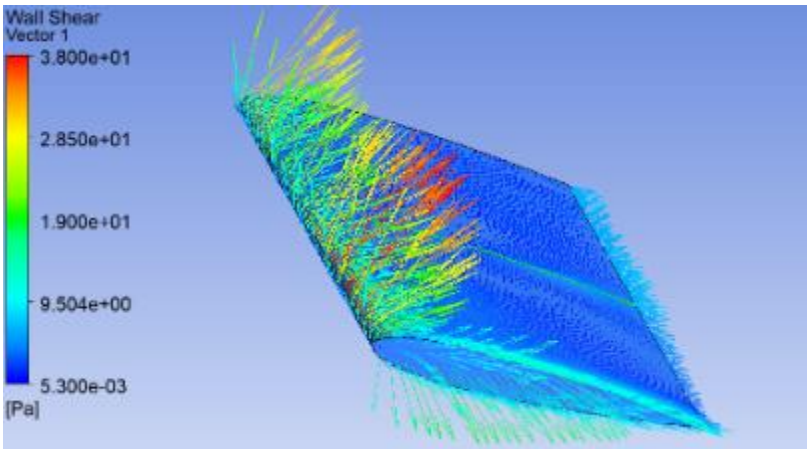

Figure B.16: Wall Shear Vector Plot for Re = 1.2E6; α = 15°

Appendix C Skin Friction Coefficient Plots

Below are the skin friction coefficient plots gathered for Re = 600k for α = 6°, 9°, 12°, and 15° respectively

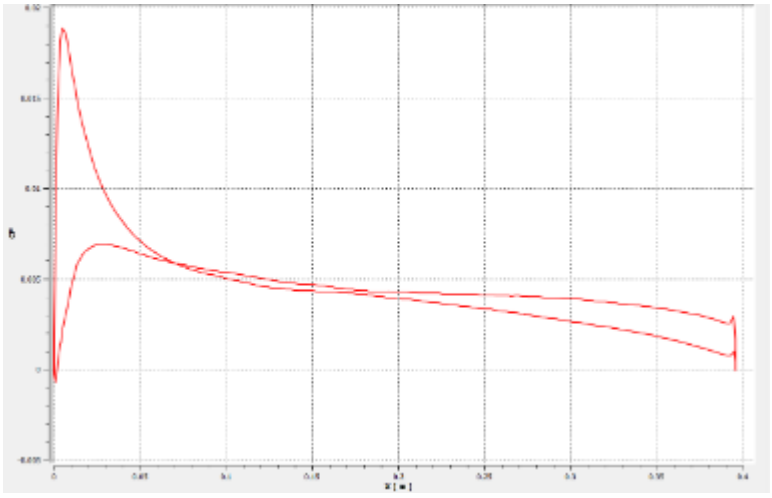

Figure C.1: Skin Friction Coefficient Plot for Re = 6.0E5; α = 6°

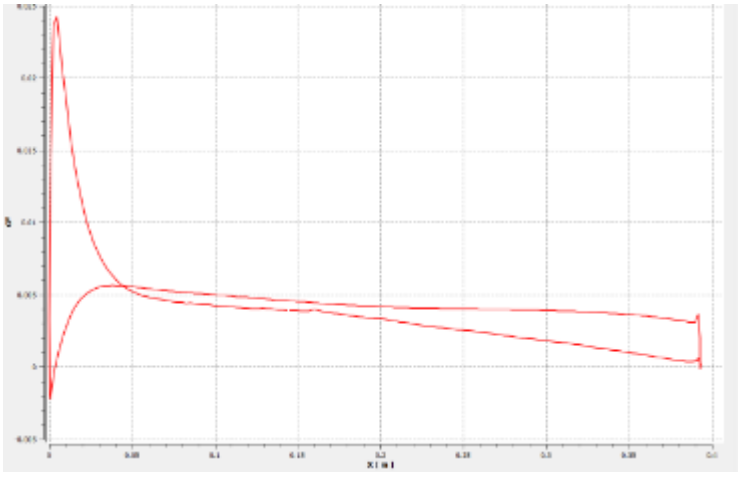

Figure C.2: Skin Friction Coefficient Plot for Re = 6.0E5; α = 9°

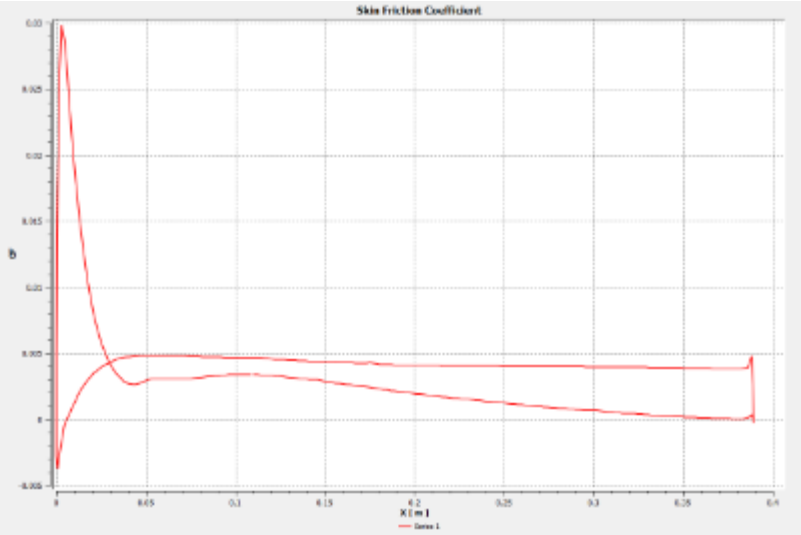

Figure C.3: Skin Friction Coefficient Plot for Re = 6.0E5; α = 12°

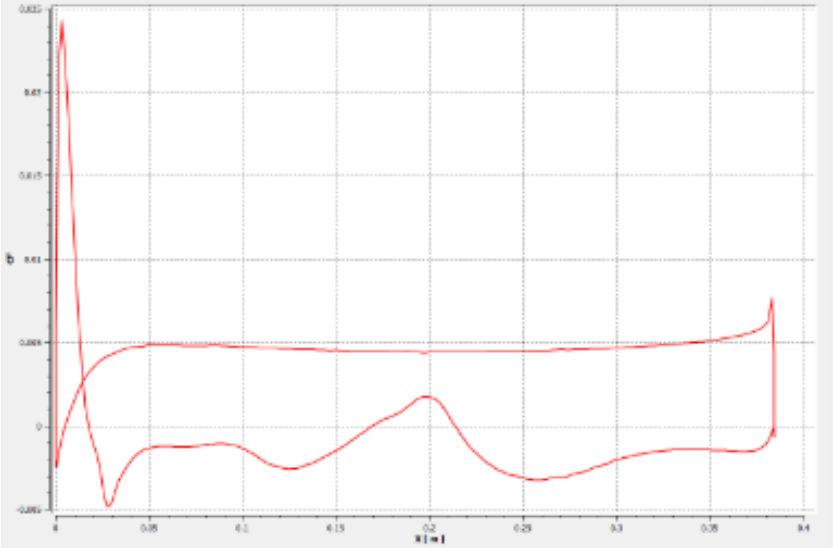

Figure C.4: Skin Friction Coefficient Plot for Re = 6.0E5; α = 15°

Below are the skin friction coefficient plots gathered for Re = 800k for α = 6°, 9°, 12°, and 15° respectively

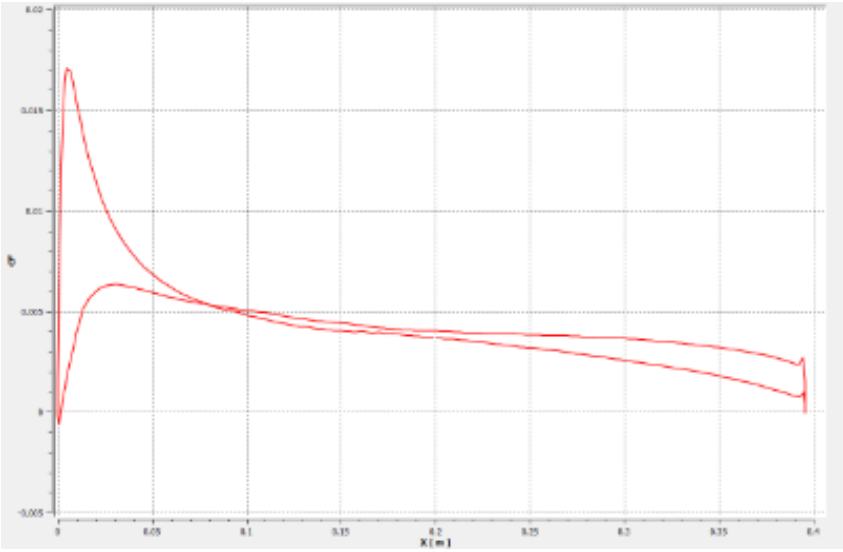

Figure C.5: Skin Friction Coefficient Plot for Re = 8.0E5; α = 6°

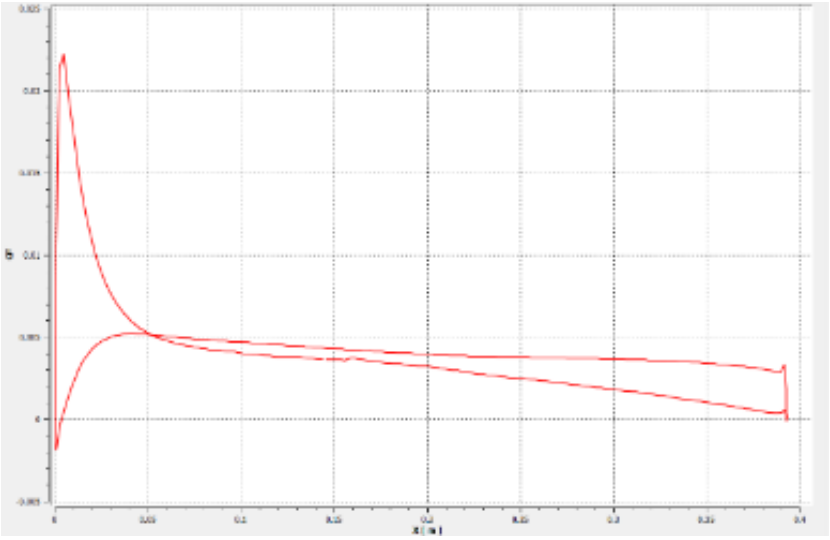

Figure C.6: Skin Friction Coefficient Plot for Re = 8.0E5; α = 9°

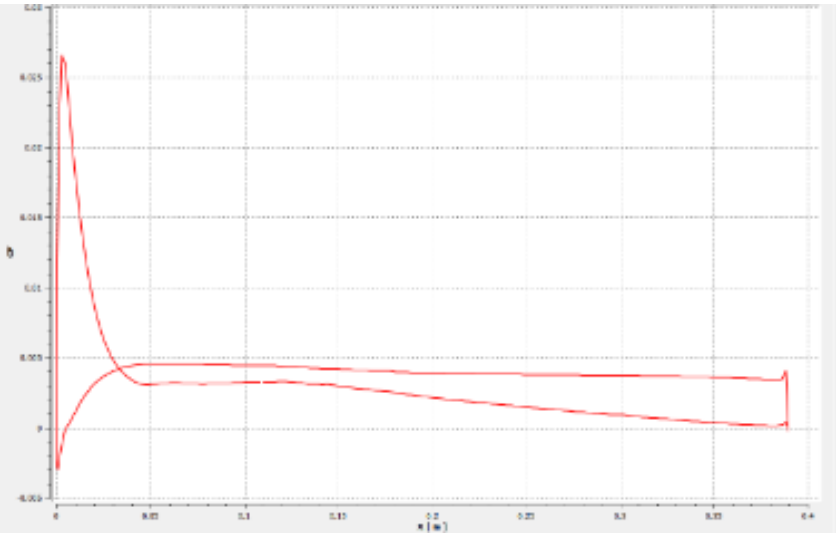

Figure C.7: Skin Friction Coefficient Plot for Re = 8.0E5; α = 12°

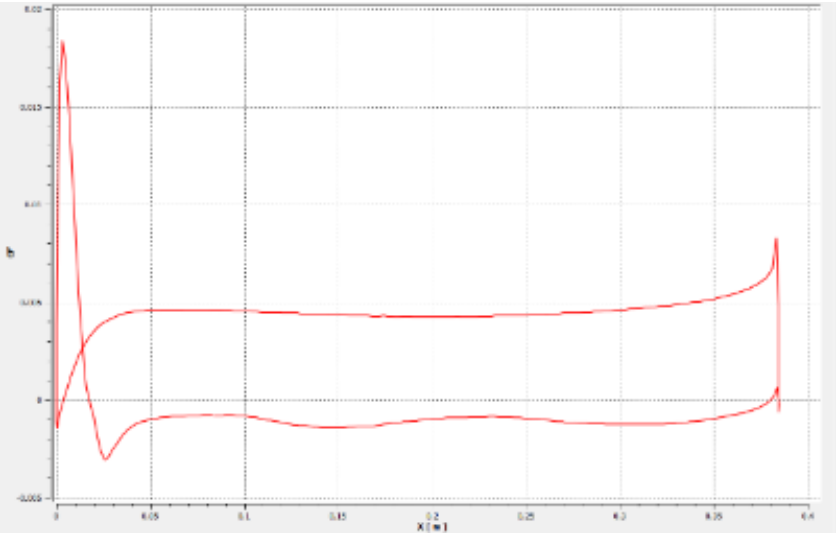

Figure C.8: Skin Friction Coefficient Plot for Re = 8.0E5; α = 15°

Below are the skin friction coefficient plots gathered for Re = 1 mil for α = 6°, 9°, 12°, and 15° respectively

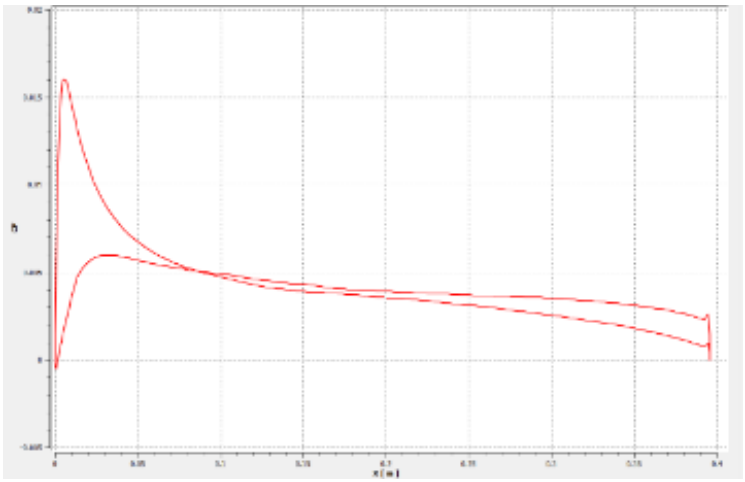

Figure C.9: Skin Friction Coefficient Plot for Re = 1.0E6; α = 6°

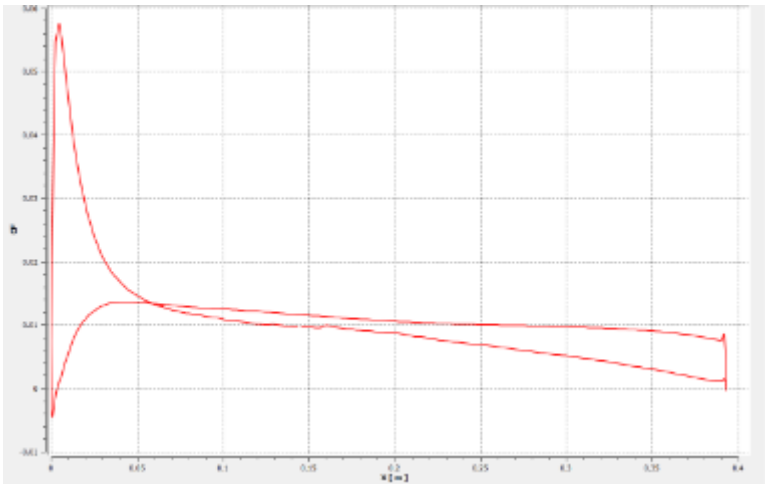

Figure C.10: Skin Friction Coefficient Plot for Re = 1.0E6; α = 9°

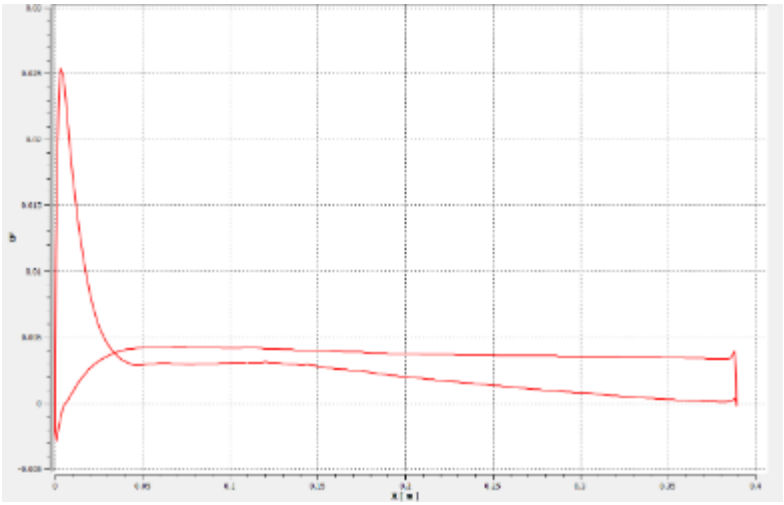

Figure C.11: Skin Friction Coefficient Plot for Re = 1.0E6; α = 12°

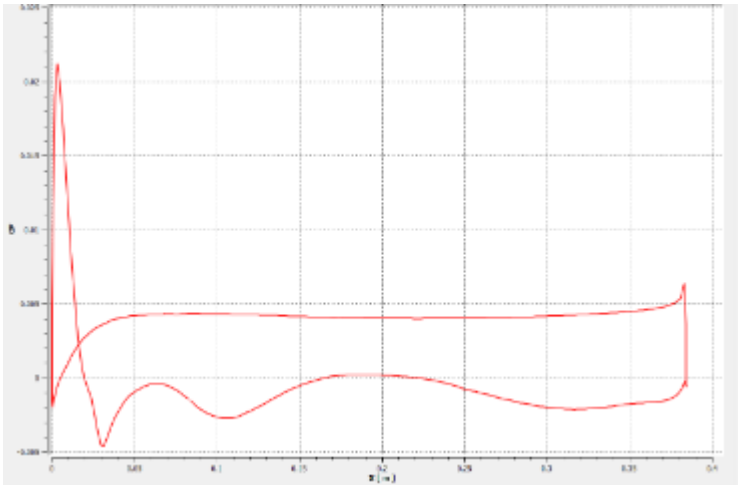

Figure C.12: Skin Friction Coefficient Plot for Re = 1.0E6; α = 15°

Below are the skin friction coefficient plots gathered for Re = 1.2 mil for α = 6°, 9°, 12°, and 15° respectively

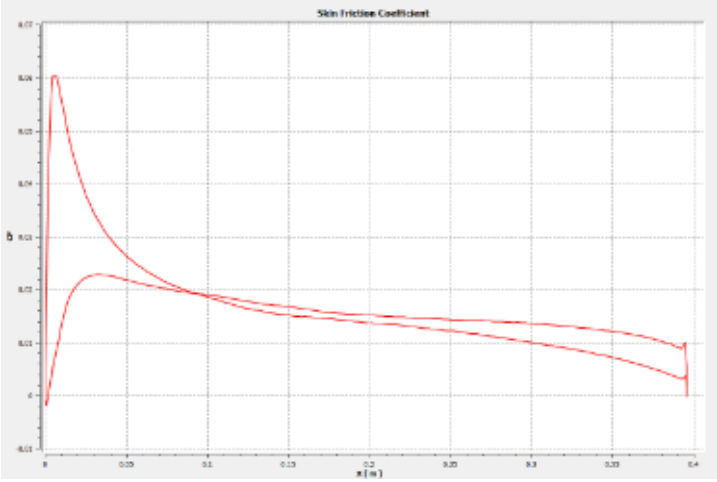

Figure C.13: Skin Friction Coefficient Plot for Re = 1.2E6; α = 6°

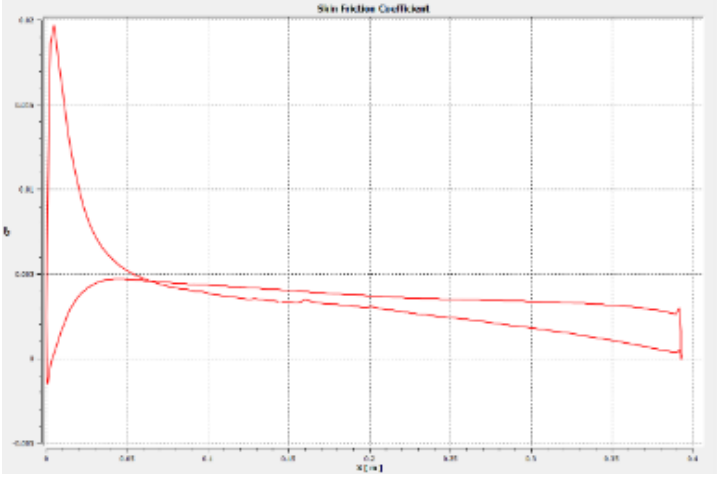

Figure C.14: Skin Friction Coefficient Plot for Re = 1.2E6; α = 9°

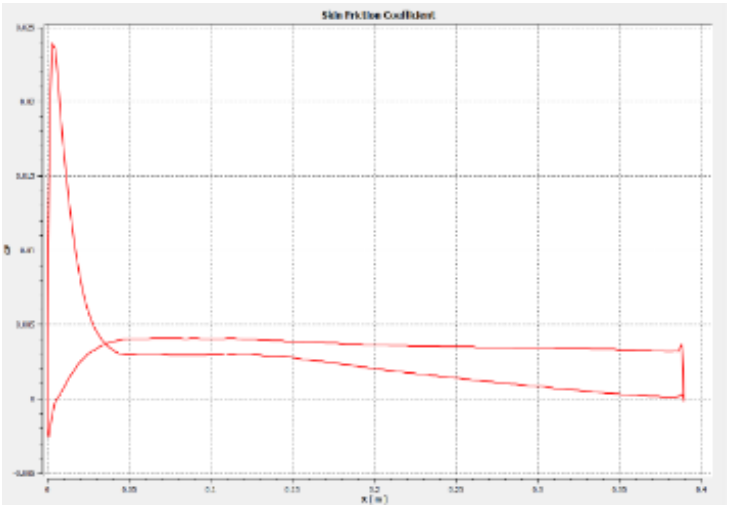

Figure C.15: Skin Friction Coefficient Plot for Re = 1.2E6; α = 12°

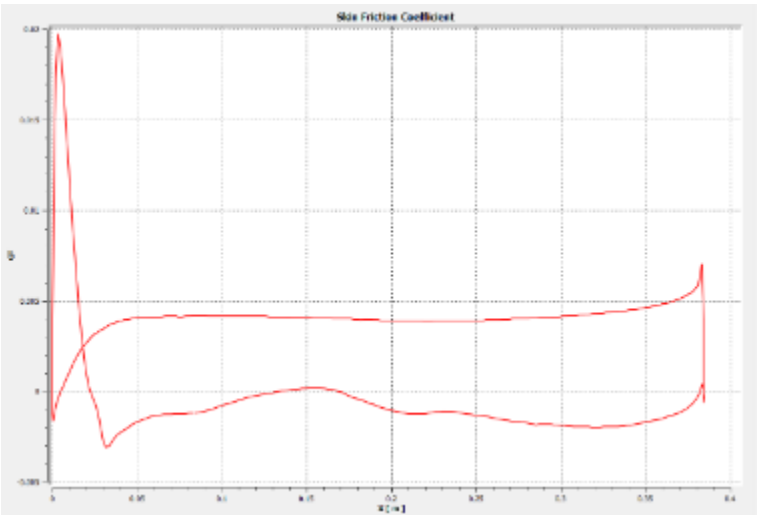

Figure C.16: Skin Friction Coefficient Plot for Re = 1.2E6; α = 15°

Appendix D Streamline Plots

Below are the velocity streamline plots gathered for Re = 600k for α = 6°, 9°, 12°, and 15° respectively

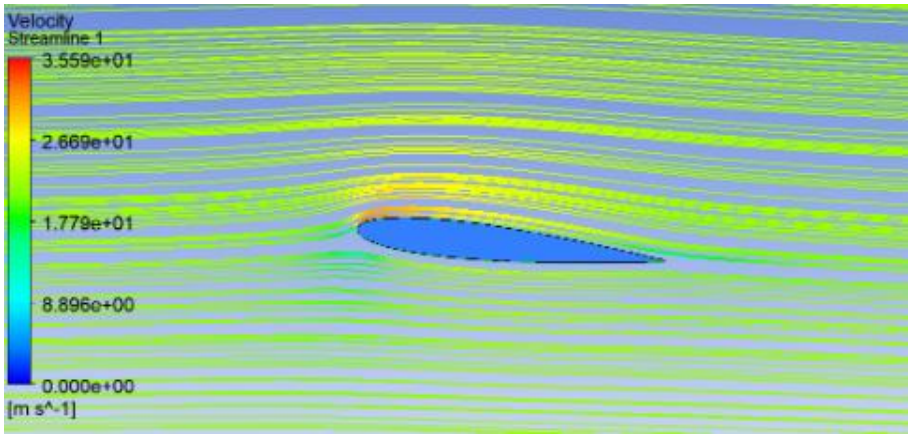

Figure D.1: Velocity Streamline for Re = 6.0E5; α = 6°

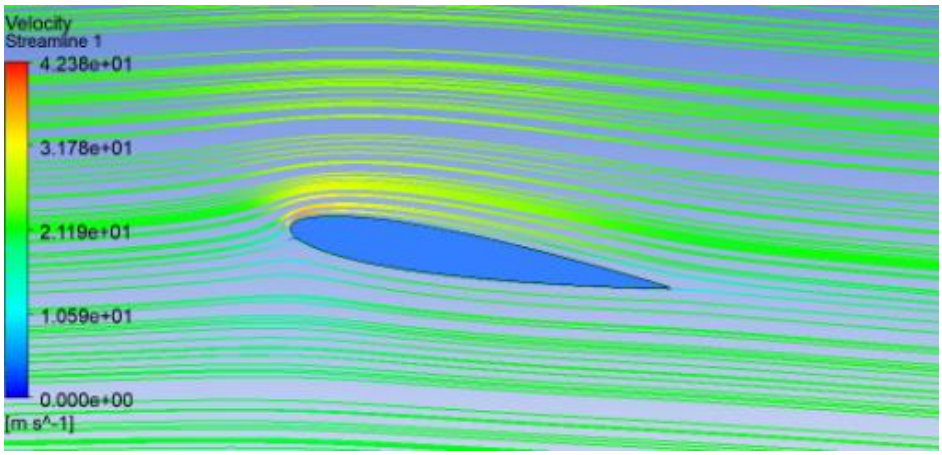

Figure D.2: Velocity Streamline for Re = 6.0E5; α = 9°

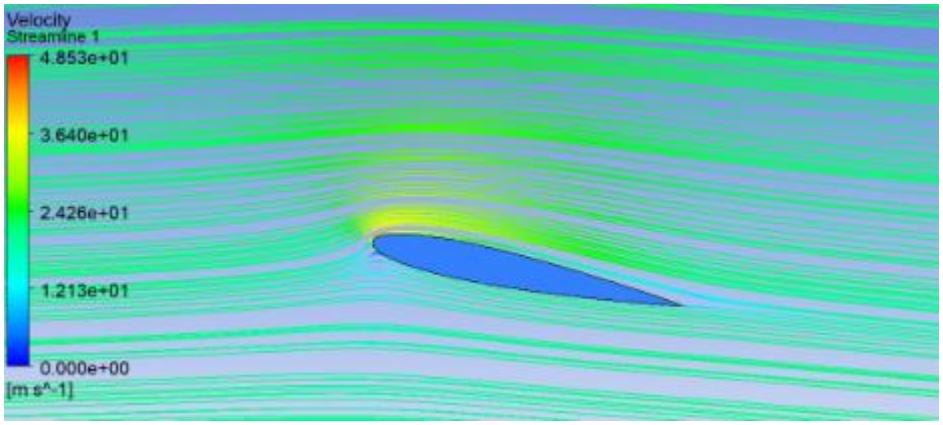

Figure D.3: Velocity Streamline for Re = 6.0E5; α = 12°

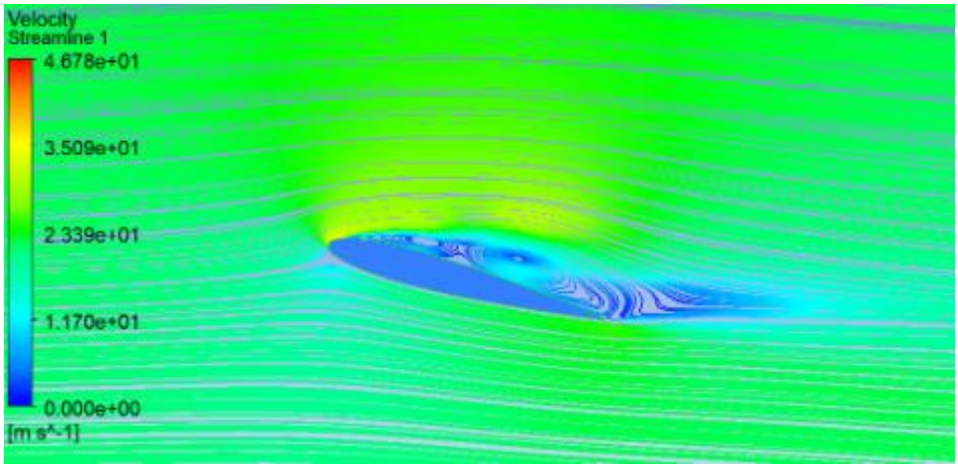

Figure D.4: Velocity Streamline for Re = 6.0E5; α = 15°

Below are the velocity streamline plots gathered for Re = 800k for α = 6°, 9°, 12°, and 15° respectively

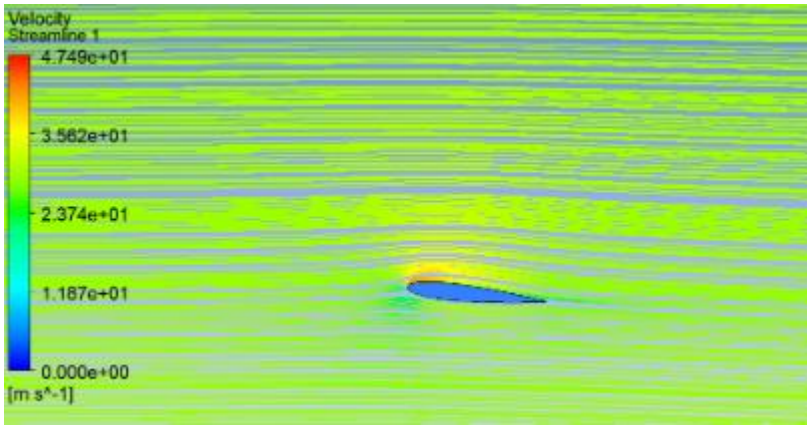

Figure D.5: Velocity Streamline for Re = 8.0E5; α = 6°

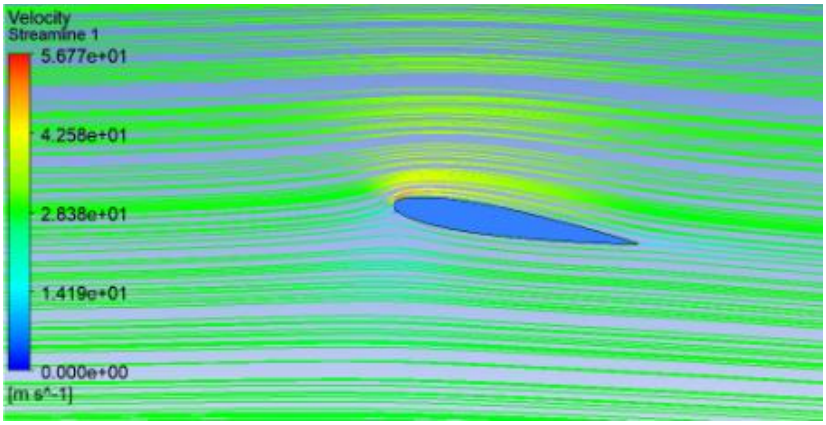

Figure D.6: Velocity Streamline for Re = 8.0E5; α = 9°

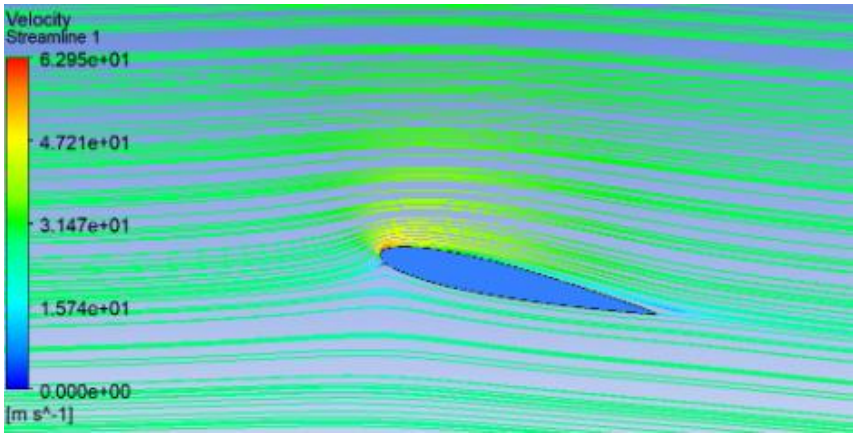

Figure D.7: Velocity Streamline for Re = 8.0E5; α = 12°

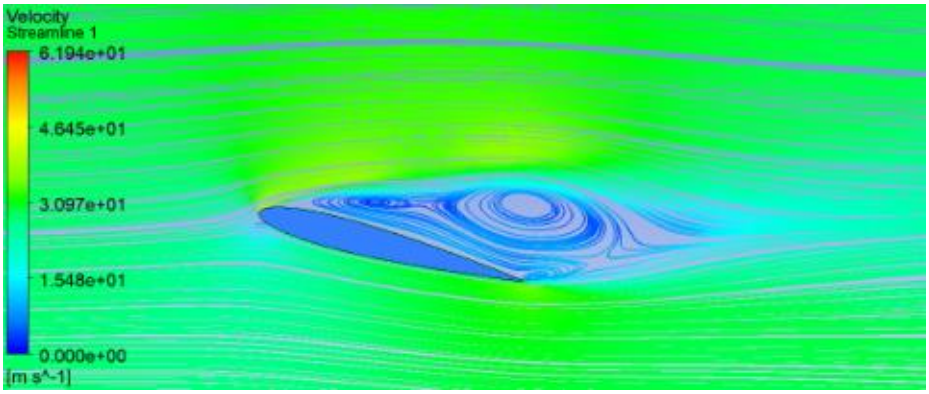

Figure D.8: Velocity Streamline for Re = 8.0E5; α = 15°

Below are the velocity streamline plots gathered for Re = 1 mil for α = 6°, 9°, 12°, and 15° respectively

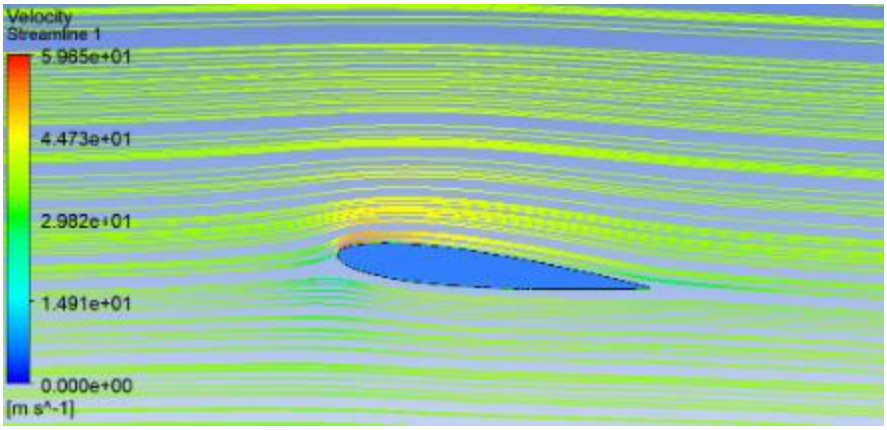

Figure D.9: Velocity Streamline for Re = 1.0E6; α = 6°

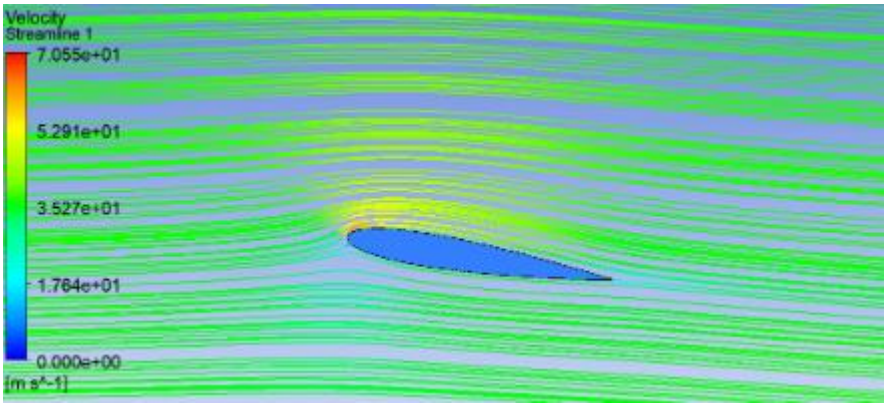

Figure D.10: Velocity Streamline for Re = 1.0E6; α = 9°

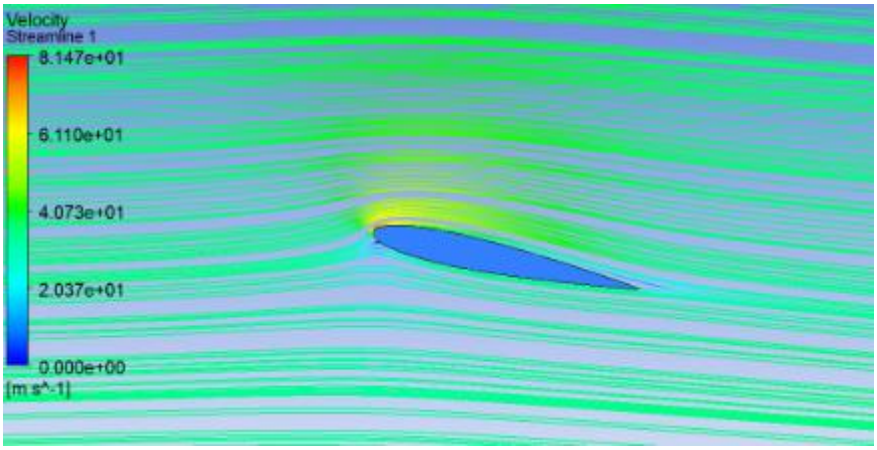

Figure D.11: Velocity Streamline for Re = 1.0E6; α = 12°

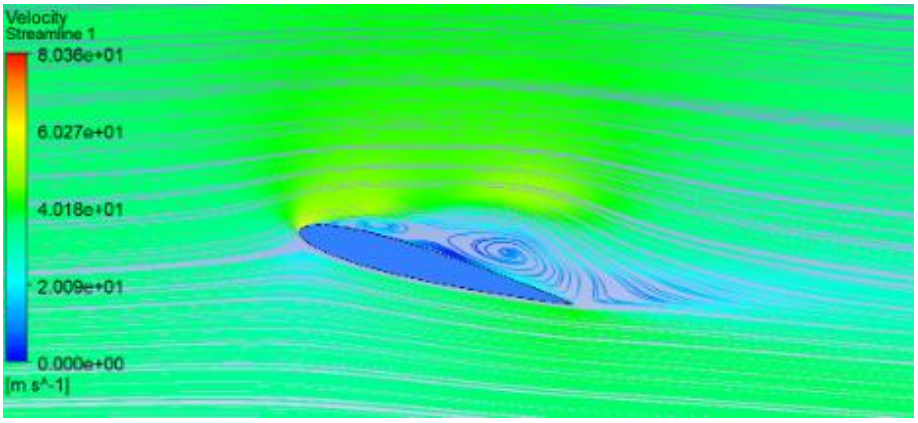

Figure D.12: Velocity Streamline for Re = 1.0E6; α = 15°

Below are the velocity streamline plots gathered for Re = 1.2 mil for α = 6°, 9°, 12°, and 15° respectively

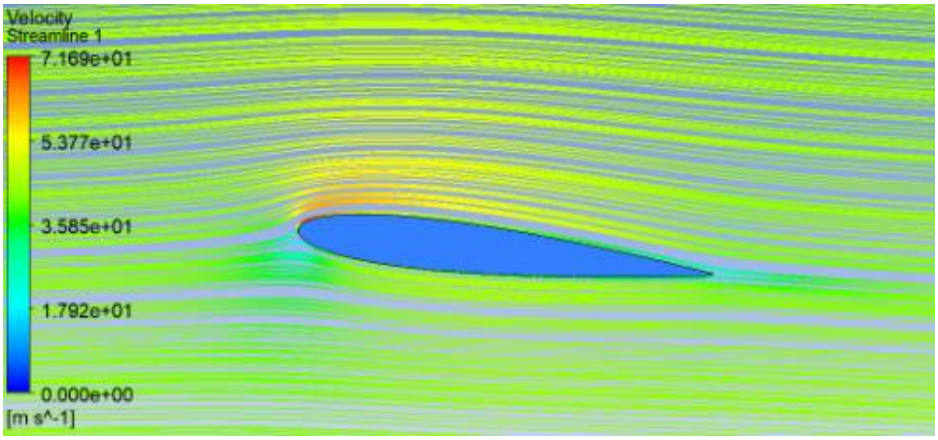

Figure D.13: Velocity Streamline for Re = 1.2E6; α = 6°

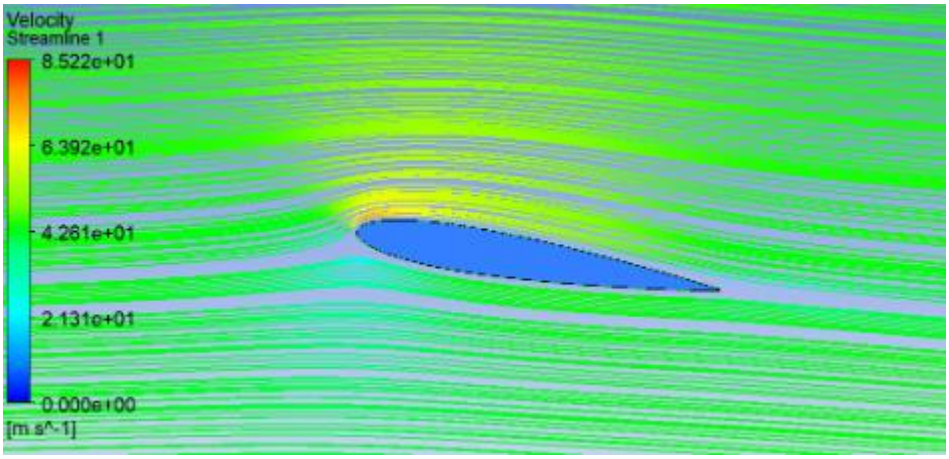

Figure D.14: Velocity Streamline for Re = 1.2E6; α = 9°

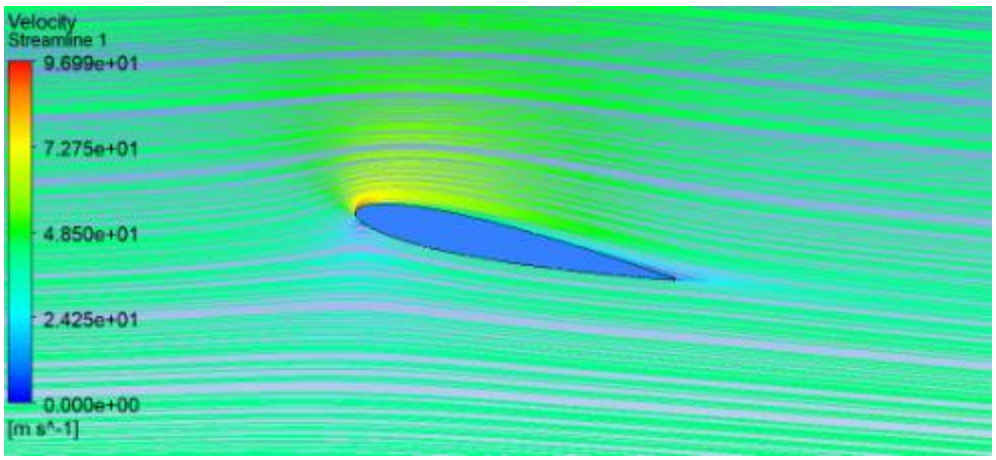

Figure D.15: Velocity Streamline for Re = 1.2E6; α = 12°

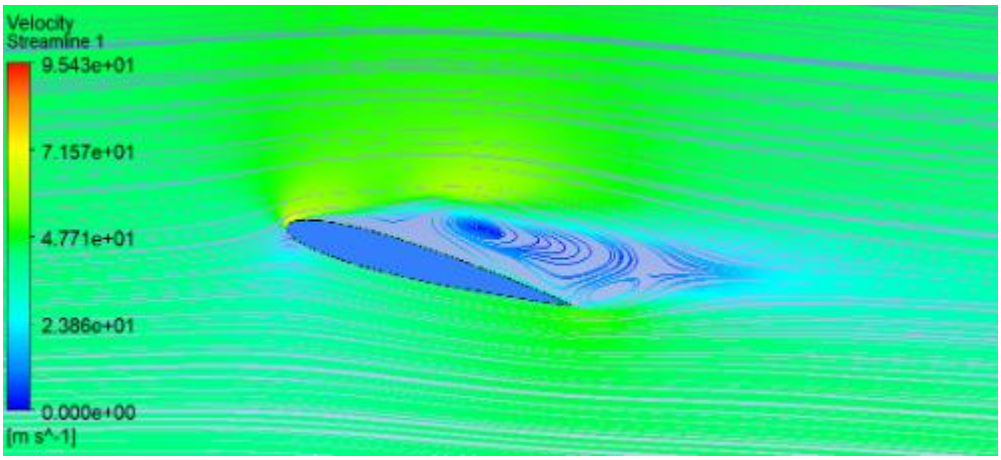

Figure D.16: Velocity Streamline for Re = 1.2E6; α = 15°